DESIGN AND ANALYSIS OF ULTRAWIDE ELASTIC METAMATERIAL FOR THREE-DIMENSIONAL VIBRATION ISOLATION

by

Berkay Acar

B.S., Mechanical Engineering, Boğaziçi University, 2019

Submitted to the Institute for Graduate Studies in
Science and Engineering in partial fulfillment of
the requirements for the degree of
Master of Science

Graduate Program in Mechanical Engineering
Boğaziçi University
2022

ACKNOWLEDGEMENTS

Firstly, I would like to offer my great thanks to Prof. Çetin Yılmaz for his guidance even in the most desperate times and countless choke points. Without his boosting motivation and enlightening wisdom, I would never dedicate myself to finalize this project.

My teammates Sedef Nisan Otlu and Zafer Gökay Tetik have been the main source of my motivation by their endless efforts and sacrifices. I owe a great thanks to both of them. I also cannot forget both mental and technical support of my colleagues and mentors in BMC Power, Yunus Emre Torun and İbrahim Çiylez.

The spherical nodes and the pipes in the space frame structure are donated by Uzay Konstrüksiyon Sistemleri İnşaat Sanayi ve Ticaret Ltd. Şti.

This work was supported by TUBITAK Grant No. 218M475.

ABSTRACT

DESIGN AND ANALYSIS OF ULTRAWIDE ELASTIC METAMATERIAL FOR THREE-DIMENSIONAL VIBRATION ISOLATION

Metamaterials are materials that are modified to bring in particular desired properties that are not inherited from original substance. Using number of techniques, materials can be engineered to have completely different electrical, optical, chemical or mechanical properties without changing it's chemical compound. The focus of this thesis is to obtain a broadband elastic metamaterial that does not allow transmission of vibration at low frequencies in three dimensions. In order to achieve broadband vibration isolation at low frequencies, inertial amplification method is utilized. Various unit cell geometries are investigated and optimization studies are conducted to widen the vibration isolation frequency range. The optimized design is manufactured and tested. It is shown that the manufactured prototype has the widest band gap in three-dimensions when all the three-dimensional elastic metamaterials and phononic crystals in the literature are considered.

ÖZET

ÜÇ BOYUTLU TİTREŞİM YALITIMI İÇİN ULTRA GENİŞ BANT ARALIKLI ELASTİK METAMALZEME TASARIMI VE ANALİZİ

Metamalzemeler, belli özelliklere sahip malzemeler elde etmek adına özel olarak işlemler görmüş maddelerdir. Belli teknikler kullanarak, malzemeler doğal hallerinden çok farklı termal, kimyasal, optik veya elektiksel materyal özellikleri kimyasal bileşimlerini değiştirmeden kazandırılabilmektedir. Bu tezin konusu da geniş frekans bandı aralığına sahip, üç boyutta titreşim dalgalarının iletimine izin vermeyen ve düşük frekanslarda çalışan elastik metamalzeme geliştirmektir. Düşük frekanslarda geniş bant aralığını elde edebilmek için atalet artırımı yöntemi tercih edilmiştir. Çeşitli birim hücre yapıları incelenmiş ve titreşim yalıtım frekans bant aralığını genişletmek amacıyla optimizasyon çalışmaları yapılmıştır. Optimize edilen tasarımın üretimi yapılmış ve test edilmiştir. Literatürdeki diğer üç boyutlu elastik metamalzemeler ve fononik kristaller incelendiğinde, üretilen prototipin bant aralığı en geniş sistem olduğu gözlemlenmektedir.

TABLE OF CONTENTS

LIST OF FIGURES

LIST OF TABLES

LIST OF SYMBOLS

k	Stiffness of the spring of inertial amplification mechanism
k_a	Stiffness of the bars of inertial amplification mechanism
m	Mass at the corners of inertial amplification mechanism
m_a	Mass in the middle of inertial amplification mechanism
u	Displacement of corner masses
x	Excitation output value to the lumped parameter system
y	Excitation input value to the lumped parameter system
ω_{p1}	First resonance frequency
ω_{z1}	First anti-resonance frequency
θ	Angle between horizontal line and the rigid bar

LIST OF ACRONYMS/ABBREVIATIONS

1D	One Dimensional
2D	Two Dimensional
3D	Three Dimensional
DOF	Degree of Freedom
FRF	Frequency Response Function
GRSM	Global Response Search Method
IAM	Inertial Amplification Mechanism
RCR	Remote Center of Rotation

1. INTRODUCTION

Main purpose of this thesis is building up on the foundations of vibration isolation using inertial amplification method improved by various researchers. Firstly, a number topics are needed to be mentioned to easily understand the later discussions. Secondly, development history of the inertial amplification mechanism of this thesis will be given.

1.1. Mechanical Vibration

Mechanical vibration is a periodic motion about an equilibrium position. It might be created on purpose, like in the case of a musical instruments or quartz resonators or it might be unwanted, like an earthquake or vibration of washing machine [5].

1.2. Spectral Gaps

Spectral gap, or specifically phononic band gap, refers to the frequency range in which vibrations and elastic waves can be halted [6,7]. Generally, a unit cell is designed for the frequency range of interest and then assembled to generate a periodic structure. If these periodic structures are subjected to vibrations or elastic waves in their phononic band gap, vibration or waves cannot propagate inside the structure. Infinite periodic structures can completely isolate vibrations [8]. However, because it is impossible to obtain an infinite structure, only partial isolation can be achieved by finite periodic structures. Performance of finite periodic structures can be measured by depth and width of the band gap obtained by frequency response function (FRF) analysis [9–11]. Arithmetic mean normalized bandwidth (BW) can be used as a quantitative measure for spectral gaps [12] and can be calculated as

$$BW = \frac{\omega_u - \omega_l}{(\omega_u + \omega_l)/2}. \tag{1.1}$$

Phononic band gaps can also be used in mechanical filters and acoustic wave guides [13]. Additionally acoustic lenses and wave guides can utilize spectral gaps to achieve their purpose [14, 15].

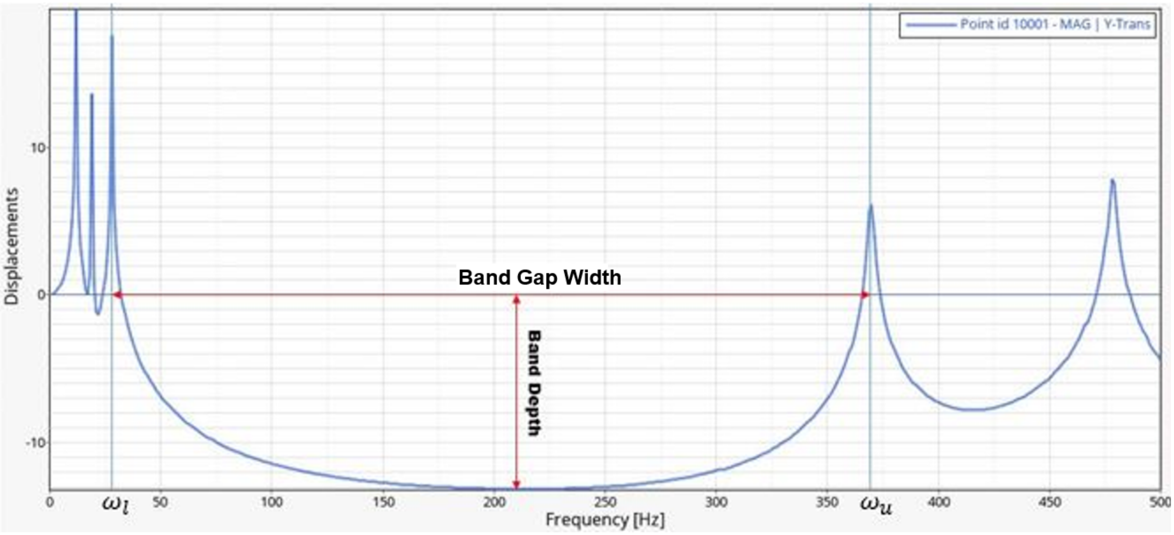

Figure 1.1. A generic frequency response function analysis result for structure that creates phononic band gap.

Structures with phononic band gaps can be periodic in one, two or three dimensions. Isolation is provided in the direction that the structure is periodic. While periodic structures in one direction can provide isolation in one direction, a 3-D periodic structure can provide isolation in all directions [16–21].

Mechanical filters, sound and vibration insulators and acoustic wave guides are some of the examples that phononic gap structures are used [22]. Bragg scattering and local resonances [23] are the two most common methods to create phononic band gaps [20, 24–27].

However, in recent years, a novel band generation method based on inertial amplification was introduced [28–30]. In this method, displacement amplification mechanisms are utilized to obtain an increased effective inertia of small masses. This method is much more effective than Bragg scattering at low-frequencies because band gaps can be formed below the Bragg limit. Additionally, as an advantage to local resonance method, because the effective inertia is increased, system can be designed without using large masses [31]. As sub-wavelength band gaps can be obtained with this method, periodic structures with inertial amplification are also called as elastic metamaterials.

The system designed in this thesis is aimed to provide seismic isolation, hence large bandwidth at low frequencies are desired. Main purpose of seismic isolation is providing protection against the destructive effects of vibration during earthquakes [32]. Nowadays, seismic isolation technology utilizes damping components along with sliding or rotating mechanisms, generally elements like rubber insulators, lead core rubber insulators with elastic capabilities or friction pendulum insulators are used [32–34]. Bragg Scattering and local resonance methods are widely used for seismic isolation purposes [8, 35–47]. However, these methods are not capable of creating wide band gaps at low frequencies [30, 31]. Besides very limited number of designs are suitable for three dimensional vibration isolation. In Table 1.1 different studies for obtaining ultrawide spectral gaps in 3D are given along with their lower and higher band gap frequency.

Table 1.1. 3D structures with ultrawide band gaps.

References	ω_l(Hz)	ω_u(Hz)	BW	ω_u/ω_l	Material
Muhammad and Lim, 2021 [48]	1292.5	16875	171.5	13.05	PLA
Lucklum and Vellekoop, 2018 [49]	0.0437	0.4702	166.0	11.19	Acrylic Plastic
Muhammad and Lim, 2021 [50]	1247.2	11319	160.2	9.30	PLA
D'Alessandro et al., 2019 [51]	455	2337	134.7	5.14	Nylon OA12

1.3. Inertial Amplification

In this thesis, phononic band gaps are achieved using the inertial amplification method, in which effective inertia of the unit cell is amplified by built-in mechanisms [30].

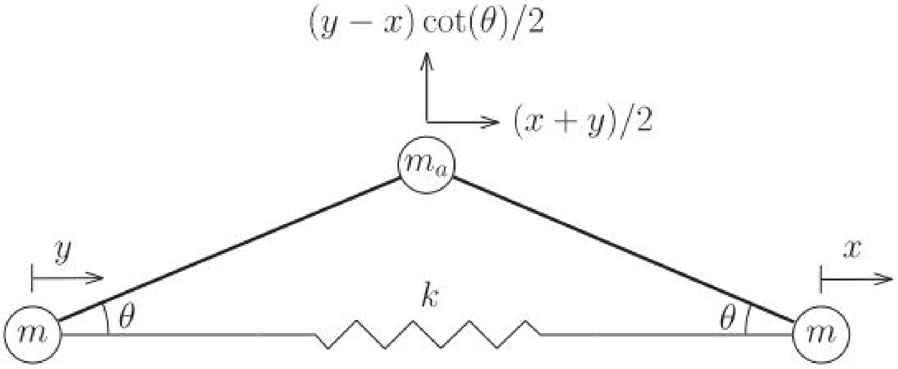

Figure 1.2. A simple inertial amplification mechanism [1].

For example, in Figure 1.2, if we assume that the rods connecting masses m and m_a are rigid, when masses m are translated by a small amounts of x and y ,m_a moves by the amount of $(y\text{-}x)\cot(\theta)/2$ in the vertical direction. For small θ, displacement of the mass m_a will be amplified considerably [33]. So, the mechanism does not change the stiffness of the overall structure, but it increases the effective mass. The displacement of the mass m_a depends on the input displacement y and output displacement x, hence there is no extra degree of freedom associated with mass m_a and the system has only one degree of freedom.

If y is the input displacement and x is the output displacement, the equation of motion of the system can be written as [1, 31],

$$\left(\frac{m_a(\cot^2(\theta)+1)}{4}+m\right)\ddot{x}+kx=\left(\frac{m_a(\cot^2(\theta)-1)}{4}+m\right)\ddot{y}+ky. \tag{1.2}$$

In Equation (1.2), even though the total mass of the system is $2m+m_a$, the effective inertia of the system, the term multiplied by ẍ, is amplified for small values of θ.

From Equation (1.2), the first resonance (ω_{p1}) frequency can be calculated as

$$\omega_{p1}=\sqrt{\frac{k}{m+m_a(\cot\theta^2+1)/4}}, \tag{1.3}$$

and anti resonance (ω_{z1}) frequency can be calculated as [35]

$$\omega_{z1}=\sqrt{\frac{k}{m_a(\cot\theta^2-1)/4}}. \tag{1.4}$$

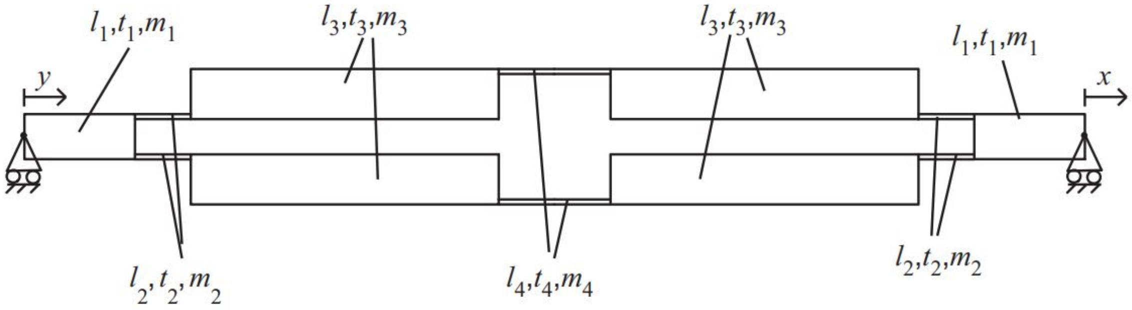

Figure 1.3. Lumped parameter model of an inertial amplification mechanism designed by Acar and Yılmaz [2]. Here y is the input and x is the output displacement.

Acar and Yilmaz [2] shows one of the first designs of the inertial amplification system related to this thesis. The inertial amplification system designed by Acar and Yılmaz [2] consists of four rectangular masses and thin flexible connections (see Figure 1.3). The inertial amplification mechanism with flexure hinges has multiple degrees of freedom. Moreover, if inertial amplification mechanisms are connected to form a one-dimensional or two-dimensional periodic structure, the band gap will be formed between the first two natural frequencies of the unit cell mechanism [2]. Hence, in Ref. 2, size optimization study is conducted to maximize the band gap.

In Yuksel and Yilmaz [3], shape optimization is conduced on the links of the inertial amplification mechanism and wider band gap is obtained compared to rectangular links (see Figure 1.4).

In addition to the width and depth of the gap, functioning direction of the mechanism is also considered as a performance parameter. To be able to function properly in three dimensions, flexible cross hinge design is proposed by Otlu [4]. The main focus of this thesis is to improve the band gap width of the mechanism shown in Figure 1.5 by making design changes and conducting optimization studies.

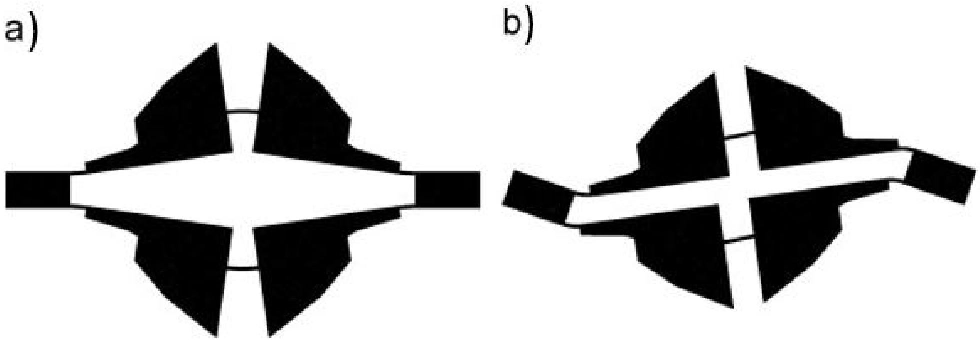

Figure 1.4. First two modes of 2-D model of the shape optimized unit mechanism designed by Yuksel and Yilmaz [3]. (a) The first mode (255.7 Hz) and (b) the second mode (817.4 Hz).

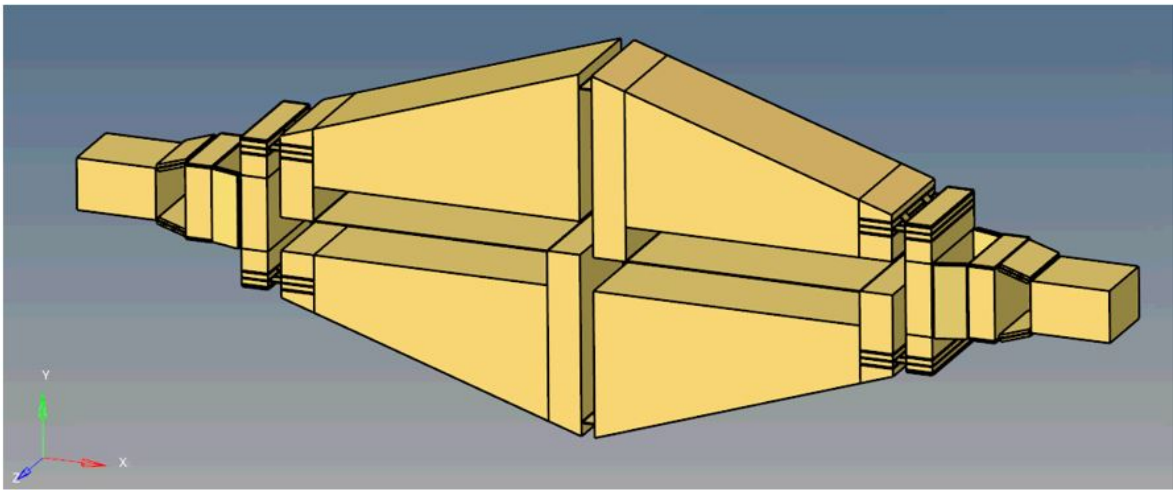

Figure 1.5. 3D Model of the inertial amplification mechanism in Otlu [4].

In this thesis, in addition to the works of Otlu [4], parametric studies are conducted. Transient response of the mechanism is calculated. Design optimization for manufacturing model is applied. An octahedron structure is designed, manufactured and tested. Lastly, test results are compared with the simulation results. It is also shown that the widest band gap in three dimensions is obtained when compared to the three-dimensional phononic crystals and elastic metamaterials in the literature.

2. DYNAMIC ANALYSIS

The latest inertial amplification system, which this thesis is build upon, designed for vibration isolation in 3D. The design details of the mechanism will be explained.

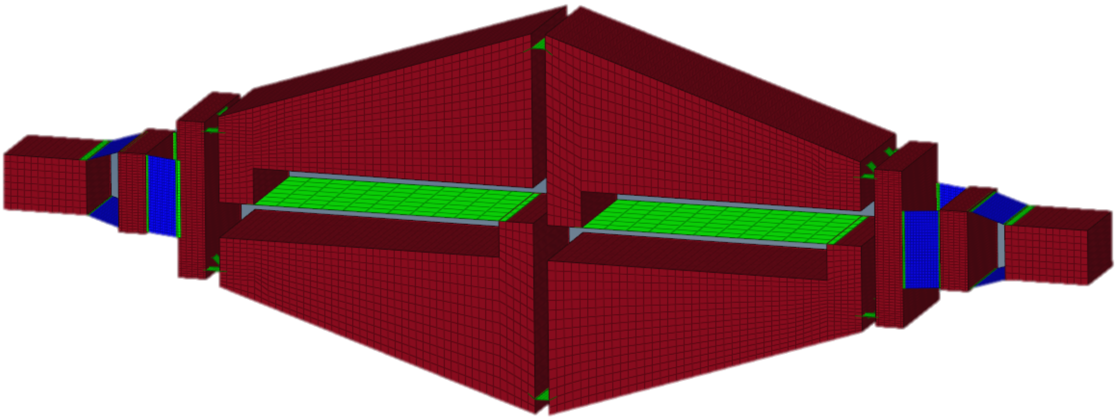

Figure 2.1. Finite element model of the inertial amplification mechanism in Otlu [4].

The finite element model consists of solid (maroon parts (Figure 2.1)) and shell elements with thickness of 1 mm (Dark Blue parts (Figure 2.1)) and 0.10 mm (green parts (Figure 2.1)). The whole structure is made up of steel with density of 7800 kg/m^3, 210 GPa elastic modulus and 0.3 Poisson ratio.

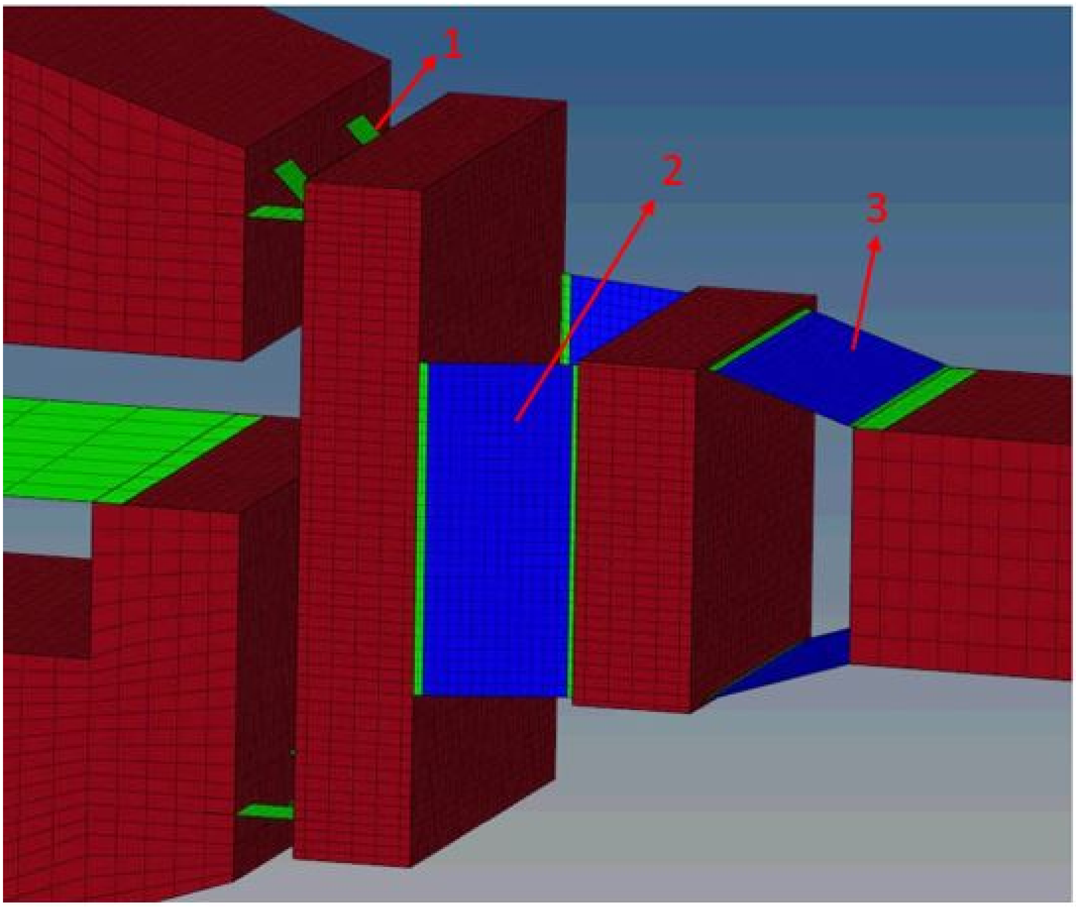

Figure 2.2. New mechanism that enables the inertial amplification system to be used in 3D vibration isolation. (1) cross and straight flexures. (2) Second stage of remote center of rotation mechanism. (3) First stage of remote center of rotation mechanism [4].

Connection between 2D and 3D elements are done by node-to-node equivalence and an additional layer of 2D elements are created inside the solid parts to obtain clamped boundary condition as shown in Figure 2.3.

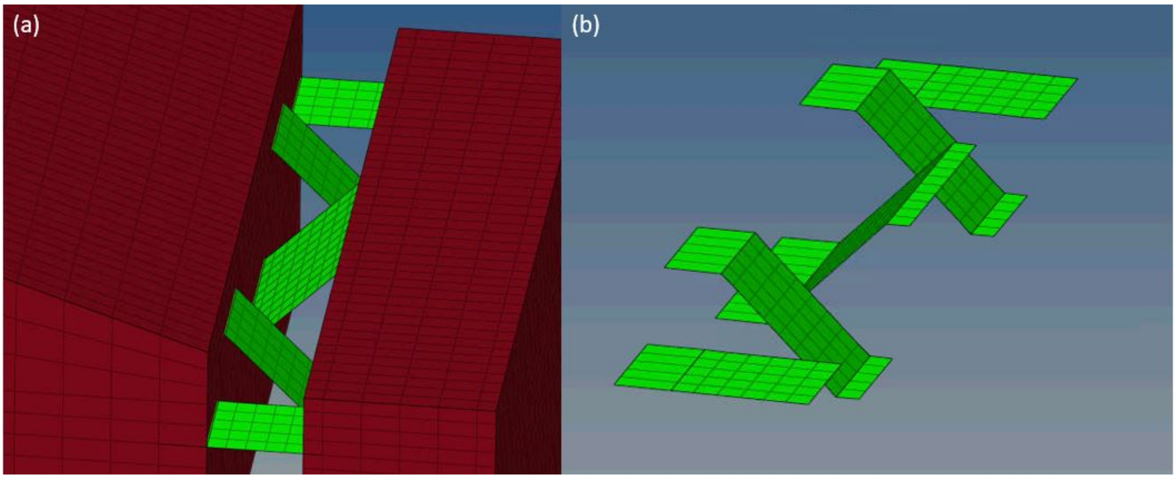

Figure 2.3. (a) Node-to-node equivalence between 2D and 3D elements. (b) Additional elements created through the 3D elements to obtain clamped boundary condition.

When the systems first six natural frequencies are calculated in free conditions, there is a large gap between the first and the second mode of the system in Table 2.1. First two mode shapes of the system are similar to the topologically optimized 2D vibration isolator designed by Yuksel and Yilmaz [1] that is build upon the 1D inertial amplification system designed by Taniker and Yilmaz [52]. The first mode is the opening and closing movement of the whole system (see Figure 2.4 at 18.23 Hz. Second and third modes are beam modes of the long flexures (see Figures 2.5 and 2.6) at 632.01 and 632.64 Hz. Fourth and fifth modes are rotation of the half mechanisms around the RCR mechanism blocks at 883.79 and 988.28 Hz (see Figures 2.7 and 2.8). These mode shapes are obtained by bending of the short flexures. Sixth mode is the torsional mode of the mechanism at 1019.90 Hz (see Figure 2.9).

Table 2.1. Natural frequencies of a single inertial amplification mechanism under free boundary conditions.

Mode Numbers	Natural Frequencies (Hz)
1st mode	18.23
2nd mode	632.01
3rd mode	632.65
4th mode	883.79
5th mode	988.28
6th mode	1019.90

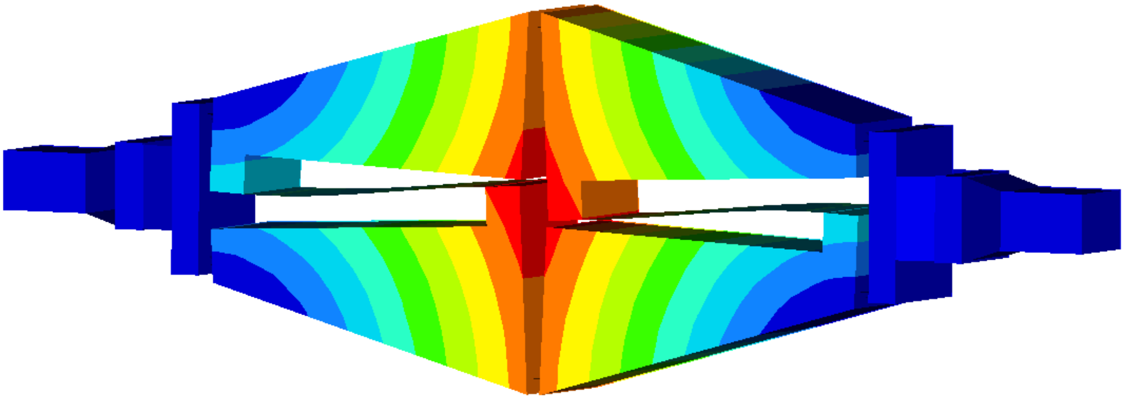

Figure 2.4. 1st mode shape of an inertial amplification mechanism at 18.23 Hz.

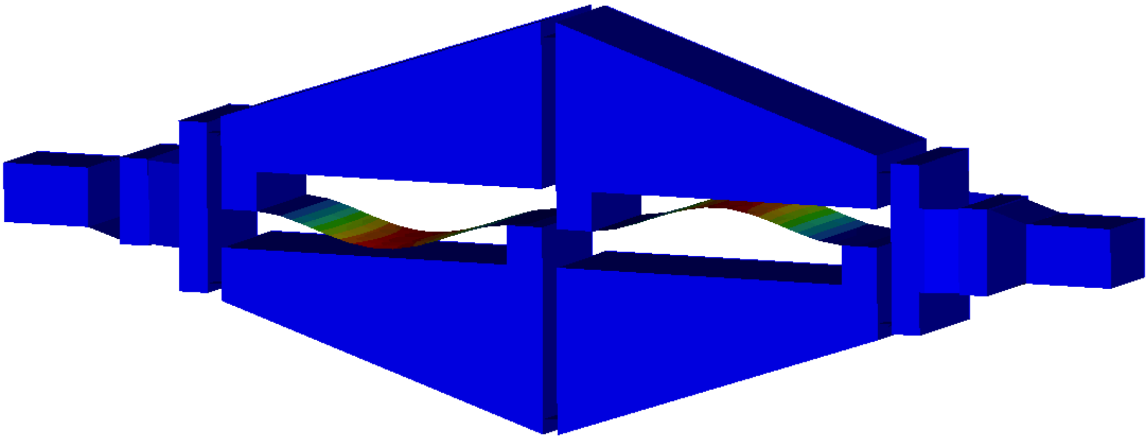

Figure 2.5. 2nd mode shape of an inertial amplification mechanism at 632.01 Hz.

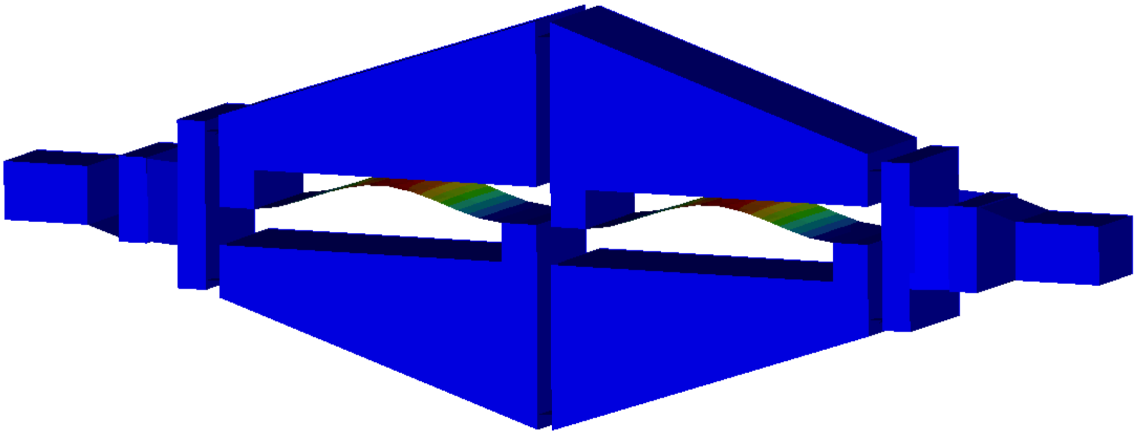

Figure 2.6. 3rd mode shape of the inertial amplification mechanism at 632.65 Hz.

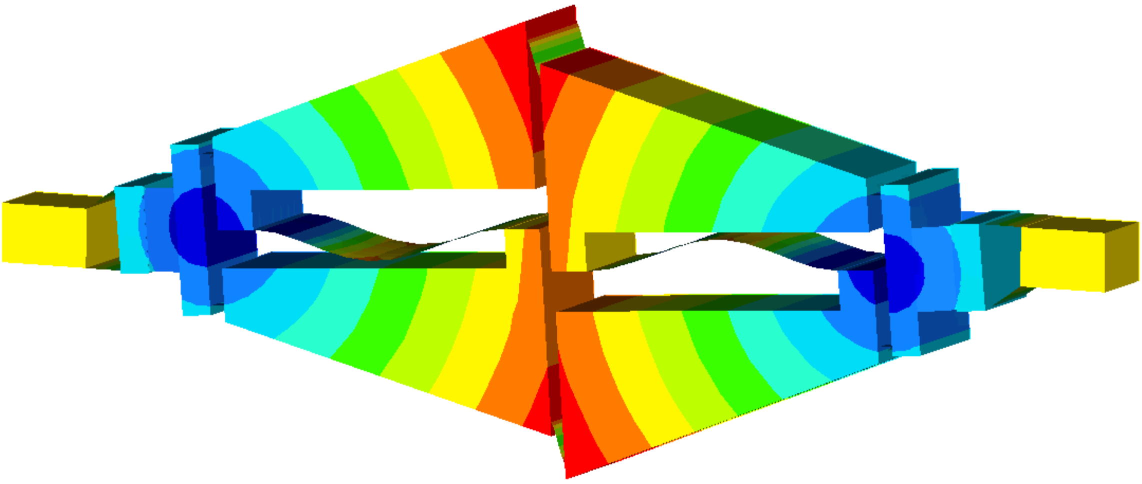

Figure 2.7. 4th mode shape of the inertial amplification mechanism at 883.79 Hz.

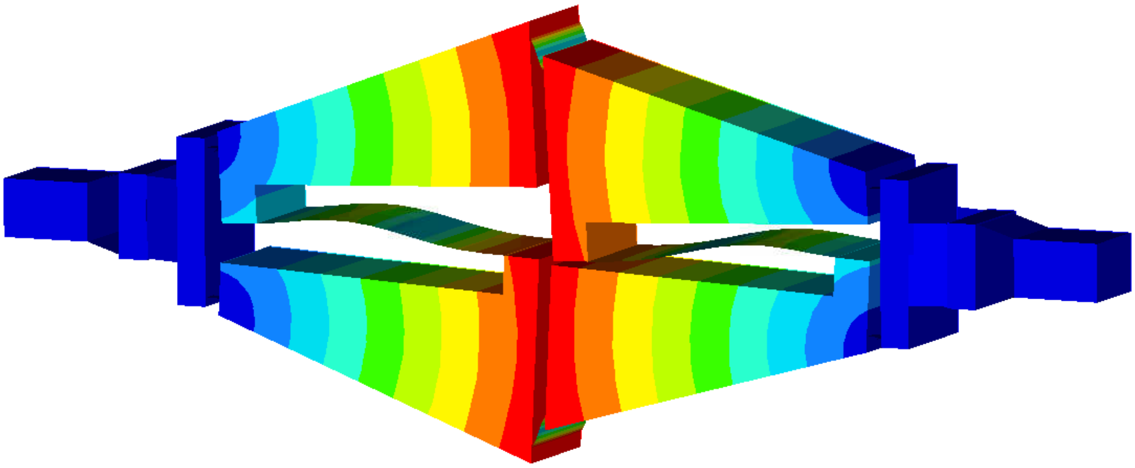

Figure 2.8. 5th mode shape of the inertial amplification mechanism at 988.28 Hz.

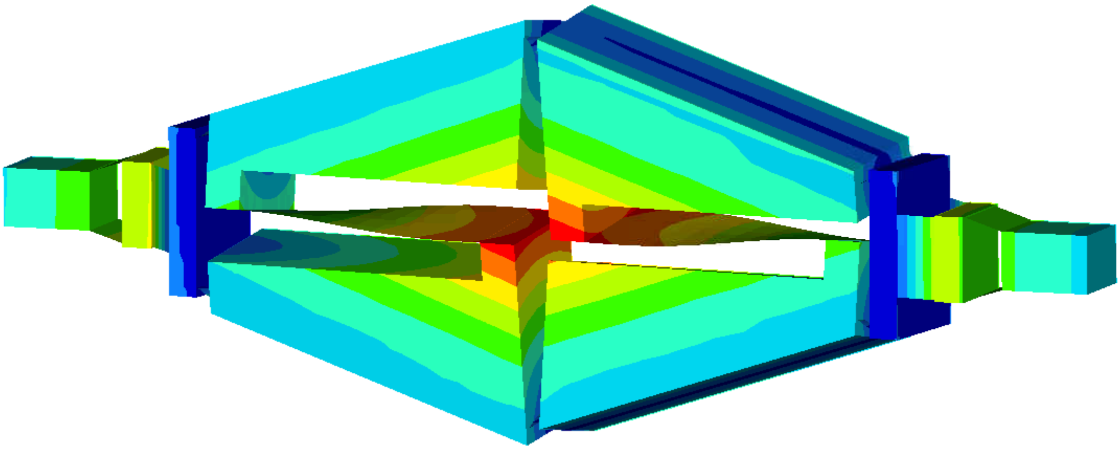

Figure 2.9. 6th mode shape of the inertial amplification mechanism at 1019.90 Hz.

Using the experiences obtained from the former versions of the 3D system [4], it is deduced that a single mechanism exhibits three different motion patterns in a periodic lattice. To obtain these motions, three different boundary conditions are applied to the system and natural frequencies are calculated. These boundary conditions are:

- Fixed - Axially free
- Fixed - Axially fixed
- Fixed - Diagonally free

The system is analyzed under the boundary conditions stated above to check if it is possible to have an idea about the behavior of the periodic structure just by analyzing a single unit. To apply the boundary condition as equal displacement of the tip nodes, rigid body (RBE2) element is used to connect the nodes at the end at a single point as shown in Figure 2.10. The difference between the out-of-plane modes of the mechanism under fixed-axial free boundary condition is shown in Figure 2.11. Rotation motion of the tip cannot be restricted due to the axial motion of the nodes at the tip surface unless RBE2 element is used.

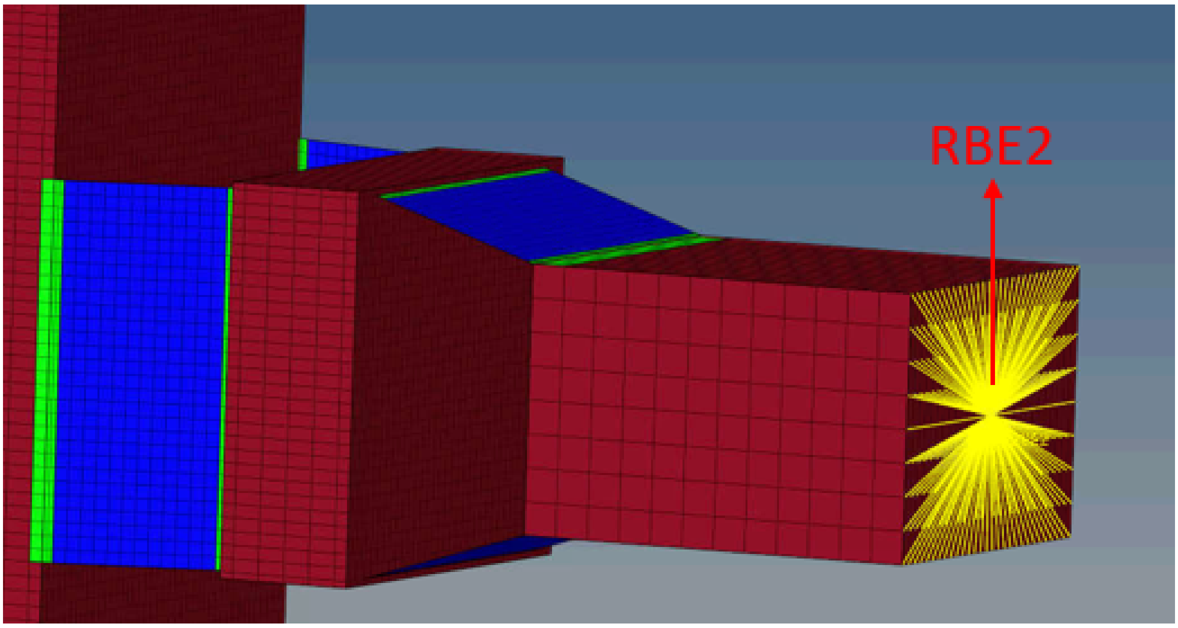

Figure 2.10. Corner of a single mechanism and the RBE2 element used to apply boundary condition.

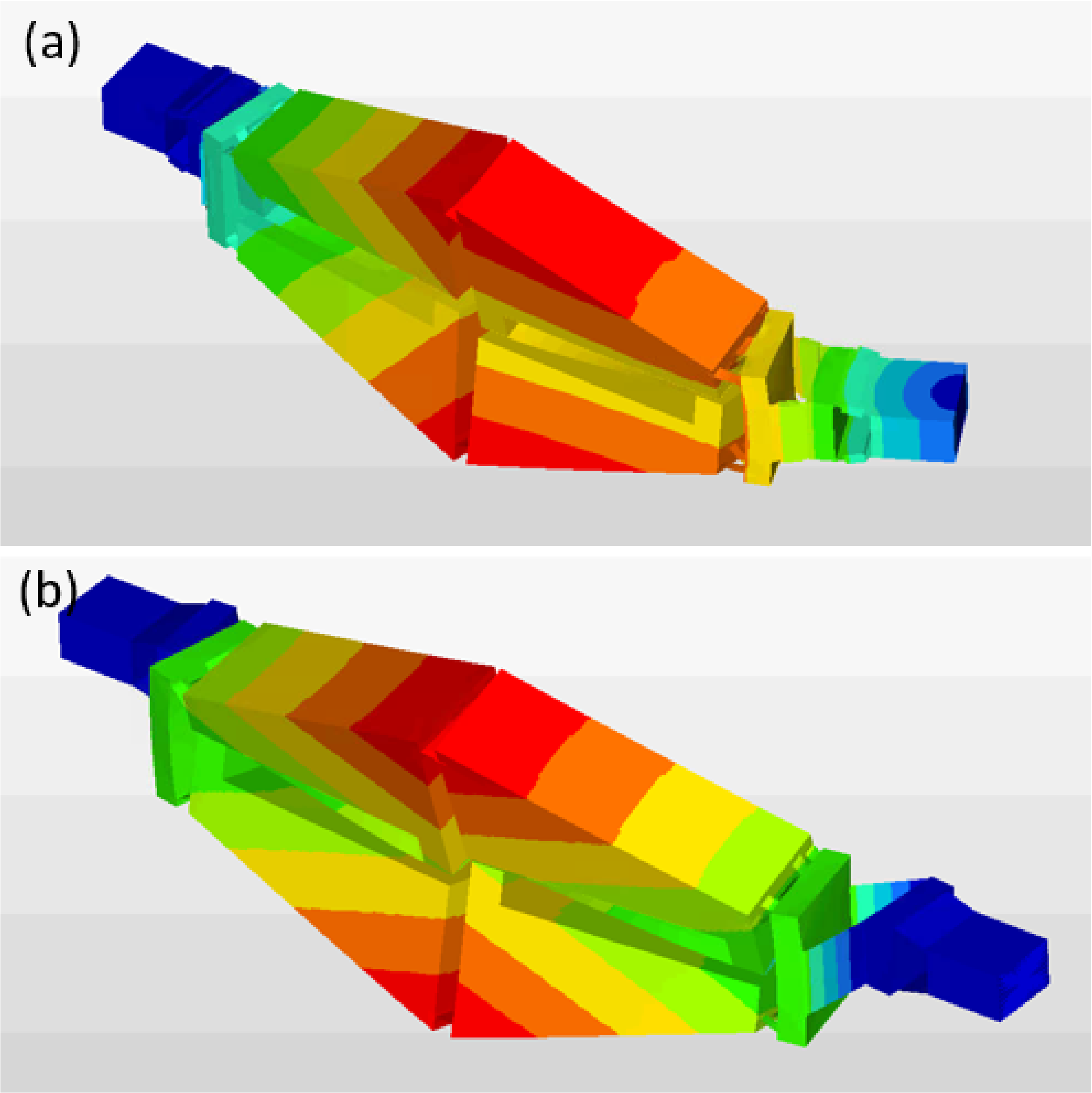

Figure 2.11. a) Boundary condition directly applied to the surface. b) Boundary condition applied to the master node of RBE2 element.

Mode shapes of the inertial amplification mechanism under these three boundary conditions are shown in the Figures 2.12, 2.13 and 2.14

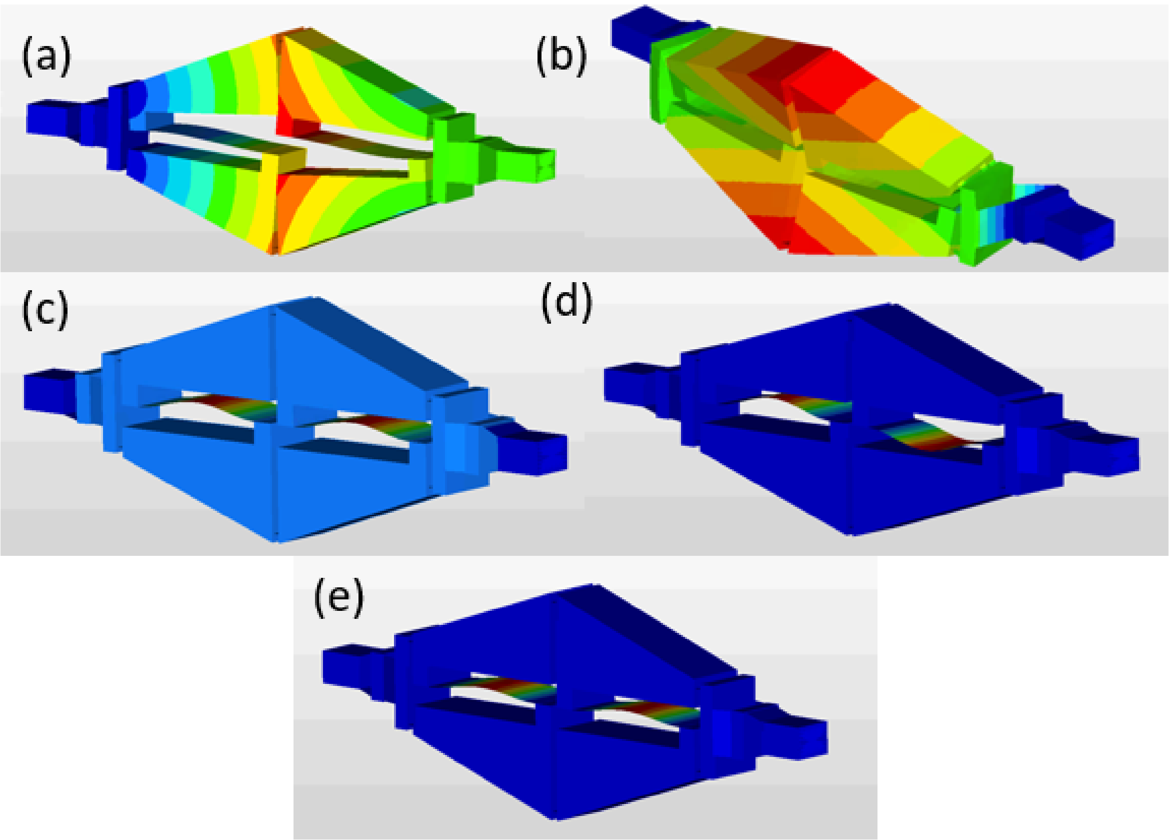

Figure 2.12. a) 1st (16.93 Hz) b) 2nd (468.05 Hz) c) 3rd (551.23 Hz) d) 4th (637.52 Hz) e) 5th (760.15 Hz) mode shapes of the inertial amplification mechanism under fixed-axially free boundary condition.

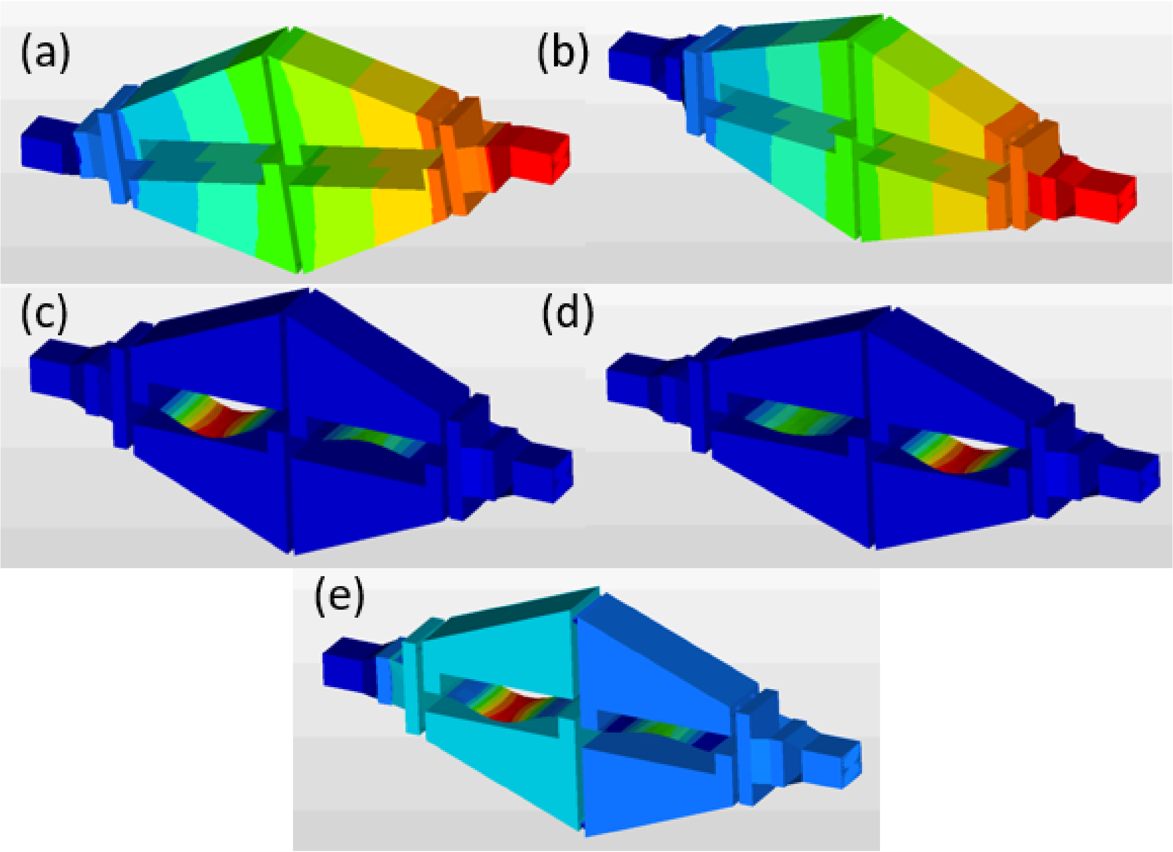

Figure 2.13. a) 1st (31.06 Hz) b) 2nd (48.52 Hz) c) 3rd (634.99 Hz) d) 4th (637.52 Hz) e) 5th (760.15 Hz) mode shapes of the inertial amplification mechanism under fixed-axially fixed boundary condition.

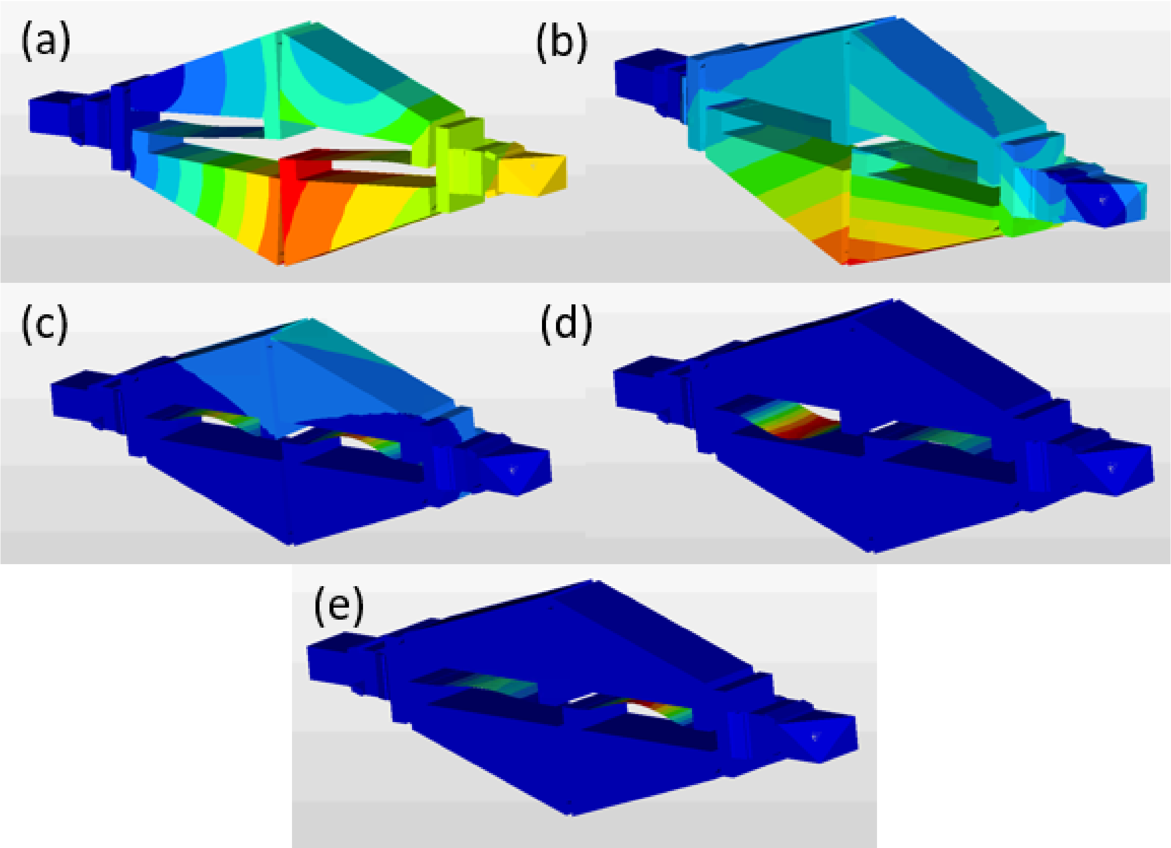

Figure 2.14. a) 1st (28.29 Hz) b) 2nd (482.41 Hz) c) 3rd (621.41 Hz) d) 4th (635.40 Hz) e) 5th (647.62 Hz) mode shapes of the inertial amplification mechanism under fixed-diagonally free boundary condition.

Natural frequencies of the mechanism under mentioned boundary conditions are given in Table 2.2.

Table 2.2. Natural frequencies of an inertial amplification mechanism under fixed-axially free, fixed-axially fixed , fixed-diagonally free boundary conditions.

Mode Numbers /Boundary Conditions	Fixed - Axial Free	Fixed - Axial Fixed	Fixed - Diagonally Free
1st mode	16.93	31.06	28.29
2nd mode	468.05	48.52	482.41
3rd mode	551.23	634.99	621.41
4th mode	635.51	637.52	635.40
5th mode	640.09	760.15	647.62

Table 2.2 shows that a large frequency gap is obtained at different ranges depending on the boundary conditions. Moreover, the limiting mode shapes are not the same. Since the natural frequencies are differing too much and the motions may not be similar to the periodic structure, it would not be safe to conduct design improvement studies on a single unit.

Connecting the single mechanisms in 3D is directly made on mesh model using a FEM modeling tool. 12 mechanisms are connected to each other in from their corners to obtain an octahedron shape. To connect each mechanism a corner component is added to the model. Corner component is obtained by intersecting four mechanism perpendicular to each other and extracting the faces. After face extraction, obtained 2D mesh is used to create a surface. By cleaning up the surfaces and meshing the corner part is obtained.

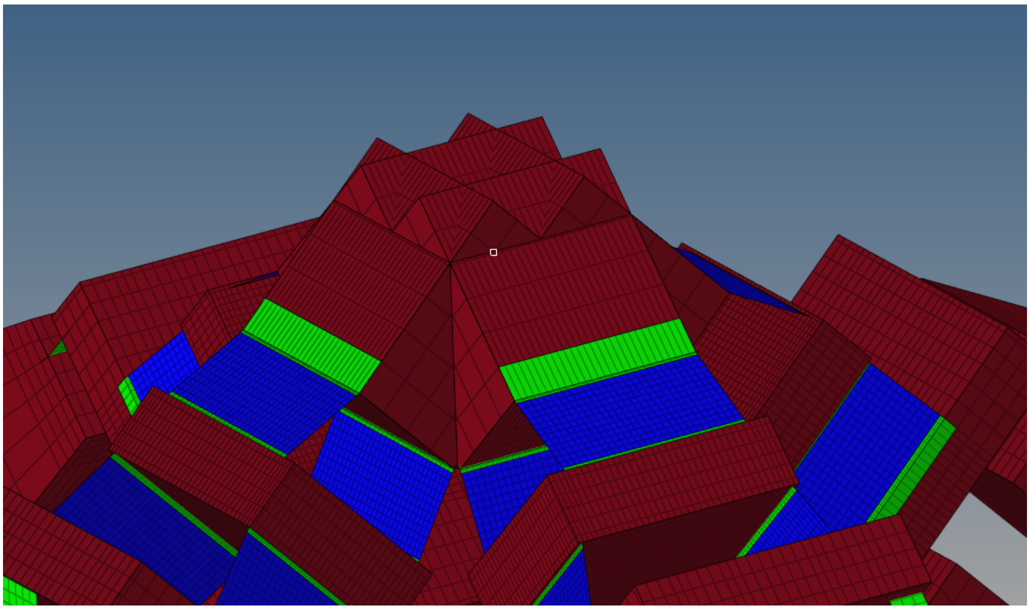

Figure 2.15. Positioning of four mechanism perpendicular to each other, intersecting at the midpoint of their corner.

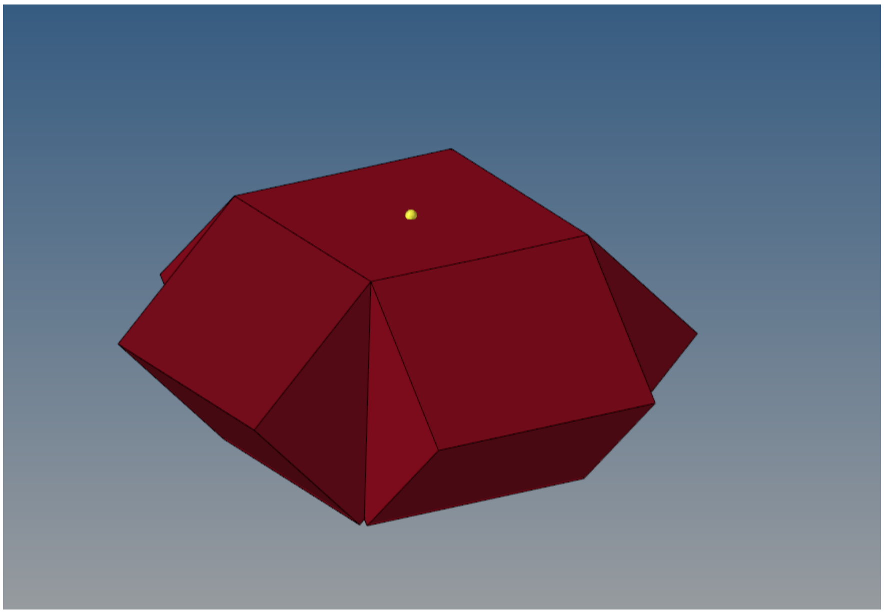

Figure 2.16. Obtained surfaces after face extraction and clean up procedures.

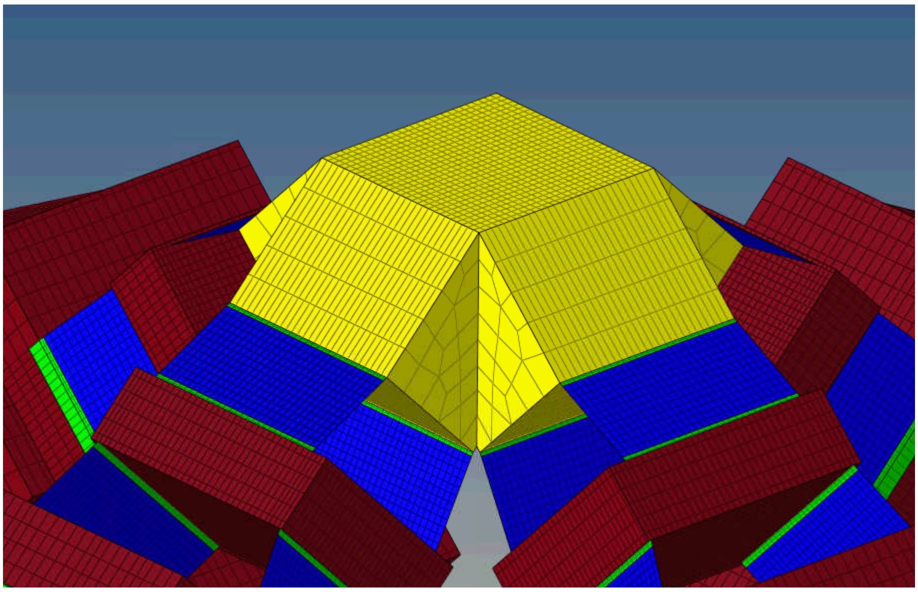

Figure 2.17. Properly meshing the of the corner part such that the nodes on the mechanisms can be equalized.

Positioning of the mechanisms can be done either perpendicular or horizontal. Both scenarios are modeled and analyzed to see which design has wider band gap. Mesh models of octahedron structures with perpendicular and horizontal mechanism are shown in Figure 2.27. As shown in Table 2.3 both layouts has the band gap between 12th and 13th natural frequencies. Perpendicular layout has ratio of upper limit of the band gap to the lower limit as 7.83 while the horizontal layout has ratio of 9.32. Therefore, horizontal layout is used for the further analyses.

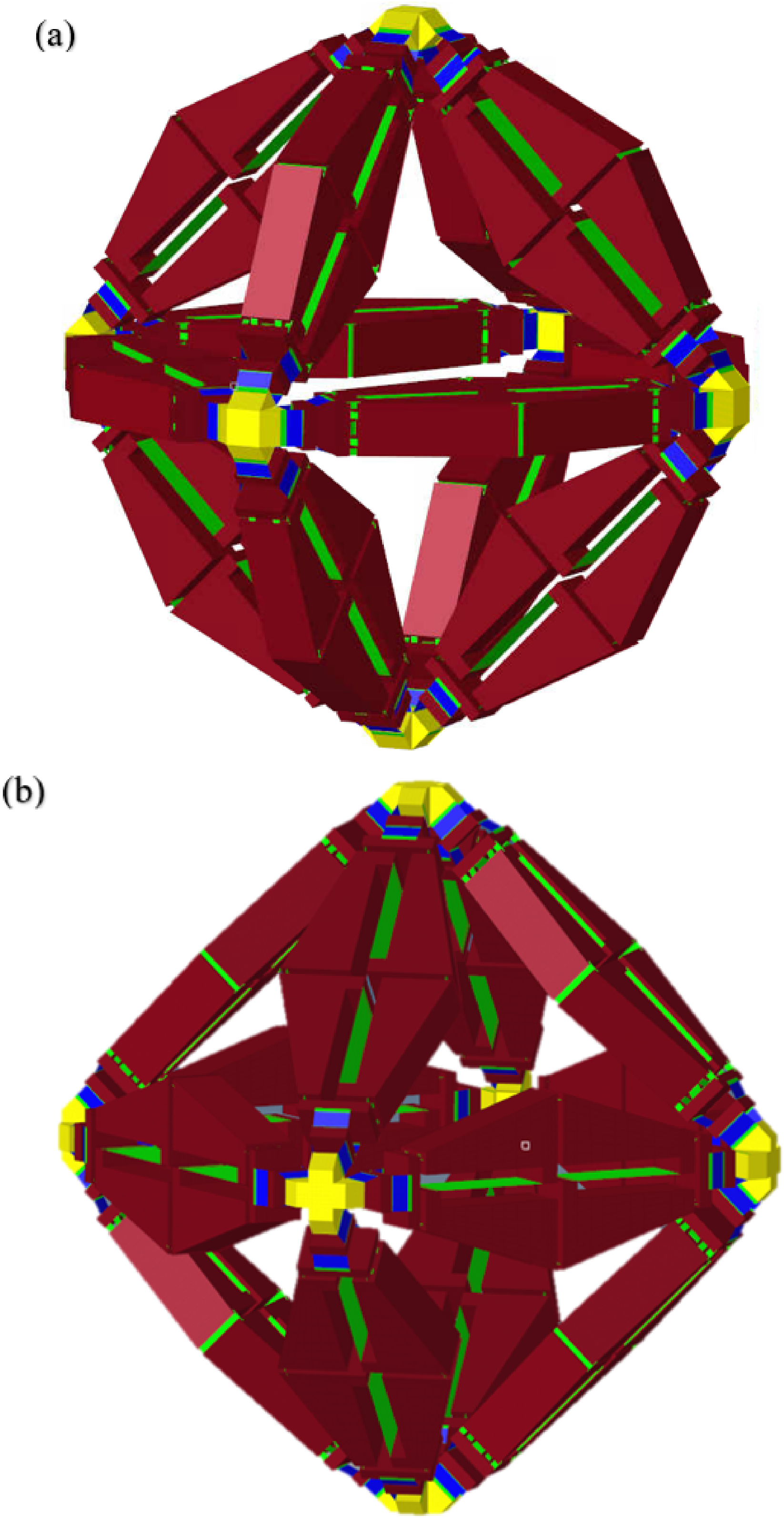

Figure 2.18. Octahedron structure with (a) perpendicular (b) horizontal mechanism layouts.

Table 2.3. Natural frequencies of octahedron structures with different mechanism layouts subject to free boundary conditions. Band gap is between 12th and 13th modes.

Mode Numbers	Perpendicular Layout (Hz)	Horizontal Layout (Hz)
1	16.72	16.73
2	20.60	20.04
3	21.21	20.05
4	21.71	20.05
5	23.40	23.98
6	24.00	23.98
7	24.09	23.98
8	24.13	32.28
9	24.14	32.28
10	38.44	32.29
11	38.57	32.32
12	38.73	32.33
13	303.32	301.45
14	309.62	301.49
15	314.16	301.59
16	334.92	371.87
17	338.76	371.91
18	344.55	371.94
19	389.82	381.00
20	391.69	381.03

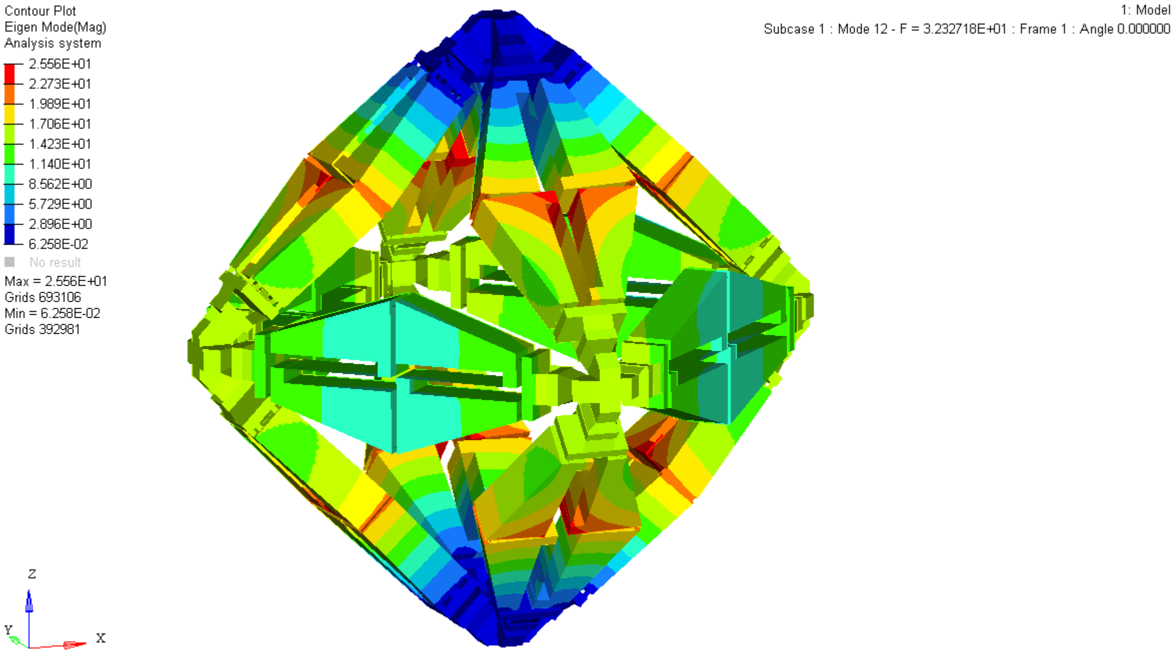

Figure 2.19. 12th mode shape of octahedron structure (32.33 Hz).

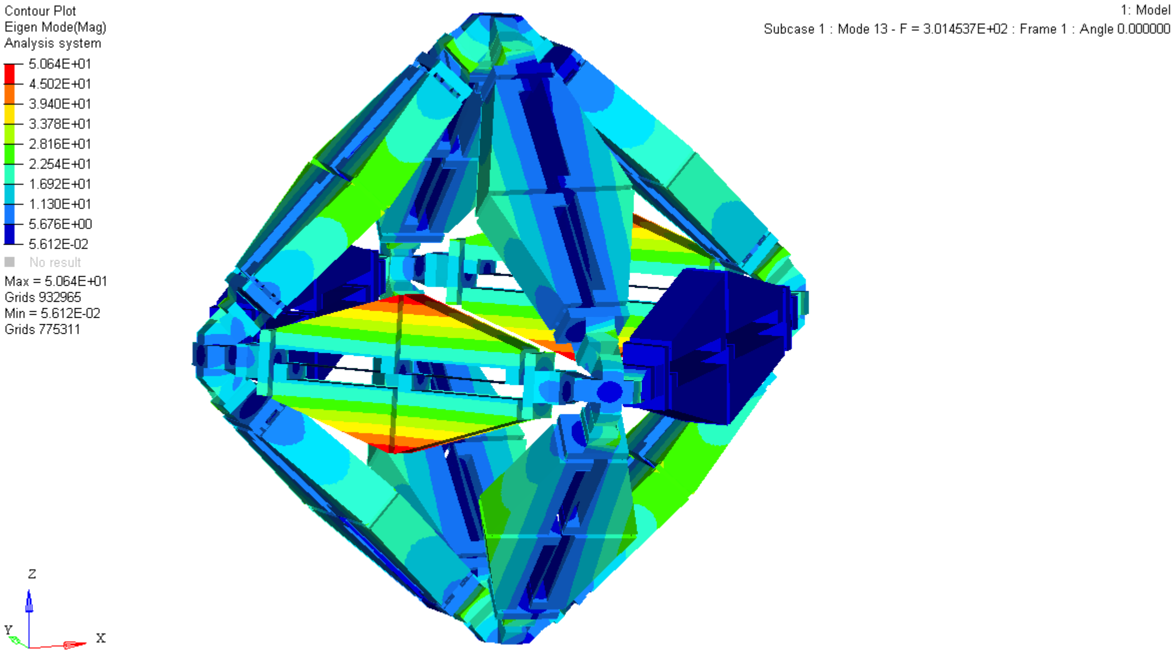

Figure 2.20. 13th mode shape of octahedron structure (301.43 Hz).

Mode shapes below and above the band gap are shown in Figures 2.19 and 2.20. In 12th mode shape each mechanism displays similar motion to the 1st mode shape of a single mechanism. Each mechanism displays opening and closing motion. On the other hand, 13th mode consists of torsional motion of the mechanisms by elastic deformation of the remote center of rotation mechanism.

After completing the modal analysis, frequency response function of the system is calculated by exciting the system from bottom corner and reading displacement data from the top. Modal analysis of the system under fixed-axially free boundary conditions also conducted to incorporate the FRF results with the mode shapes and natural frequencies. Natural frequencies of the fixed-axially fixed system are shown in Table 2.4. 1st, 10th, 12th, 13th and 16th mode shapes are also shown in Figures 2.21, 2.22, 2.23, 2.24 and 2.25.

Table 2.4. Natural frequencies of the fixed-axially free octahedron structure.

Mode Number	**Frequency**
1	11.95
2	17.48
3	17.48
4	19.01
5	20.05
6	20.76
7	20.76
8	26.57
9	26.57
10	27.98
11	30.73
12	32.29
13	32.33
14	320.13
15	320.74
16	369.56
17	384.00
18	438.13
19	438.96
20	467.39

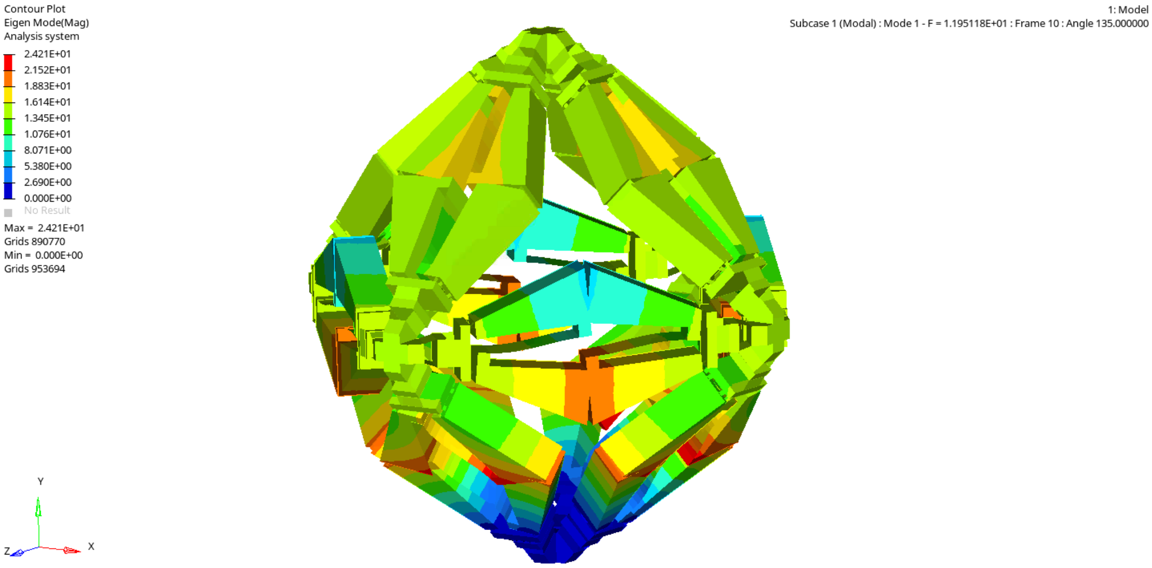

Figure 2.21. 1st mode shape of fixed- axially free octahedron structure (11.95 Hz).

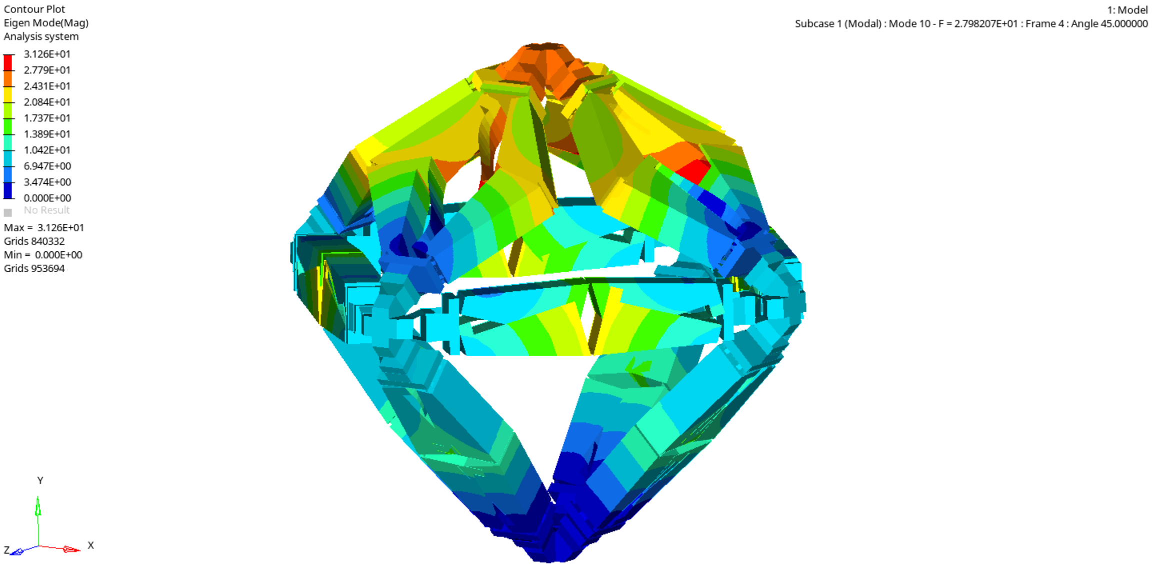

Figure 2.22. 10th mode shape of fixed- axially free octahedron structure (27.98 Hz).

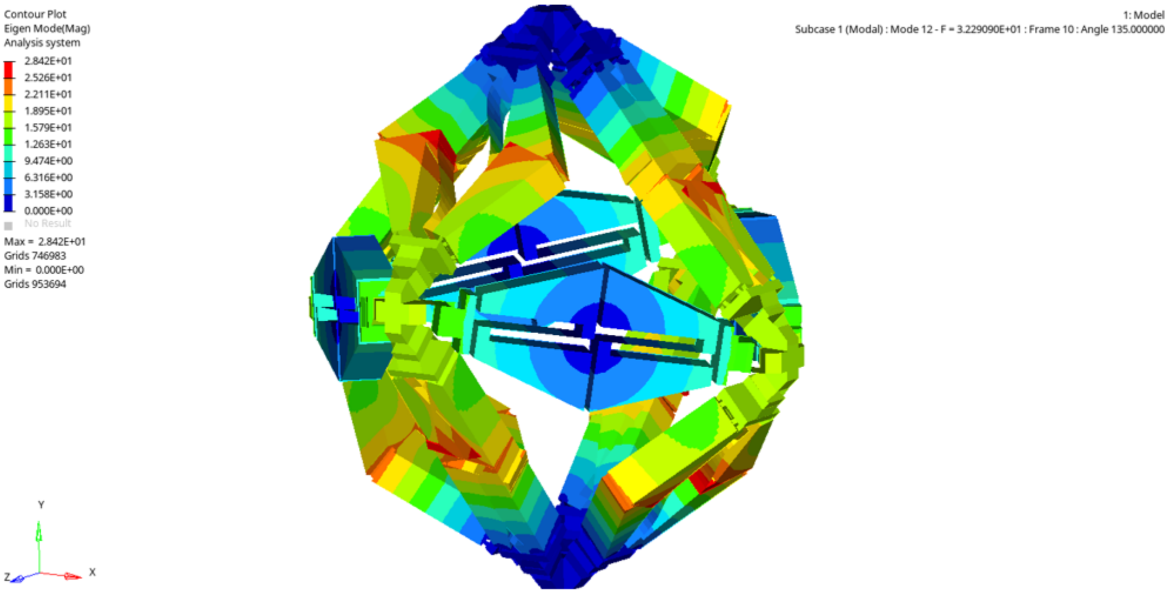

Figure 2.23. 12th mode shape of fixed- axially free octahedron structure (32.29 Hz).

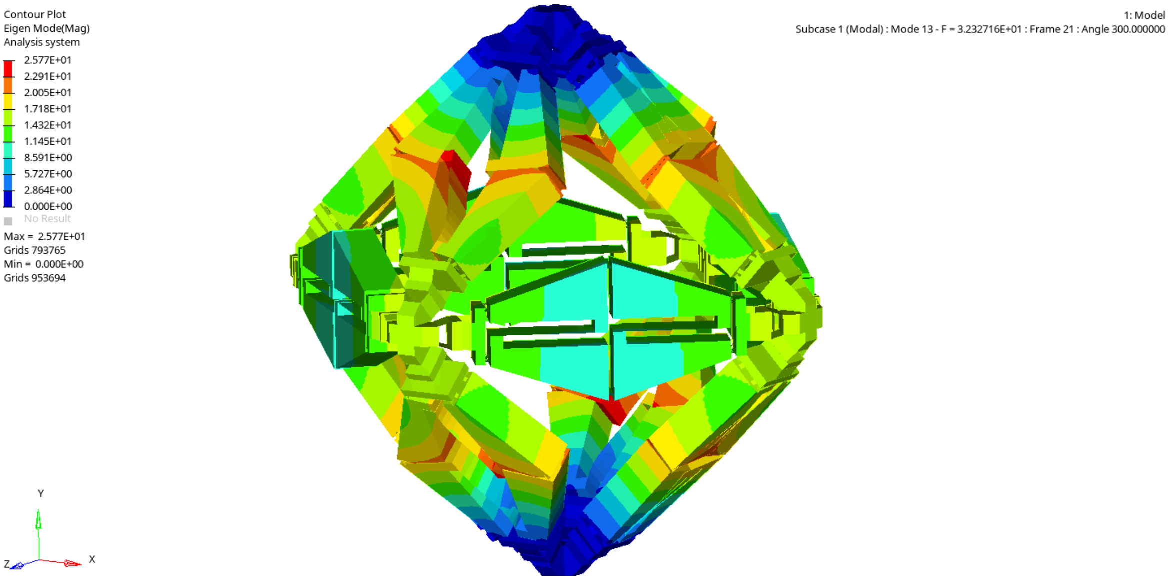

Figure 2.24. 13th mode shape of fixed- axially free octahedron structure (32.33 Hz).

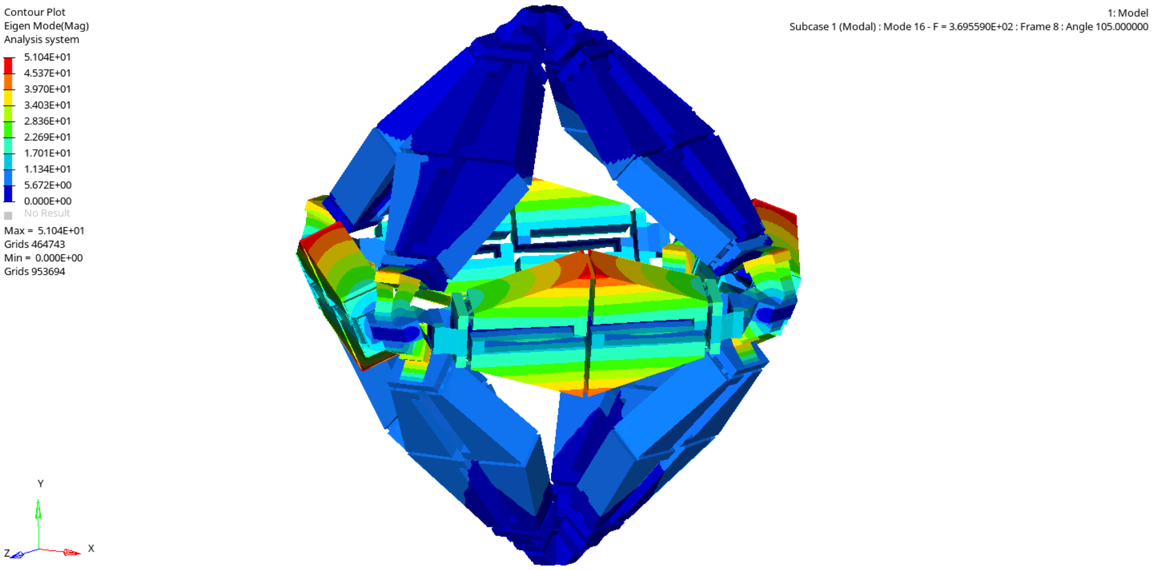

Figure 2.25. 16th mode shape of fixed- axially free octahedron structure (369.56 Hz).

From the mode shapes, it is observed that the top corner of the octahedron shows relatively small movement between 10th and 16th natural frequencies. This situation can also be observed from the displacement versus frequency results of the FRF analysis. By applying 1% material damping and unit displacement in vertical direction from the bottom and measuring displacement from the top graph in Figure 2.26 is obtained.

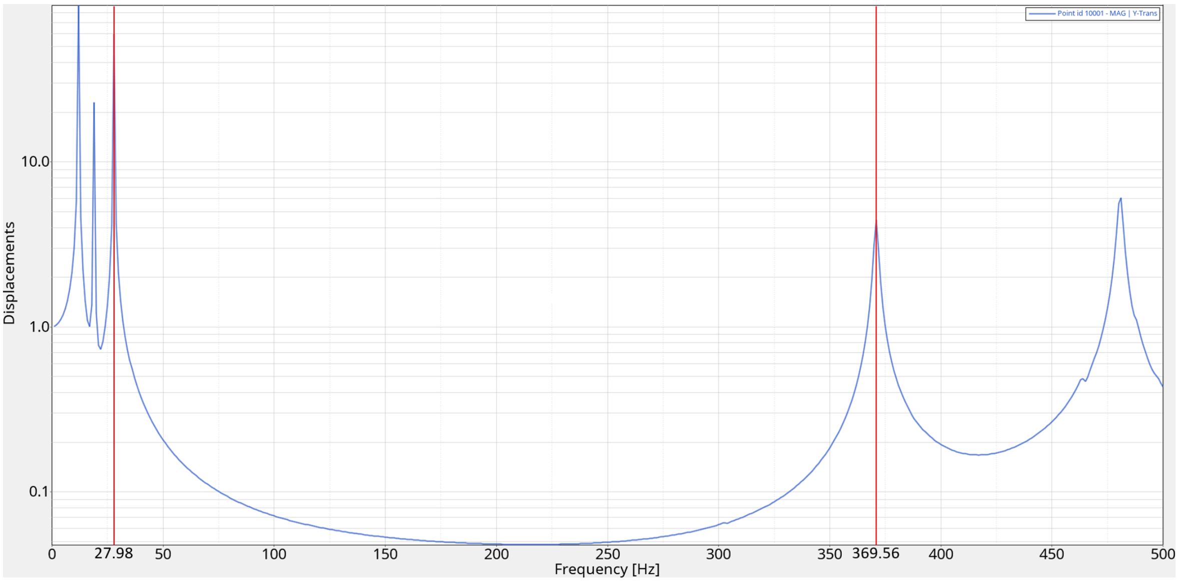

Figure 2.26. Vertical displacement of the top corner when unit displacement is applied from the bottom between 0-500 Hz.

As shown in Figure 2.26, the peaks below and above the band gap frequencies coincide with the 10th and 16th natural frequencies of the octahedron structure. However, there is an ambiguous point to mention, because the displacement is measured from right in the middle of the corner, axial motion caused by rotation of the corner cannot be seen from this measurement. Because the corner is relatively small compared to rest of the structure, this motion is neglected.

To model the inertial amplification mechanism periodically in 3D space six octahedron mechanisms are brought together to form a lattice structure. To see the behavior of the 3x2 periodic octahedron structure, modal and FRF analysis are done on the system same as the single octahedron structure.

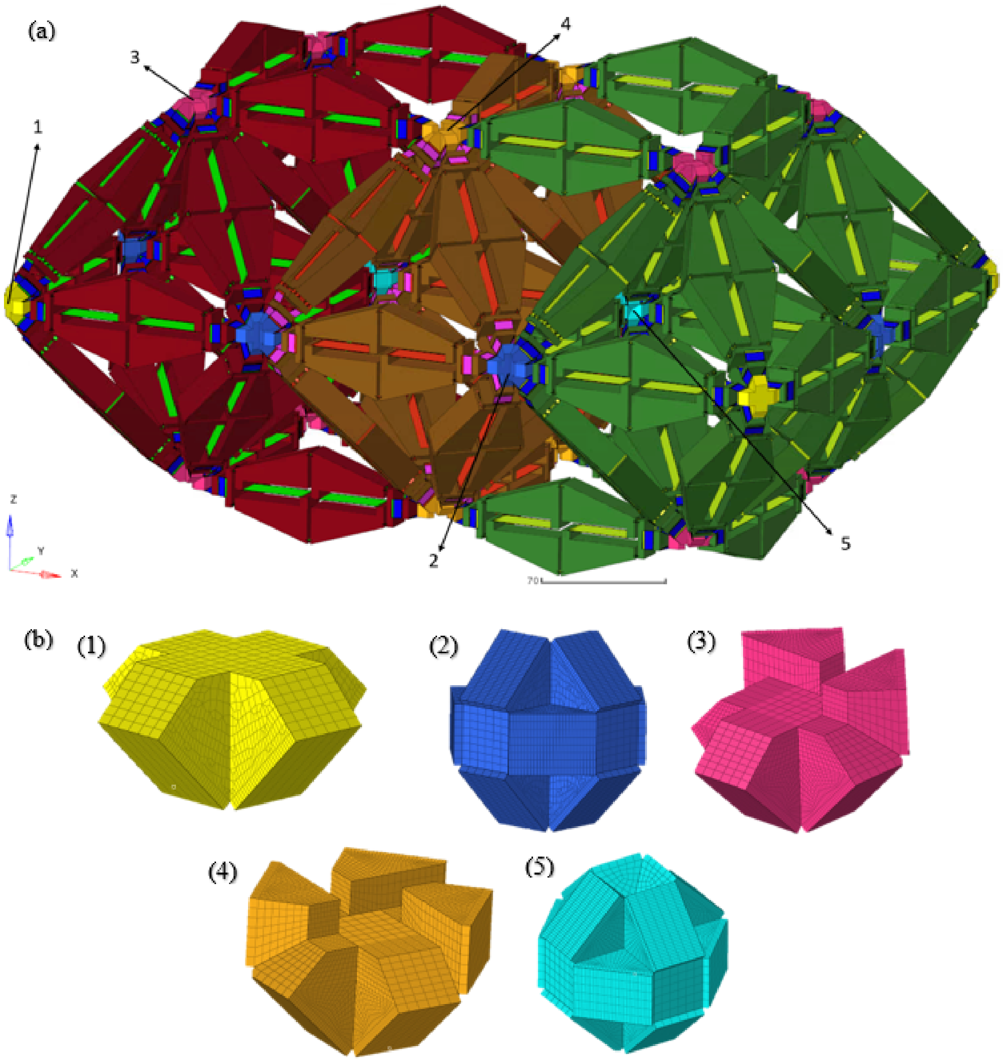

Figure 2.27. (a) FEM model of 3x2 periodical octahedron structure. (b) Corner components used to build up 3x2 periodical structure: (1) 4 piece corner connection, (2) 7 piece side connection, (3) 6 piece top-bottom side connection, (4) 7 piece top-bottom corner connection, (5) 12 piece inner connection.

Firstly model subject to free boundary condition is analyzed to see if there is an additional type of motion other than opening-closing and torsional motion, and the limiting frequencies of the band gap are found. After that the mechanism is fixed form one end to see the frequency response of the 3x2 periodic structure.

Table 2.5. Natural frequencies of 3x2 periodic octahedron subject to free boundary conditions.

Mode	**Freq.**	**Mode**	**Freq.**	**Mode**	**Freq.**	**Mode**	**Freq.**
1	11.26	21	21.71	41	27.69	61	33.84
2	14.16	22	21.85	42	27.99	62	34.45
3	14.32	23	22.36	43	28.05	63	34.84
4	14.42	24	22.99	44	28.08	64	34.95
5	15.61	25	23.45	45	28.85	65	35.38
6	15.76	26	23.61	46	29.68	66	36.16
7	16.41	27	23.82	47	29.89	67	288.73
8	17.21	28	23.92	48	30.21	68	302.68
9	18.03	29	25.08	49	30.42	69	304.26
10	18.08	30	25.66	50	30.56	70	314.04
11	18.41	31	25.80	51	30.58	71	324.44
12	18.43	32	25.90	52	30.94	72	333.86
13	18.54	33	26.07	53	31.16	73	336.84
14	18.81	34	26.45	54	31.88	74	338.95
15	19.01	35	26.83	55	32.63	75	358.45
16	19.24	36	26.86	56	32.71	76	380.31
17	21.20	37	26.92	57	32.77	77	382.75
18	21.42	38	27.16	58	32.92	78	395.63
19	21.47	39	27.40	59	33.31	79	396.53
20	21.55	40	27.51	60	33.73	80	401.44

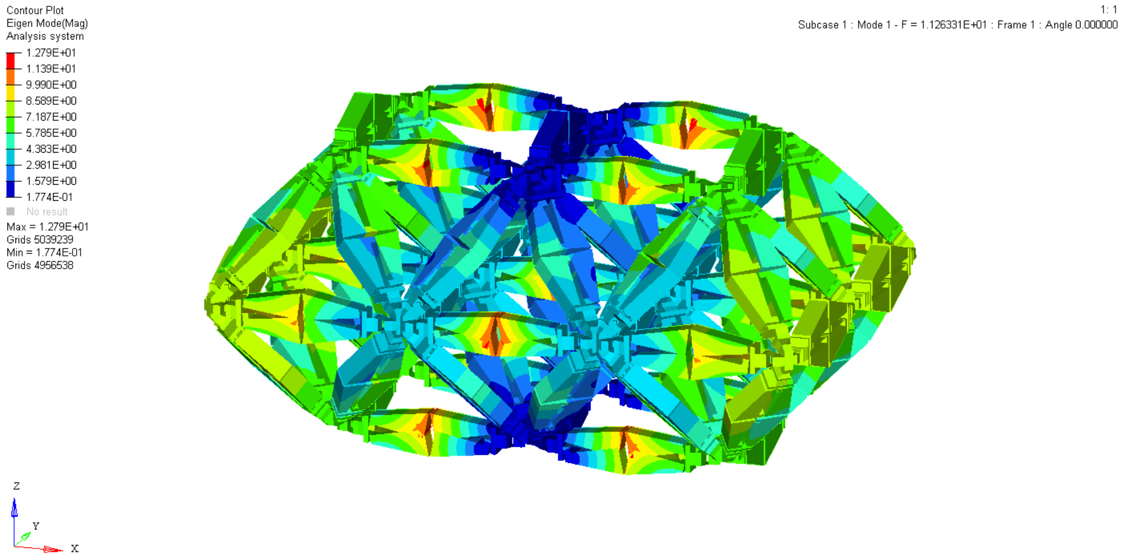

Figure 2.28. 1st mode shape of 3x2 periodic octahedron structure subject to free boundary conditions (11.26 Hz).

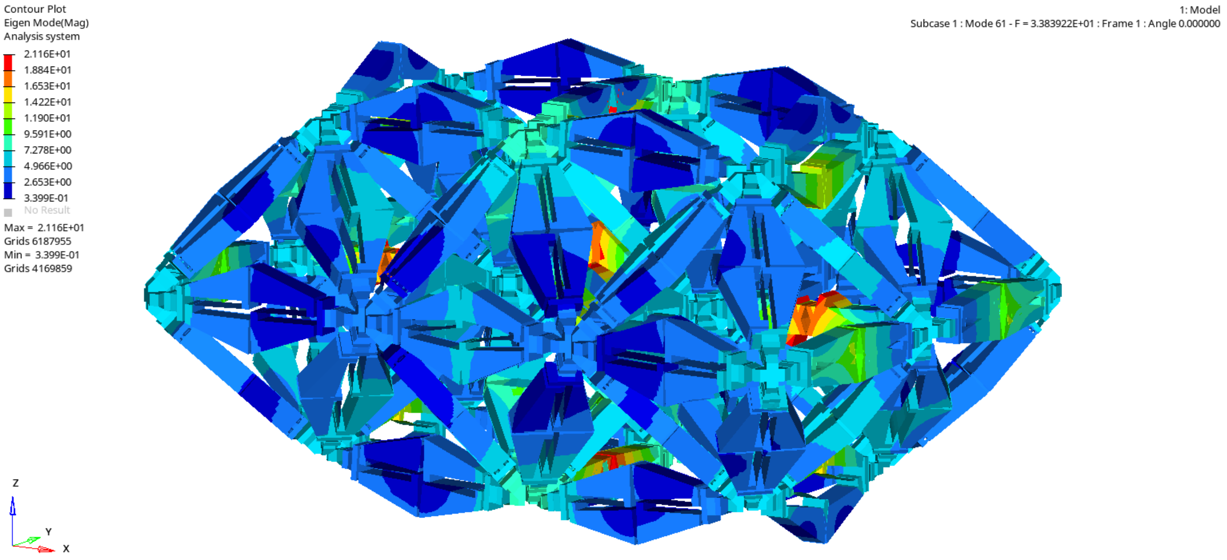

Figure 2.29. 61st mode shape of 3x2 periodic octahedron structure subject to free boundary conditions (33.84 Hz).

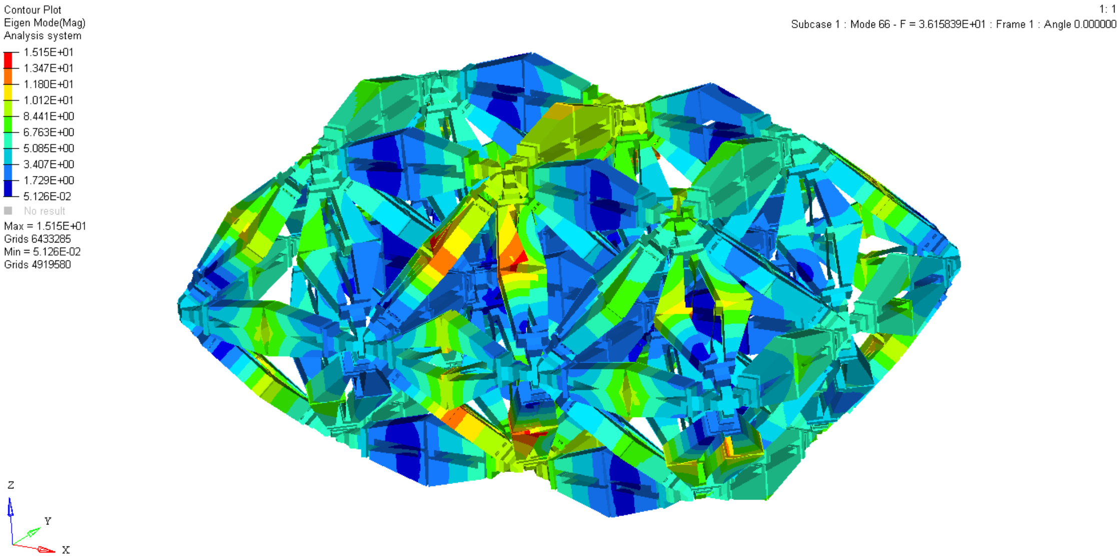

Figure 2.30. 66th mode shape of 3x2 periodic octahedron structure subject to free boundary conditions (36.16 Hz).

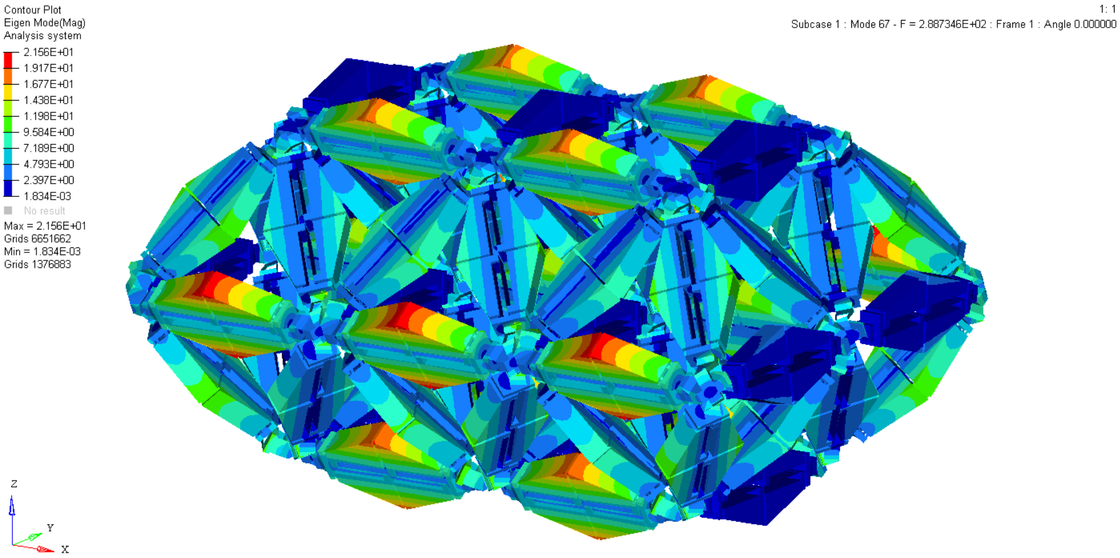

Figure 2.31. 67th mode shape of 3x2 periodic octahedron structure subject to free boundary conditions (288.73 Hz).

Similar to the octahedron structure, below the lower limit of the band gap, each mechanism displays opening-closing motion and above the upper limit of the band gap each mechanism displays torsional motion.

After calculating the natural frequencies of the 3x2 periodic system in free boundary conditions, fixed boundary condition is applied to one side and displacement data is measured from the other side as shown in Figure 2.32.

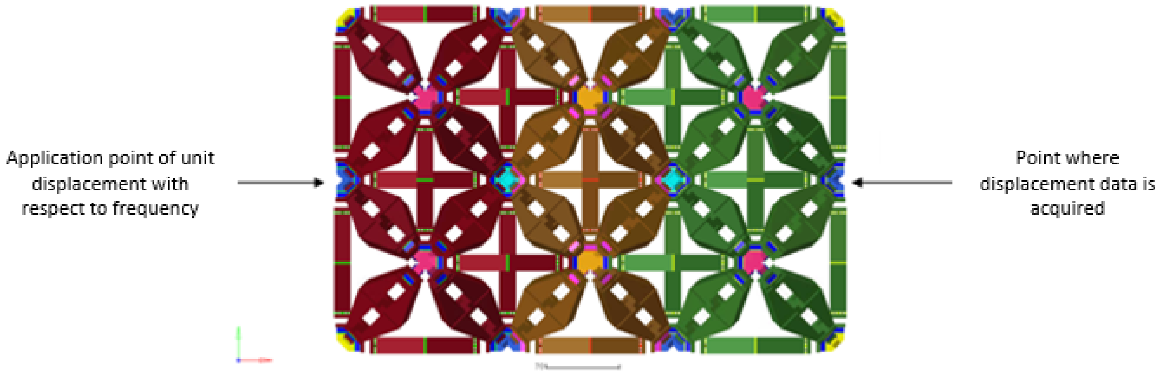

Application point of unit displacement with respect to frequency

Point where displacement data is acquired

Figure 2.32. Points of displacement application and data acquisition on 3x2 periodic octahedron structure.

Table 2.6. Natural frequencies of 3x2 periodic octahedron structure subject to fixed - axially free boundary conditions. Values indicated by red color are the frequencies inside the vibration isolation band.

Mode	**Freq.**	**Mode**	**Freq.**	**Mode**	**Freq.**	**Mode**	**Freq.**
1	4.98	21	20.47	41	26.96	61	33.56
2	7.72	22	21.08	42	27.34	62	33.63
3	8.27	23	21.28	43	27.41	63	34.13
4	10.27	24	21.78	44	27.72	64	34.49
5	12.69	25	22.07	45	27.85	65	34.73
6	13.03	26	22.52	46	28.63	66	35.05
7	13.30	27	23.50	47	28.87	67	35.62
8	14.16	28	23.73	48	29.18	68	299.76
9	16.51	29	23.78	49	29.66	69	311.63
10	16.61	30	23.82	50	30.01	70	329.80
11	17.09	31	24.60	51	30.22	71	333.43
12	17.63	32	24.67	52	30.44	72	338.27
13	18.35	33	25.34	53	30.59	73	346.92
14	18.47	34	25.67	54	30.91	74	355.36
15	18.70	35	25.88	55	31.12	75	359.57
16	18.89	36	25.97	56	31.26	76	390.26
17	18.93	37	26.05	57	31.71	77	395.33
18	19.40	38	26.17	58	32.72	78	396.64
19	19.77	39	26.46	59	32.72	79	401.76
20	20.09	40	26.93	60	32.81	80	402.20

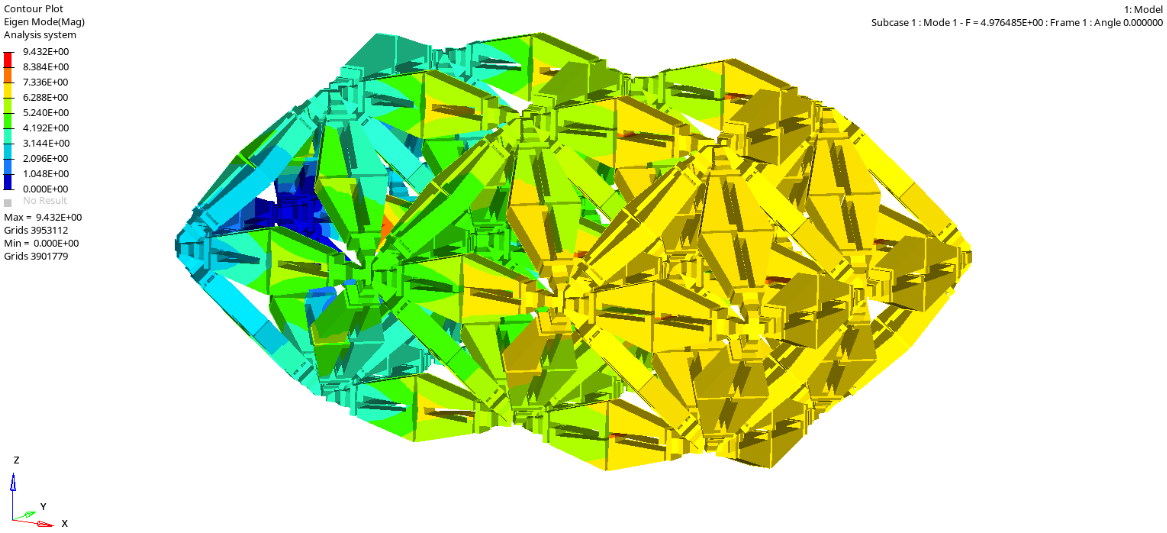

Figure 2.33. 1st mode shape of 3x2 periodic octahedron structure subject to fixed - axially free boundary conditions (4.98 Hz).

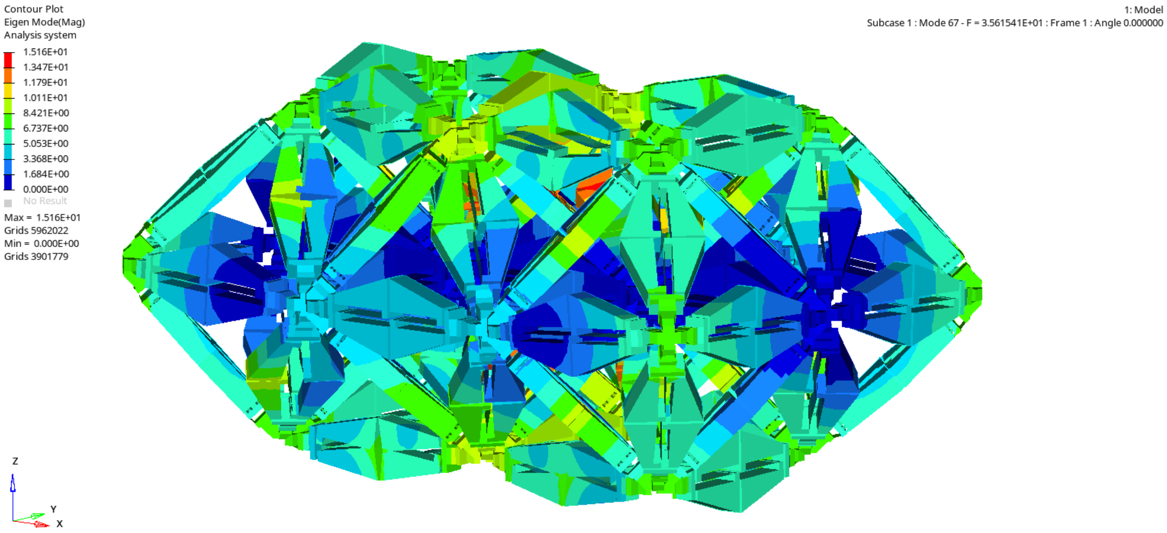

Figure 2.34. 67th mode shape of 3x2 periodic octahedron structure subject to fixed - axially free boundary conditions (35.62 Hz).

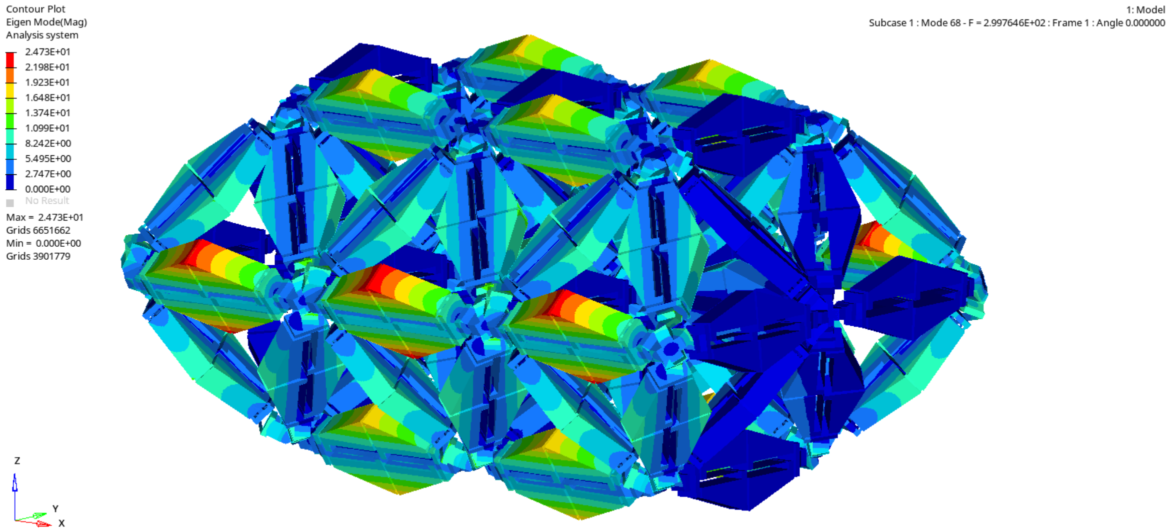

Figure 2.35. 68th mode shape of 3x2 periodic octahedron structure subject to fixed - axially free boundary conditions (299.76 Hz).

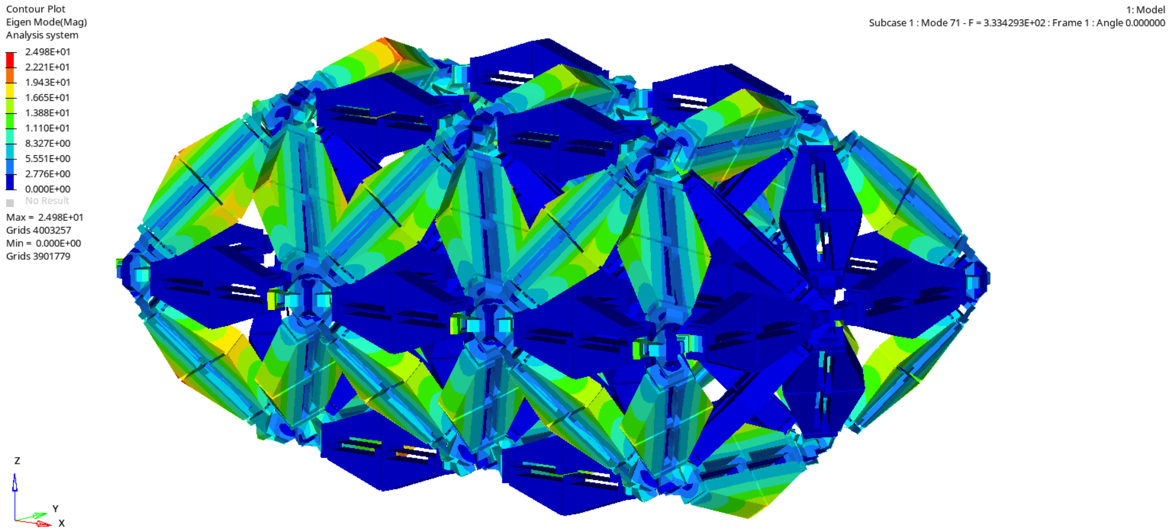

Figure 2.36. 71st mode shape of 3x2 periodic octahedron structure subject to fixed - axially free boundary conditions (333.43 Hz).

After modal analysis, frequency response of the system is measured by applying 1% material damping.

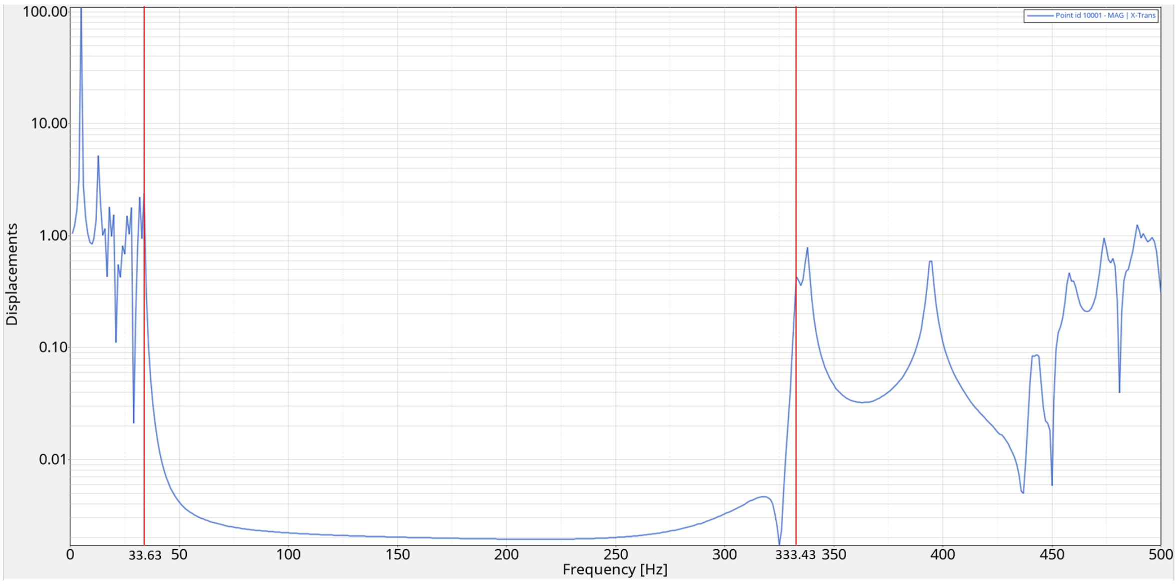

Figure 2.37. Frequency response function of 3x2 periodic octahedron in horizontal direction.

Additionally, excitation in vertical and horizontal directions are applied and their effect is calculated at the opposite corner as shown in Figure 2.38. As a result, it can be deduced that the system does have large isolation bandwidth in 3D.

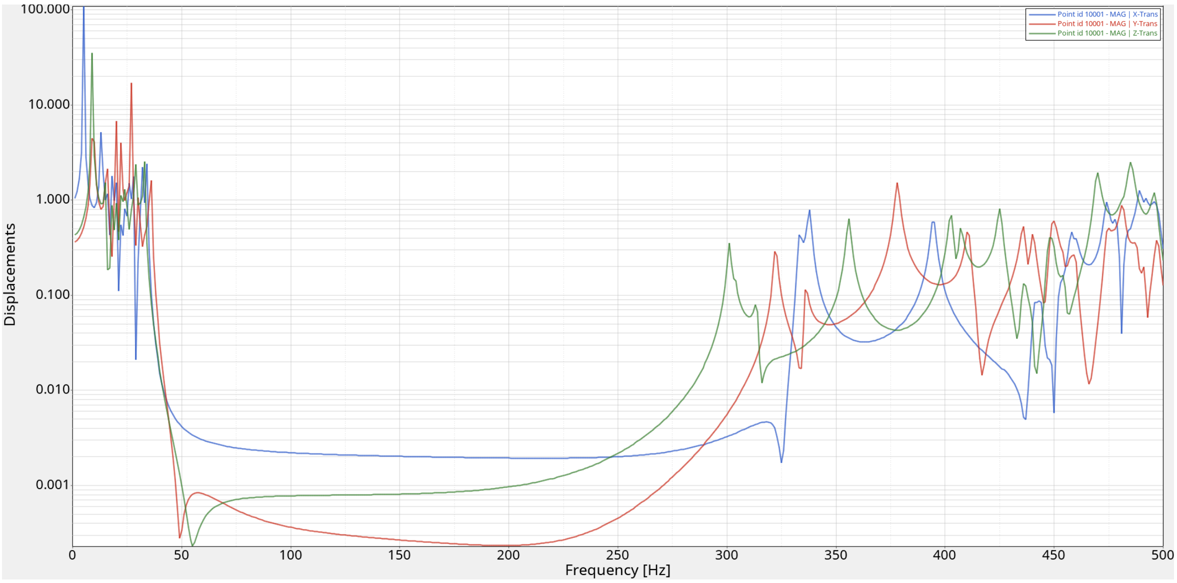

Figure 2.38. Frequency response function of 3x2 periodic octahedron obtained by exciting the structure x, y and z directions and obtaining outputs in the same directions.

When the mode shapes of 3x2 periodic system is observed it is seen that the mode shapes below the band gap display opening and closing motion while the mode shapes above the band gap display torsional motion. Considering the same behavior of the single octahedron structure it can be deduced that there is a correlation between the effect of a design change made on single octahedron structure and 3x2 periodic octahedron structure. Therefore design optimization studies are focused on improving the single octahedron structure.

3. PARAMETRIC STUDIES AND OPTIMIZATION

When mode shapes of a single inertial amplification mechanism is examined, while at the lower limit of the band gap, nodes at the center of the middle of the system are displaying relatively higher displacement, at the upper limit of the band gap the highest and lowest locations of the middle of the mechanism display highest displacement. Therefore, as center of gravity of the bulk parts get closer to the center, decrease in the 12th natural frequency and increase in the 13th natural frequency are expected.

To test this argument an analysis model is set up with differing regions of material density inside the mechanism as shown in Figure 3.1. Using each mechanism, an octahedron structure is prepared (see Figure 3.2) and their natural frequencies and mode shapes are calculated.

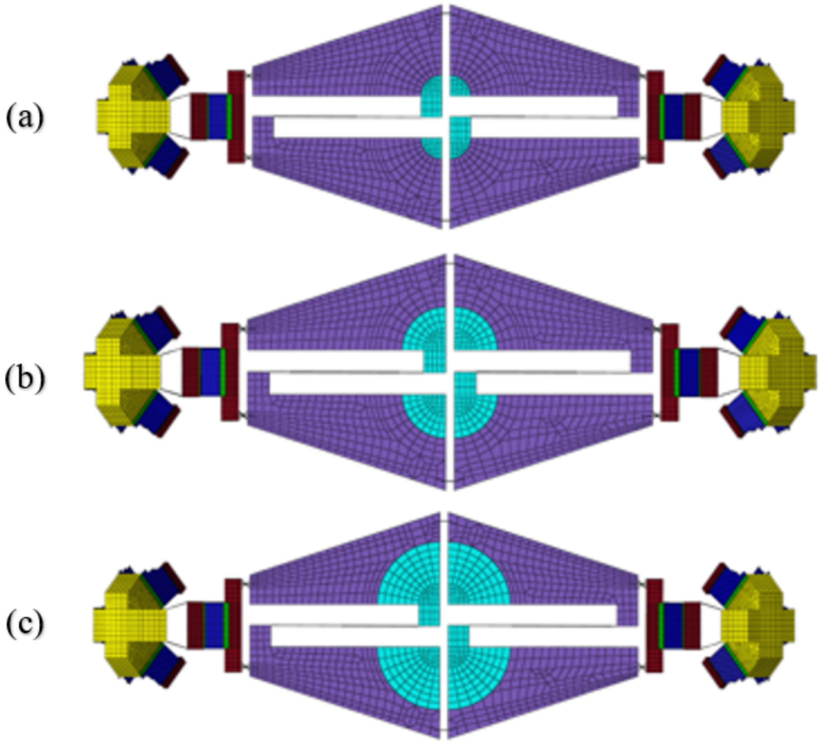

Figure 3.1. Inertial amplification mechanism designs with density modifications. Circular regions of a) 5 mm, b) 10 mm, c) 15 mm (turquoise) radius has three times increased density while the rest of the bulk parts (purple) has one third of the original density.

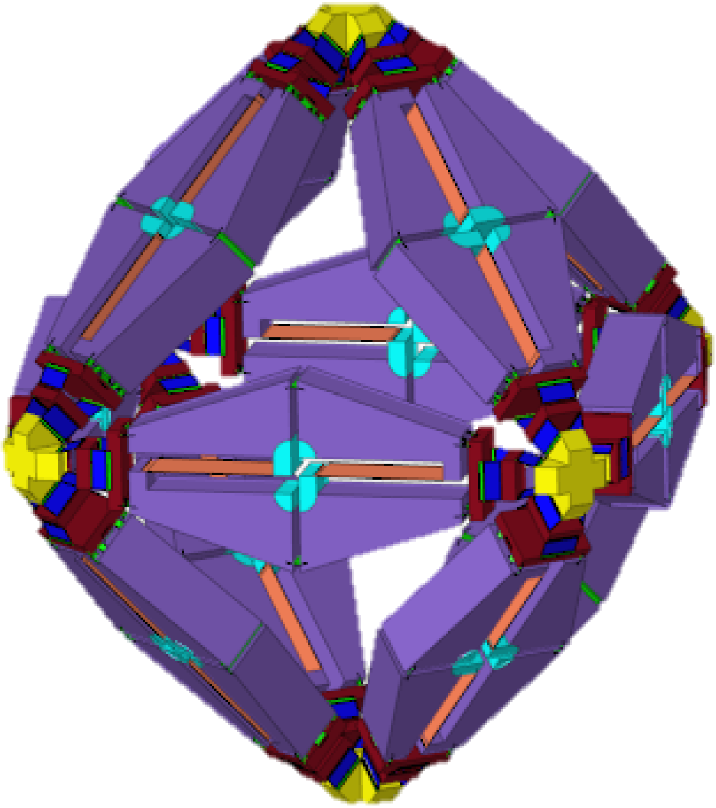

Figure 3.2. Octahedron structure made up of inertial amplification mechanisms with modified density regions.

In the mode shapes of the modal analysis results, it is observed that the upper limit of the band gap of some of the design iterations are determined by the bending modes of the long flexures between upper and lower bulk parts as shown in Figure 3.3.

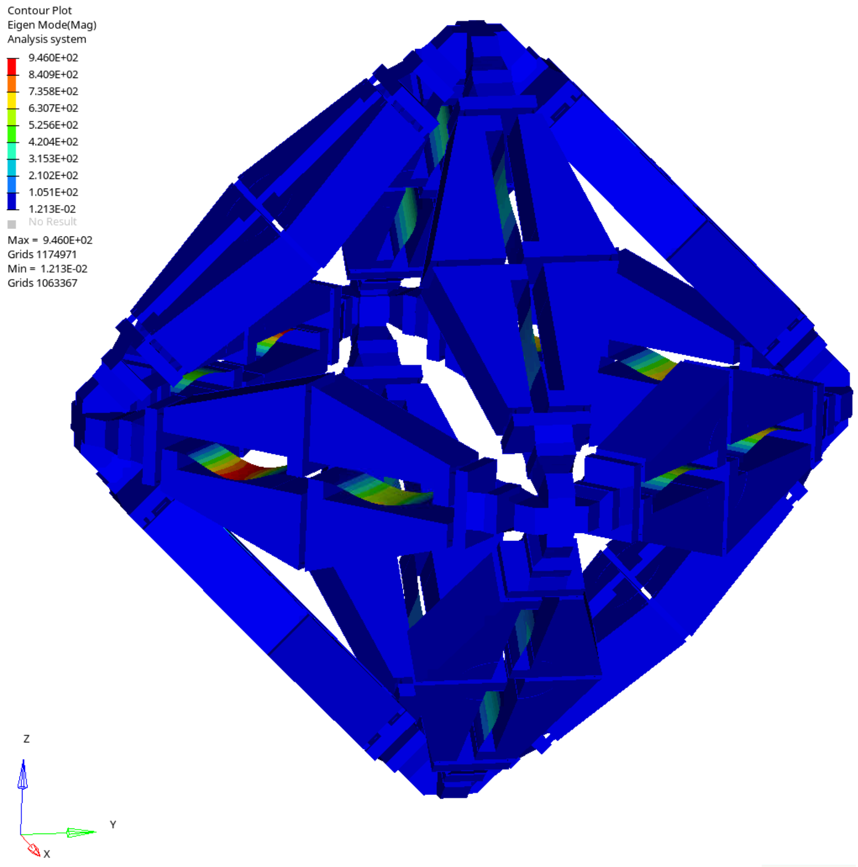

Figure 3.3. Bending mode of the long flexures.

As a solution, thicknesses of long flexures are updated to obtain the widest band gap. Thicknesses are changed to 0.090 mm for Figure 3.1a, 0.115 mm for Figure 3.1b and 0.135 mm for Figure 3.1c from 0.100 mm. Natural frequencies of each design after long flexure thickness modification is given in Table 3.1. As can be seen from the table, limits of the band gap still resides between 12th and 13th natural frequencies meaning that only the natural frequency values are changed rather than mode shapes. Ratios of the upper and lower band frequencies can be calculated as 10.74, 11.81, 10.99 for the systems with 5mm, 10mm and 15mm radii circular central masses, respectively. The highest ratio is obtained for the 10mm radius circular central mass.

Table 3.1. Natural frequencies of octahedron structures with 5, 10 and 15 mm radius circular modified regions.

Mode No	**5 mm Frequencies**	**10 mm Frequencies**	**15 mm Frequencies**
1	20.01	15.27	11.87
2	27.46	21.69	17.33
3	27.46	21.7	17.33
4	27.48	21.71	17.34
5	29.3	22.86	18.19
5	29.3	22.86	18.19
7	29.3	22.86	18.2
8	39.67	32.32	26.33
9	39.67	32.32	26.33
10	45.31	36.79	29.96
11	45.32	36.8	29.97
12	45.33	36.81	29.97
13	486.77	423.51	329.38
14	487.44	423.63	329.5
15	487.7	423.87	329.71
16	558.23	483.02	382.56
17	558.3	483.1	382.57
18	558.37	483.17	382.59
19	558.41	483.24	382.6
20	558.49	483.25	382.63

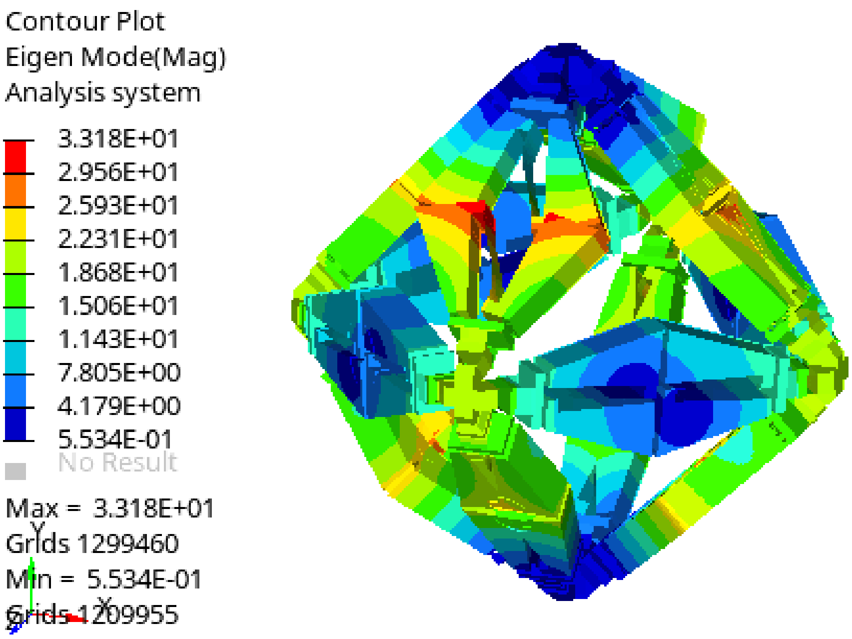

Figure 3.4. 12th mode shape of the 10 mm radius of modified density region model (36.81 Hz).

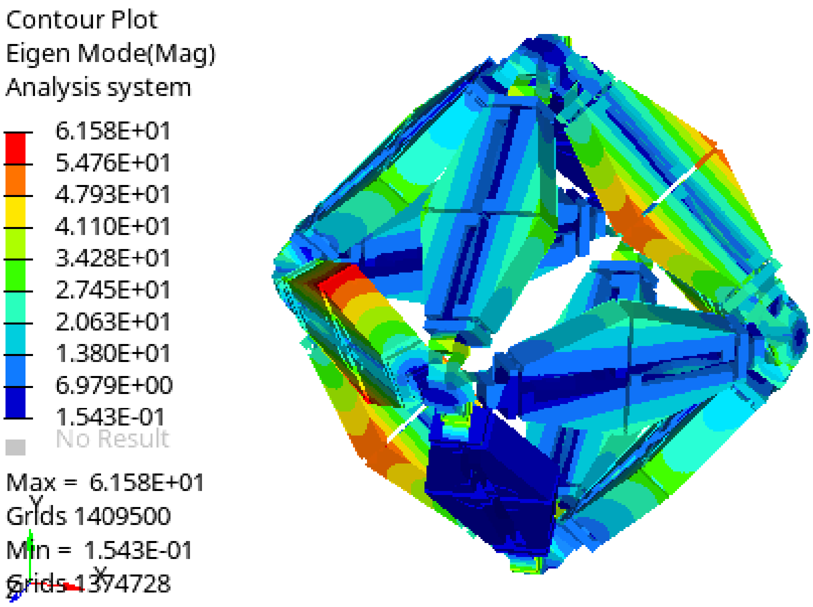

Figure 3.5. 13th mode shape of the 10 mm radius of modified density region model (423.51 Hz).

After validating the positive effect of gathering the mass close to the center, bulk parts of the mechanism are modified such that the materials away from the center regions are removed as shown in Figure 3.6. To eliminate the slight out-of-plane motion observed in 13th mode of the mass modified mechanism as shown in Figure 3.5, short flexures are separated from the middle and shifted to the sides without changing the total length.

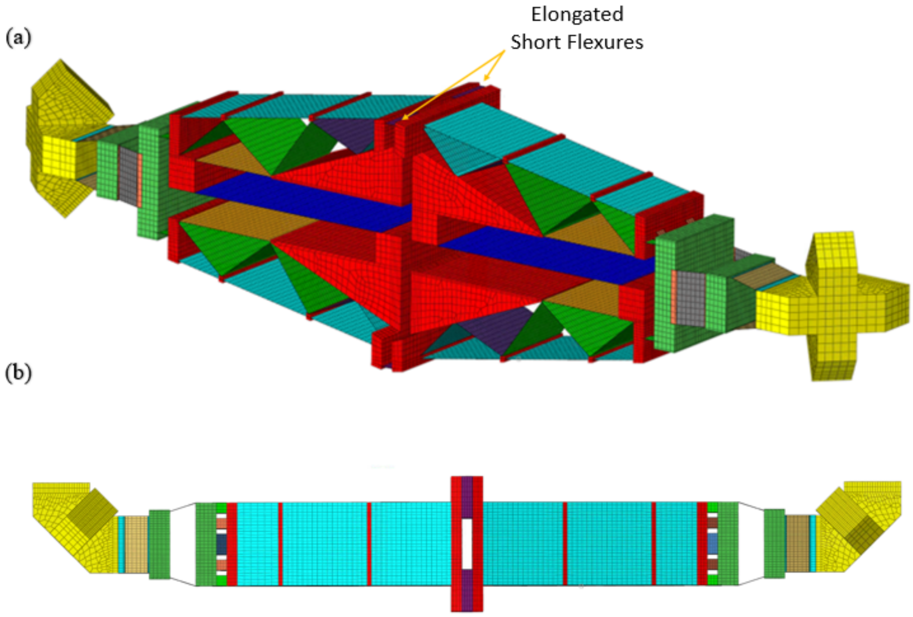

Figure 3.6. Modified inertial amplification mechanism with removed material and elongated short flexures a) isometric view, b) top view.

When the new system is assembled into an octahedron and analyzed, natural frequencies are obtained as in the Table 3.2.

Table 3.2. Natural frequencies of octahedron structure with mass optimized inertial amplification mechanism.

Mode Number	**Frequency**
1	20.56
2	26.48
3	26.49
4	26.58
5	26.94
6	26.95
7	27.16
8	35.00
9	35.06
10	40.20
11	40.29
12	40.29
13	510.48
14	511.41
15	512.09
16	535.76
17	536.82
18	540.97
19	549.54
20	549.81

In the new model, band gap is still observed between 12th and 13th natural frequencies and the ratio of the upper and lower band gap limits is calculated as 12.67. Mode shapes of the 12th and 13th natural frequencies are shown in Figures 3.7 and 3.8.

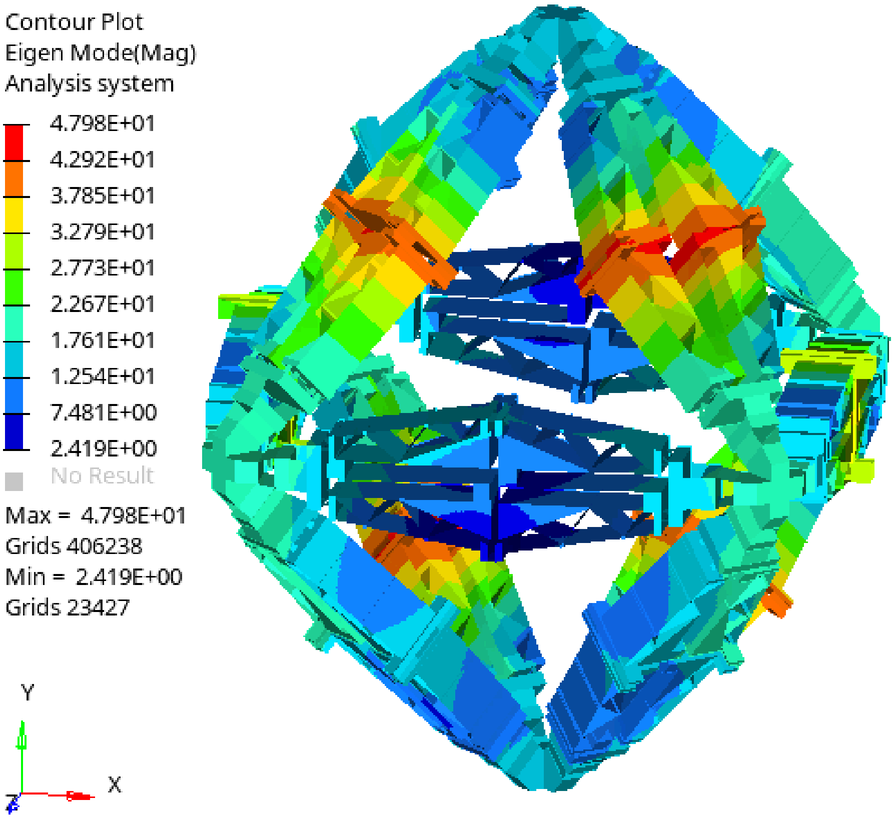

Figure 3.7. 12th mode shape of octahedron structure with truss supported inertial amplification mechanisms (40.29 Hz).

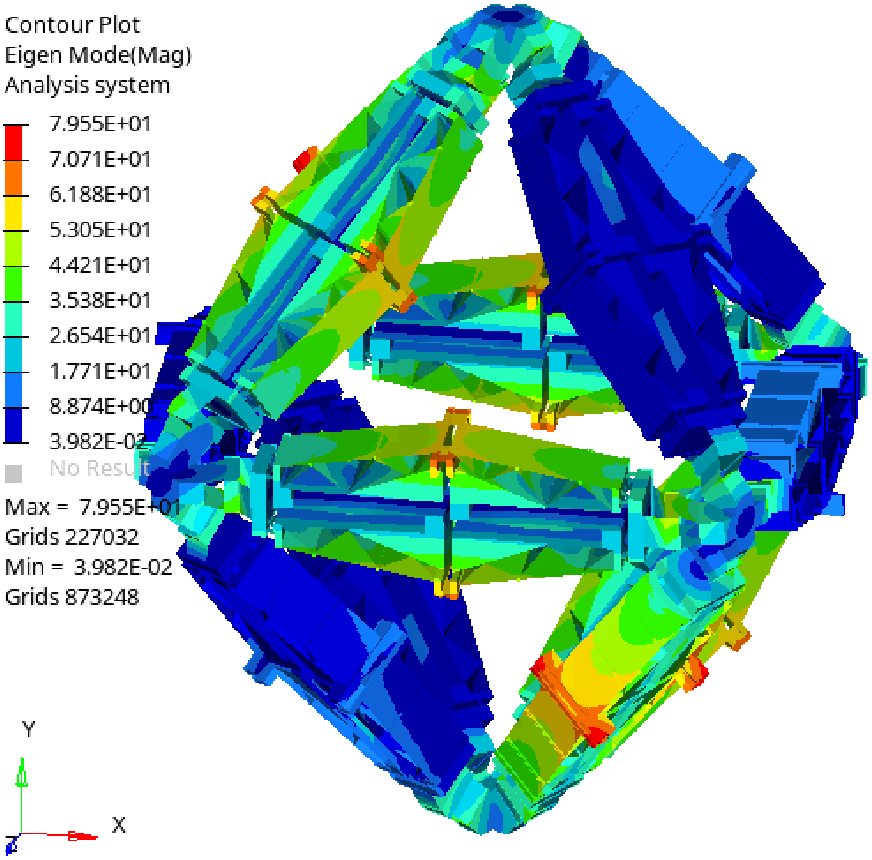

Figure 3.8. 13th mode shape of octahedron structure with truss supported inertial amplification mechanisms (510.48).

To further increase the band gap, thicknesses of shell components in the mechanism are defined as parameters and an optimization study is conducted. After a couple of iterations, it is observed that effect of thickness modifications on thin parts of remote center of rotation mechanisms, both cross flexure types and three truss components are in correlation separately. Therefore, these thickness values are gathered under single parameter for each group. As a result parameters can be defined as:

- Parameter-1: Thicknesses of truss members
- Parameter-2: Thicknesses of thin members of RCR mechanism
- Parameter-3: Thickness of straight flexures
- Parameter-4: Thickness of both cross flexures
- Parameter-5: Thickness of short flexure

The components that are represented by these parameters are shown in Figure 3.9. Each parameter are set to be varied between an upper and a lower bound value. These values are determined using manual iteration results and shown in Table 3.3.

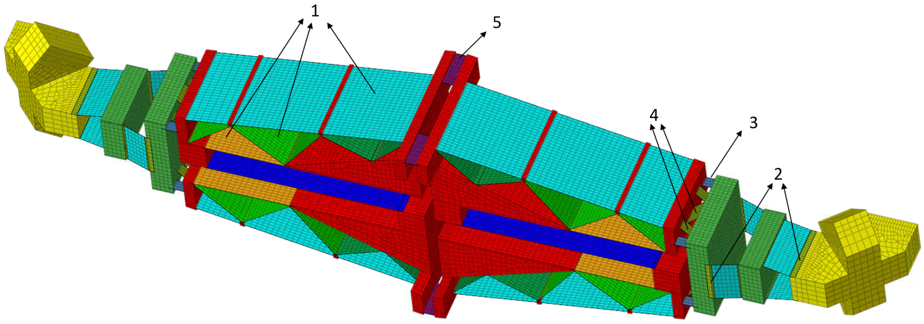

Figure 3.9. Finite element model of truss supported inertial amplification mechanism with parameterized shell element thicknesses.

Table 3.3. Boundaries of the thickness values of parameterized components.

Parameter	**Lower Boundary**	**Nominal**	**Upper Boundary**
Parameter-1	0.5000	0.5000	1.0000
Parameter-2	0.1500	0.1600	0.2500
Parameter-3	0.1000	0.1300	0.2000
Parameter-4	0.1000	0.1000	0.2000
Parameter-5	0.1000	0.1300	0.2000

For optimization, global response search method (GRSM) is utilized. This method calculates a number of iterations initially for creating a rough surface map globally. Then using the data obtained from the random initial iterations, algorithm tries to reach the optimum value starting from the possible optimum points in the surface.

In this case, first 60 iterations are run with random values of parameters between their lower and upper bounds. After that 40 more iterations are run to reach the optimum values.

Table 3.4. Optimization study iterations.

It.	Pr-1	Pr-2	Pr-3	Pr-4	Pr-5	12th Mode	13th Mode	Ratio
1	0.5	0.16	0.13	0.1	0.13	38.363	485.606	12.658
2	0.904	0.248	0.187	0.198	0.145	61.056	582.147	9.535
3	0.965	0.159	0.109	0.166	0.176	41.744	446.673	10.700
4	0.517	0.248	0.182	0.125	0.103	61.867	551.604	8.916
5	0.554	0.234	0.1	0.143	0.192	58.936	543.775	9.227
6	0.51	0.168	0.175	0.192	0.167	45.476	528.558	11.623
7	0.863	0.224	0.102	0.123	0.112	50.672	534.522	10.549
8	0.999	0.202	0.187	0.108	0.189	49.444	556.799	11.261
9	0.925	0.153	0.199	0.141	0.102	34.199	416.683	12.184
10	0.689	0.234	0.135	0.195	0.11	55.701	555.614	9.975
11	0.526	0.24	0.193	0.192	0.185	63.747	569.381	8.932
12	0.991	0.249	0.101	0.158	0.179	61.499	557.08	9.058
13	0.591	0.237	0.195	0.11	0.187	62.209	572.196	9.198
14	0.995	0.234	0.182	0.108	0.101	53.092	559.698	10.542
15	0.956	0.175	0.186	0.174	0.164	44.553	509.947	11.446
16	0.653	0.165	0.192	0.128	0.197	46.195	501.072	10.847
17	0.618	0.174	0.101	0.194	0.135	41.585	515.278	12.391
18	0.658	0.15	0.173	0.178	0.106	36.617	438.22	11.968
19	0.799	0.214	0.138	0.113	0.166	51.374	557.793	10.858
20	0.672	0.158	0.102	0.136	0.171	40.45	465.667	11.512
21	0.968	0.158	0.15	0.108	0.141	37.236	440.258	11.824
22	0.525	0.232	0.105	0.117	0.126	56.53	531.817	9.408
23	0.95	0.165	0.141	0.199	0.116	37.664	445.998	11.842
24	0.523	0.189	0.164	0.142	0.121	45.433	541.202	11.912
25	0.855	0.21	0.142	0.189	0.197	53.678	567.631	10.575
26	0.96	0.235	0.103	0.199	0.134	54.224	546.528	10.079
27	0.989	0.215	0.149	0.158	0.111	51.306	559.841	10.912

Table 3.4 Optimization study iterations. (cont.)

It.	**Pr-1**	**Pr-2**	**Pr-3**	**Pr-4**	**Pr-5**	**12th Mode**	**13th Mode**	**Ratio**
28	0.729	0.219	0.195	0.154	0.149	54.828	574.324	10.475
29	0.533	0.176	0.102	0.192	0.194	48.769	535.24	10.975
30	0.73	0.166	0.108	0.146	0.111	38.428	495.87	12.904
31	0.691	0.238	0.149	0.153	0.189	61.949	574.341	9.271
32	0.748	0.212	0.104	0.163	0.148	51.567	546.248	10.593
33	0.768	0.183	0.195	0.104	0.153	43.147	520.641	12.067
34	0.941	0.247	0.198	0.107	0.152	60.724	579.266	9.539
35	0.997	0.174	0.139	0.125	0.187	43.2	471.173	10.907
36	0.846	0.193	0.199	0.197	0.108	44.906	556.874	12.401
37	0.55	0.158	0.139	0.168	0.142	40.432	482.633	11.937
38	0.511	0.229	0.181	0.175	0.108	57.404	555.536	9.678
39	0.759	0.16	0.147	0.196	0.171	41.98	464.353	11.061
40	0.505	0.219	0.136	0.1	0.198	58.007	551.65	9.510
41	0.733	0.162	0.166	0.129	0.101	36.523	465.619	12.749
42	0.53	0.192	0.153	0.142	0.176	48.745	545.98	11.201
43	0.515	0.189	0.197	0.1	0.135	46.714	551.018	11.796
44	0.683	0.215	0.133	0.145	0.112	52.032	546.639	10.506
45	0.515	0.236	0.111	0.192	0.149	61.027	546.946	8.962
46	0.824	0.249	0.161	0.139	0.132	60.347	565.583	9.372
47	0.761	0.194	0.199	0.196	0.19	49.992	560.856	11.219
48	0.722	0.166	0.141	0.104	0.156	41.798	498.808	11.934
49	0.538	0.236	0.15	0.117	0.152	60.431	552.494	9.143
50	0.964	0.217	0.2	0.191	0.181	54.633	581.31	10.640
51	0.972	0.192	0.134	0.108	0.1	42.028	522.158	12.424
52	0.901	0.232	0.101	0.107	0.186	56.914	546.424	9.601
53	0.805	0.178	0.101	0.197	0.193	47.289	528.067	11.167
54	0.993	0.245	0.16	0.142	0.195	59.175	570.458	9.640

Table 3.4 Optimization study iterations. (cont.)

It.	Pr-1	Pr-2	Pr-3	Pr-4	Pr-5	12th Mode	13th Mode	Ratio
55	0.714	0.16	0.169	0.145	0.16	40.171	467.527	11.638
56	0.767	0.197	0.156	0.196	0.121	47.473	560.851	11.814
57	0.996	0.187	0.2	0.117	0.13	43.613	528.615	12.121
58	0.725	0.248	0.106	0.195	0.199	64.91	563.841	8.687
59	0.541	0.165	0.129	0.101	0.188	45.453	520.079	11.442
60	0.982	0.249	0.134	0.116	0.15	59.5	557.951	9.377
61	0.681	0.156	0.1	0.136	0.101	35.833	463.536	12.936
62	0.659	0.15	0.1	0.117	0.1	33.731	431.078	12.780
63	0.561	0.153	0.105	0.119	0.126	35.695	440.993	12.354
64	0.915	0.157	0.105	0.115	0.124	36.085	446.93	12.385
65	0.729	0.16	0.1	0.126	0.1	35.833	463.536	12.936
66	0.755	0.158	0.1	0.153	0.1	37.277	461.464	12.379
67	0.711	0.172	0.111	0.114	0.111	38.428	495.87	12.904
68	0.792	0.223	0.191	0.147	0.195	56.353	576.354	10.228
69	0.632	0.165	0.1	0.126	0.1	36.205	473.164	13.069
70	0.698	0.162	0.118	0.125	0.102	35.982	464.219	12.901
71	0.659	0.163	0.106	0.126	0.106	36.34	464.48	12.782
72	0.757	0.232	0.199	0.113	0.121	55	568.913	10.344
73	0.676	0.165	0.1	0.116	0.1	35.833	463.536	12.936
74	0.5	0.16	0.1	0.1	0.1	36.572	483.174	13.212
75	0.685	0.162	0.103	0.119	0.103	35.833	463.536	12.936
76	0.91	0.156	0.18	0.115	0.184	41.248	450.009	10.910
77	0.5	0.166	0.11	0.1	0.1	38.943	515.596	13.240
78	0.5	0.161	0.1	0.135	0.1	36.572	483.174	13.212
79	0.507	0.165	0.108	0.101	0.101	38.943	515.596	13.240
80	0.94	0.183	0.14	0.166	0.147	43.805	518.186	11.829
81	0.5	0.161	0.119	0.1	0.1	36.723	483.876	13.176

Table 3.4 Optimization study iterations. (cont.)

It.	**Pr-1**	**Pr-2**	**Pr-3**	**Pr-4**	**Pr-5**	**12th Mode**	**13th Mode**	**Ratio**
82	0.5	0.162	0.108	0.106	0.1	36.644	483.54	13.196
83	0.504	0.161	0.119	0.101	0.101	36.723	483.876	13.176
84	0.797	0.177	0.134	0.155	0.189	47.456	528.88	11.145
85	0.5	0.162	0.1	0.107	0.1	36.572	483.174	13.212
86	0.518	0.165	0.107	0.1	0.1	38.943	515.596	13.240
87	0.502	0.162	0.1	0.106	0.1	36.572	483.174	13.212
88	0.995	0.215	0.154	0.2	0.158	50.589	565.301	11.174
89	0.5	0.163	0.103	0.1	0.1	36.572	483.174	13.212
90	0.504	0.165	0.107	0.1	0.101	36.644	483.54	13.196
91	0.501	0.163	0.103	0.1	0.1	36.572	483.174	13.212
92	0.52	0.205	0.146	0.192	0.195	53.003	554.466	10.461
93	0.525	0.168	0.116	0.1	0.1	39.001	516.083	13.233
94	0.522	0.168	0.112	0.103	0.1	38.943	515.596	13.24
95	0.526	0.168	0.116	0.1	0.1	39.001	516.083	13.233
96	0.51	0.187	0.172	0.1	0.195	50.623	551.796	10.900
97	0.525	0.167	0.116	0.1	0.1	39.001	516.083	13.233
98	0.516	0.165	0.11	0.102	0.1	38.943	515.596	13.240
99	0.504	0.178	0.124	0.107	0.111	42.043	527.544	12.548
100	0.911	0.195	0.105	0.132	0.154	44.351	535.27	12.069

When Table 3.4 is examined, it is deduced that the most effective parameter is parameter-5, thickness of the short flexure, and the least effective parameter is parameter-1, thickness of the truss members. It can be seen that, 77th, 79th, 86th, 94th and 98th iterations are the best choices for thickness values. Additionally, the values between these iterations are very close to each other so as the optimum value, 98th iteration is accepted.

A separate optimization is planned to be run for the shell components inside the bulk parts of Figure 3.6 and their thicknesses will be decided accordingly in production phase. Until then, their thicknesses are assumed identical and after a short optimization study, the value is decided to be 0.52 mm. Consequently, 12th and 13th natural frequencies are obtained at 37.28 Hz and 502.07 Hz, and the ratio of 13th natural frequency to the 12th natural frequency becomes 13.46.

4. DESIGN SCALING FOR MANUFACTURING

The mechanism in Figure 3.6 is 157 mm in length and it contains features with thickness as low as 0.1 mm (see Table 3.3 Parameter-3, 4, 5). To avoid possible errors during manufacture and assembly processes the mechanism is enlarged by a scale. For the scale, commercially available truss structures are investigated and the system is scaled to fit in a truss structure (see Figure 4.1) with 600 mm members. This decision is taken in accordance with available manufacturing precision, quality and sizes of connection members like nodal spheres, bolts and screws, additionally total mass of the structure and cost is taken into account. The mechanism is scaled up 3.8 times so that it is possible to remove the bars of a truss structure and insert inertial amplification systems into the structure.

Figure 4.1. A generic truss structure.

Natural frequencies determining the band gap were between 12th and 13th mode as 37.28 and 502.07 Hz for an octahedron made up of mechanisms with 157 mm length. When the mechanism is scaled up to 600 mm 12th and 13th natural frequencies becomes 9.78 and 131.60 Hz. For both cases ratio of the upper and lower limits of the band gap is 13.46. It is shown that even though the natural frequencies change with changing size, ratio of these two gap limits remain constant.

The mechanism is modeled to be produced by common manufacturing methods as shown in Figure 4.2. From the scaled up FEM model, mass of an octahedron structure is calculated to be approximately 110 kg. After prototype dimensions are determined an additional series of analysis tasks are accomplished.

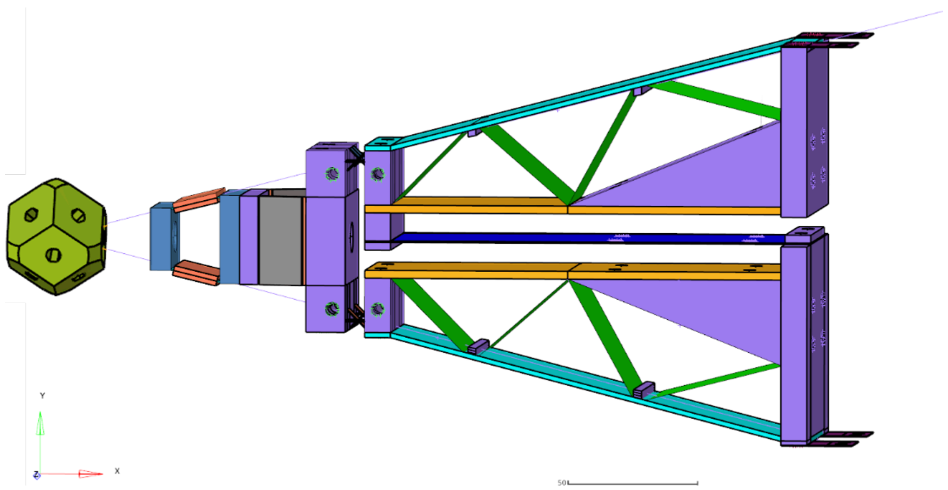

Figure 4.2. 3D model of half inertial amplification mechanism scaled up 3.8 times. The other half is vertical and horizontal reflection of the half mechanism.

The system is composed of 3D modeling for prototype manufacturing is completed as shown in figure 4.2. FEM model of octahedron is built to conduct dynamic assessment of the structure (see Figure 4.3).

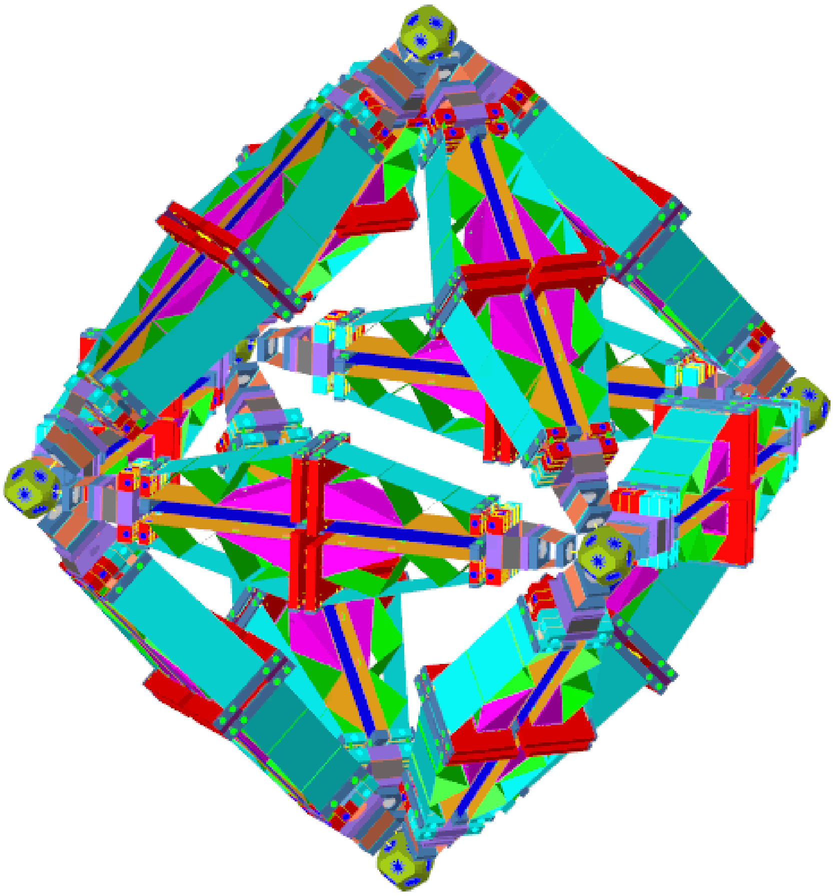

Figure 4.3. FEM model of production model of the octahedron structure.

Some features are modified to obtain an appropriate connection interface with the rest of the mechanism as shown in Figures 4.4 and 4.5.

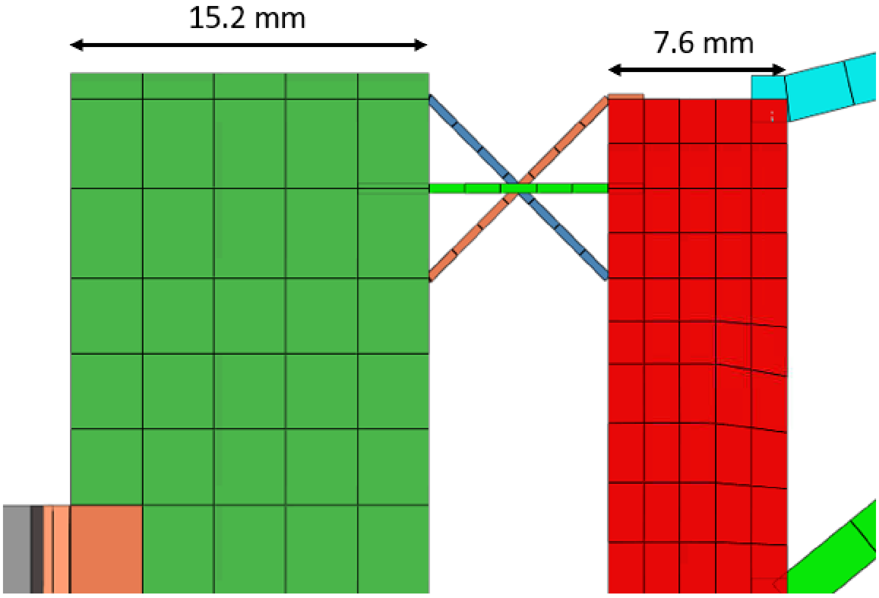

Figure 4.4. Former dimensions of cross flexure ends.

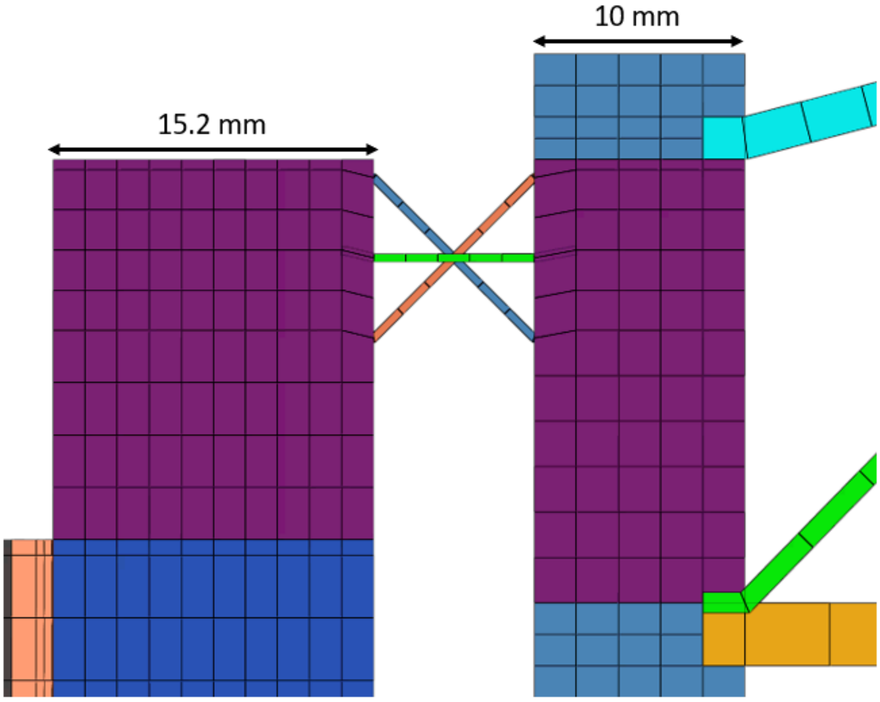

Figure 4.5. New dimensions of cross flexure ends.

Similarly, parts at the ends of the short flexures are modified from 7.6 mm thickness to 10 mm thickness so that a M5 countersunk bolts can be used on it. These modifications changed the inertia distribution of the mechanism. Additionally, remote center of rotation mechanisms are decided to be produced separately for each stage and bolted to each other with a single bolt. For a better mounting, plate dimensions of remote center of rotation mechanisms are also updated without changing the dimensions of the other parts. After modeling the mechanism in 3D, an FEM model is set up using the updated geometry.

Using the FEM model, natural frequencies and mode shapes are calculated as shown in Table 4.1. Band gap is still observed between 12th and 13th natural frequencies but the ratio became 10.36. As expected, the motion displayed in 12th mode is opening and closing motion (see Figure 4.6) and the motion in 13th mode is torsion of individual mechanisms around the corners (see Figure 4.7).

Table 4.1. FEM model of production model of the octahedron structure.

Mode No	**Frequency**
1	5.19
2	6.26
3	6.27
4	6.27
5	6.75
6	6.75
7	6.75
8	8.78
9	8.78
10	8.78
11	9.18
12	9.19
13	95.20
14	95.24
15	102.85

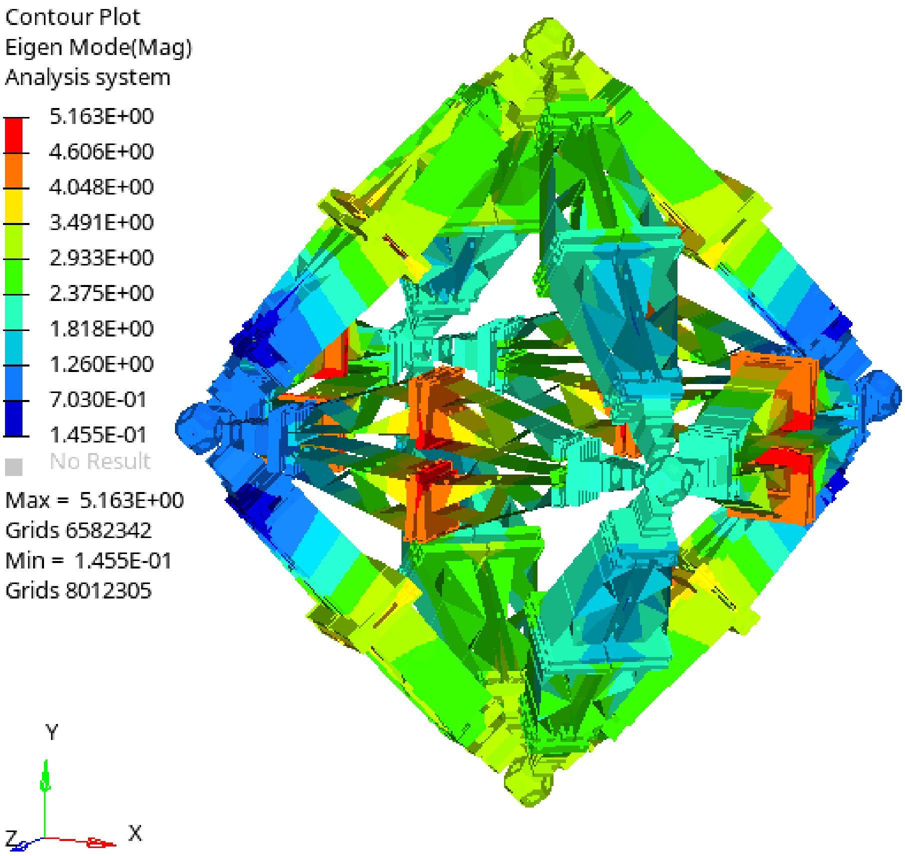

Figure 4.6. 12th mode shape of production model.

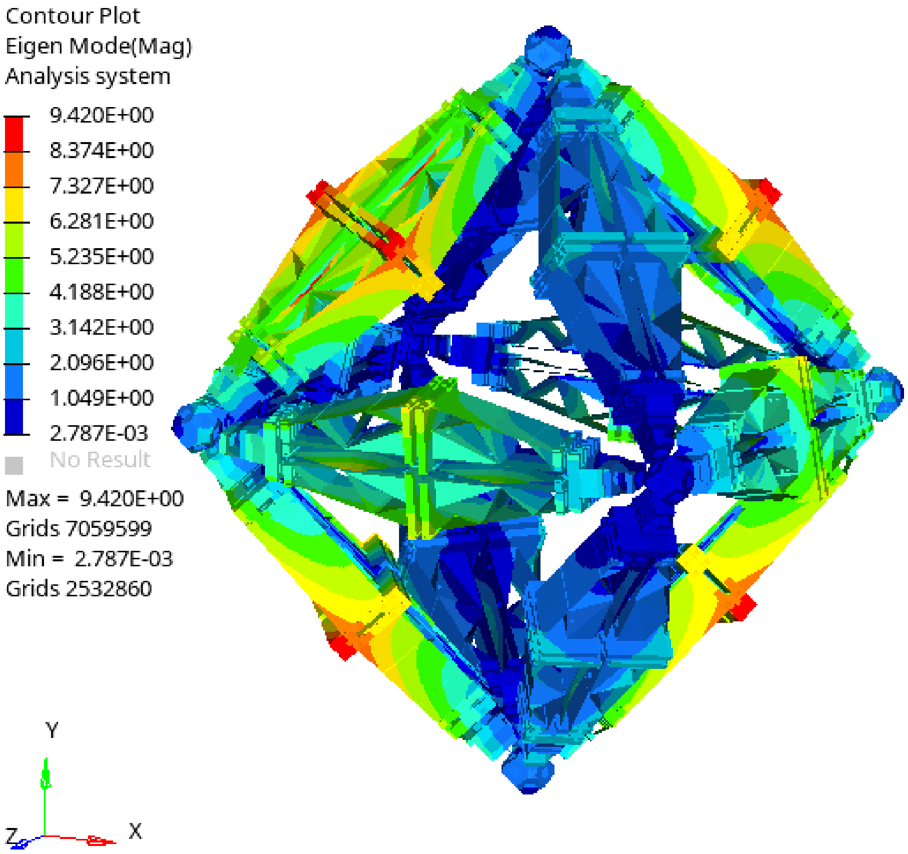

Figure 4.7. 13th mode shape of production model.

To improve the production model, one last optimization study is conducted. Changes made on the production model can be stated as:

- In the new model, it is found out that the out-of-plane motion is not as effective as before, so the features indicated by number 5 in Figure 3.9 are removed. Short flexures are shifted inside as in Figure 4.8.
- Width of the short flexures indicated by number 5 are brought to 10 mm.
- Material removal are conducted from the component number 6 of Figure 4.8 so that the rotational inertia around the x-axis is decreased. As a result, increase in the frequency ratio is achieved.
- Thicknesses of the components 1.1, 1.2, and 1.3 are optimized using global response surface method and their thicknesses are decided to be 2 mm for component 1.1, 1 mm for component 1.2 and 3 mm for component 1.3.
- For the rest of the component thicknesses (components 2.1, 2.2, 3, 4, 5) are

separately optimized by the same method.

- An additional plate of 8.5 mm thickness (component 7, Figure 4.8) is added to the gap between the lower triangle and the long flexure to increase the inertia of the system.

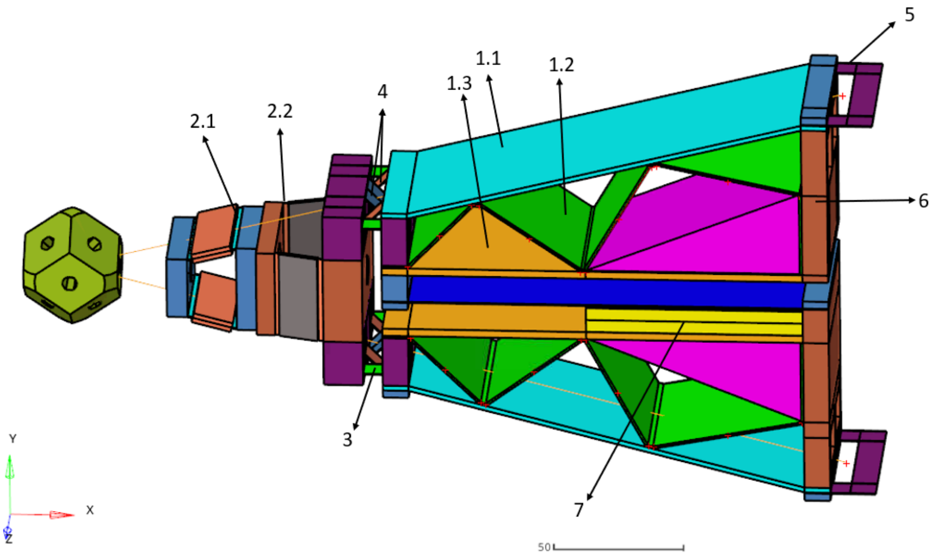

Figure 4.8. Optimized production model of the inertial amplification mechanism.

Using the 3D model in Figure 4.8, FEM model of an octahedron is set up (see Figure 4.9), parametric optimizations are conducted on that model and using the results 3D model is updated.

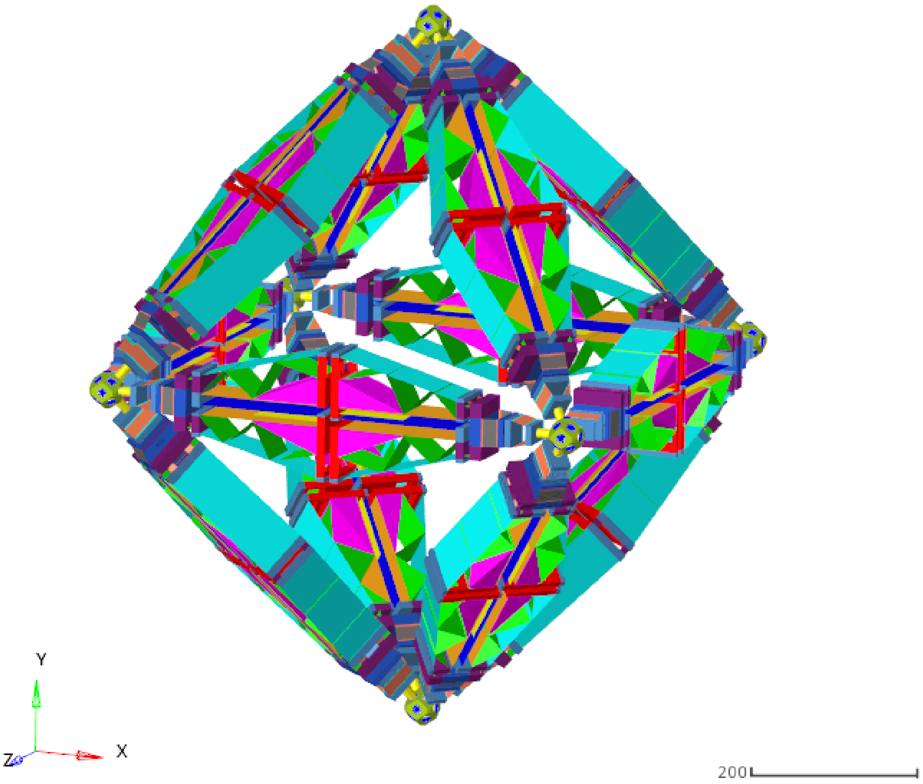

Figure 4.9. FEM model of an octahedron made up of production model of inertial amplification mechanisms.

Table 4.2. Thickness values obtained after optimization study on production model.

Parameter	**Lower Boundary (mm)**	**Upper Boundary (mm)**	**Optimum thickness (mm)**
1.1	1.00	5.00	2.00
1.2	1.00	5.00	1.00
1.3	1.00	5.00	3.00
2.1	0.40	1.00	0.44
2.2	0.40	1.00	0.48
3	0.40	1.00	0.40
4	0.40	1.00	0.40
5	0.40	1.00	0.40

Natural frequencies of the octahedron with optimized parameters are calculated as in Table 4.3. According to the table, new band gap ratio is 14.43. This ratio is larger than any other three dimensional phononic crystal or elastic metamaterial in the literature (Table 1.1). Band gap is still located between 12th and 13th natural frequencies, and beam modes of the long flexures start at 102.27 Hz which is well above the band gap frequency. 12th and 13th mode shapes are similar to former iterations as shown in Figures 4.10 and 4.11.

Table 4.3. Natural frequencies of octahedron structure with optimized parameters.

Mode No	**Frequency**	**Mode No**	**Frequency**
1	3.18	26	90.00
2	3.98	27	90.02
3	3.98	28	90.03
4	3.98	29	90.03
5	4.37	30	90.05
6	4.37	31	90.05
7	4.37	32	90.07
8	6.05	33	90.07
9	6.05	34	90.11
10	6.08	35	90.12
11	6.09	36	90.16
12	6.09	37	90.19
13	87.31	38	90.2
14	87.33	39	90.21
15	87.36	40	94.63
16	89.83	41	94.72
17	89.84	42	102.27
18	89.93	43	102.36
19	89.94	44	102.4
20	89.96	45	109.61
21	89.97	46	109.65
22	89.97	47	109.81
23	89.99	48	113.62
24	90.00	49	113.67
25	90.00	50	113.81

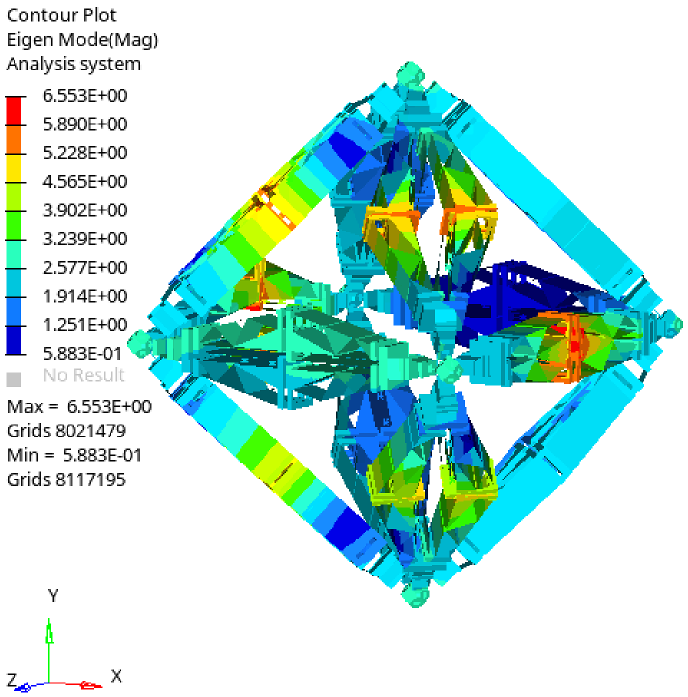

Figure 4.10. 12th mode shape of optimized octahedron at 6.09 Hz.

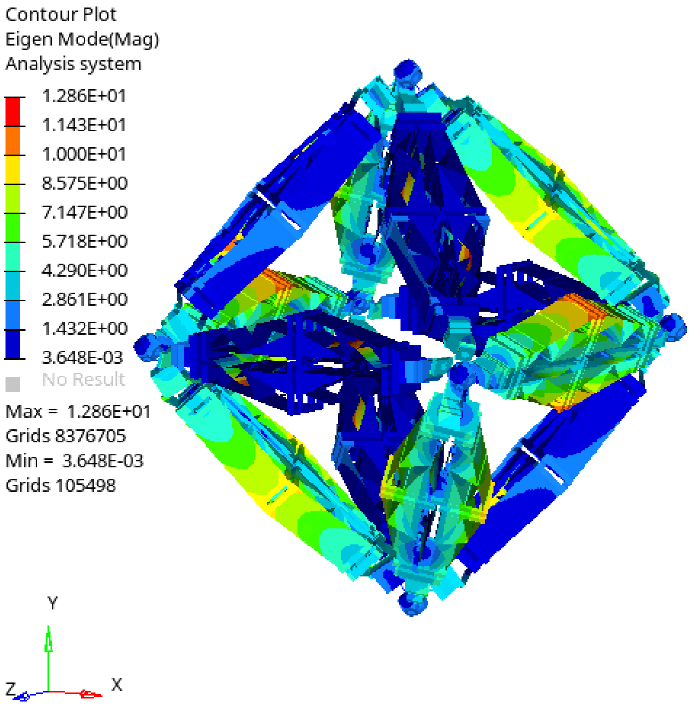

Figure 4.11. 13th mode shape of optimized octahedron at 87.31 Hz.

After verifying the effect of optimization by modal analysis, FRF analysis is conducted by applying unit displacement from one corner and measuring data from the opposite corner. For FRF analysis, 1% material damping is applied to the structure. Frequencies at which displacement is calculated lower than 1 mm are within the isolation frequency range. As shown in Figure 4.12 vibration isolation occurs between 5.25 Hz and 100.75 Hz. The lower limit of the isolation bandwidth is approximately at the 12th natural frequency while the upper limit is well above the 13th natural frequency. Because the 13th mode shape is the torsional motion of the mechanisms, the corner at which measurement is taken displays no considerable displacement at that frequency.

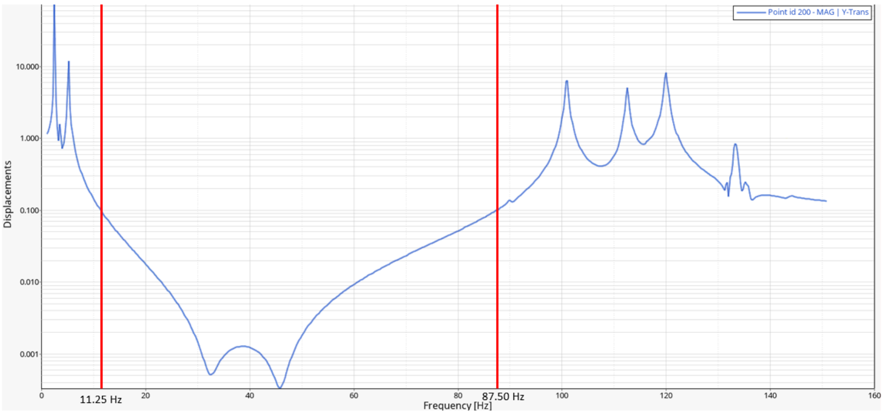

Figure 4.12. Axial displacement result of FRF analysis of optimized octahedron structure.

When the Figure 4.12 is investigated, between 11.25 and 87.50 Hz vibration transmission drops down below 0.1 times of input displacement. In other words, 90% of the vibration is isolated.

FRF analysis is calculated according to linear system assumptions and steady state condition. The mechanism is also analysed under transient conditions to observe it’s linear behavior under low displacement and nonlinear behavior under high displacement. Firstly an FRF analysis is run on a single mechanism by exciting from one corner by unit displacement and measuring from the other to see the dynamic behavior of a single mechanism (see Figure 4.13). Inside the band gap, the tip displacement is measured as 0.8 mm throughout the frequency range for 1 mm input vibration. Hence, the output amplitude is 80% of the input amplitude.

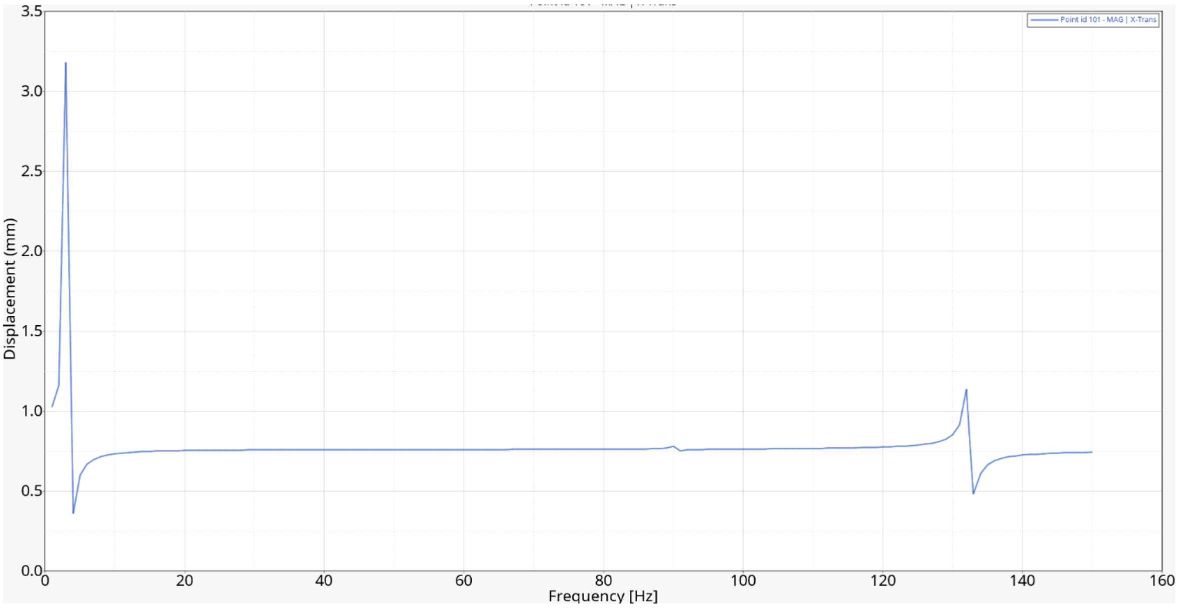

Figure 4.13. Axial displacement result of a single mechanism FRF analysis.

For transient analysis, a single mechanism is excited axially from left corner for 1, 4, and 10 mm displacement magnitudes in time domain with 11.25 Hz and 87.50 Hz for 30 periods and displacement at the opposite corner is calculated as shown in Figure 4.14.

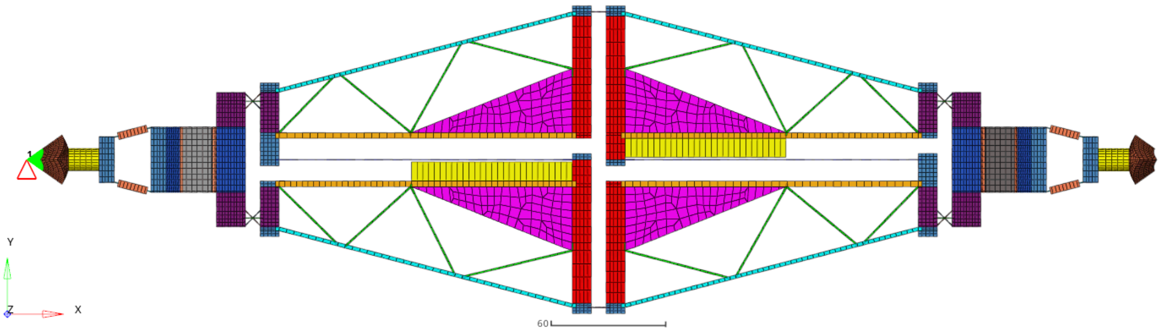

Figure 4.14. Transient analysis model for 1, 4, and 10 mm displacement excitation with 11.25 and 87.50 Hz.

Displacement excitation applied on the left corner at 11.25 and 87.50 Hz are shown in Figures 4.15 and 4.16.

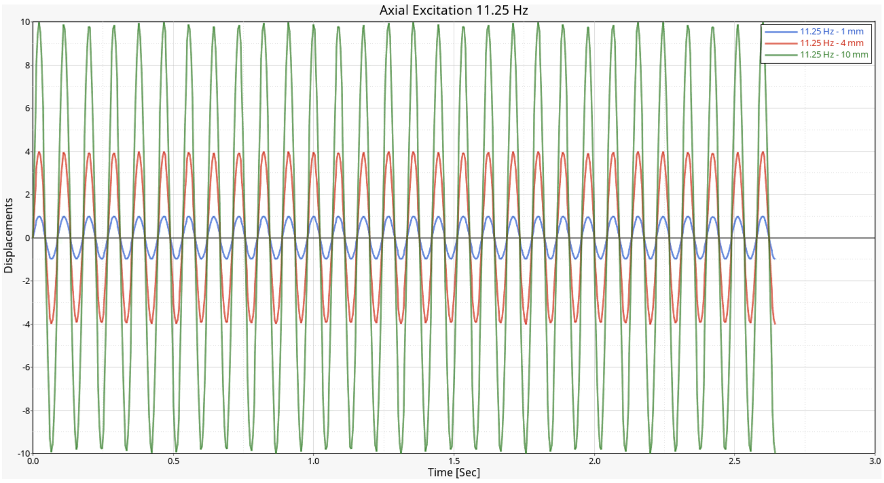

Figure 4.15. Displacement excitation versus time at 11.25 Hz.

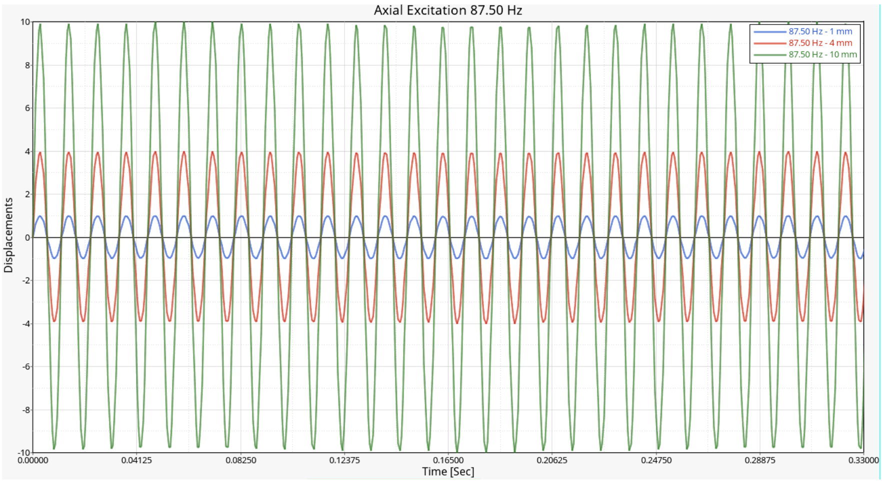

Figure 4.16. Displacement excitation versus time at 87.50 Hz.

Displacement measurements are conducted on the other corner of the mechanism. Results are shown in Figures 4.17 and 4.18. Figure 4.17 shows that the output amplitude is approximately 80% of the input amplitude for 1 mm, 4 mm and 10 mm input amplitudes. However, Figure 4.18 shows that output amplitudes are slightly higher especially for 4 mm and 10 mm input amplitudes.

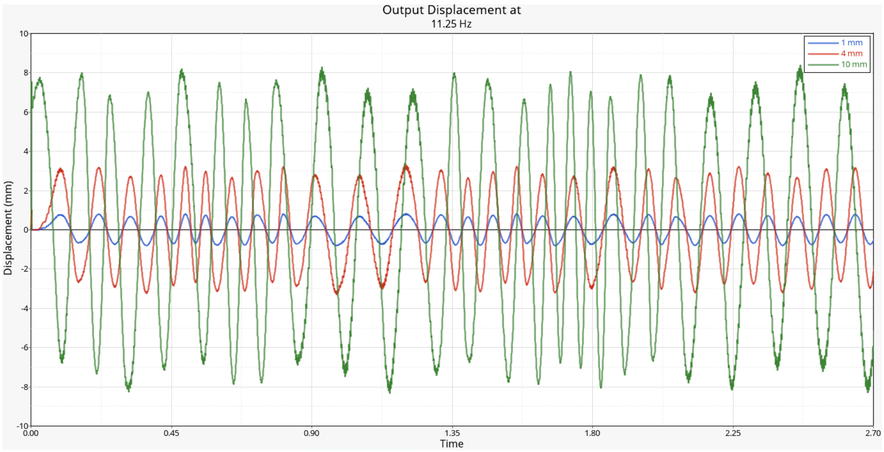

Figure 4.17. Displacement of the opposite corner versus time at 11.25 Hz.

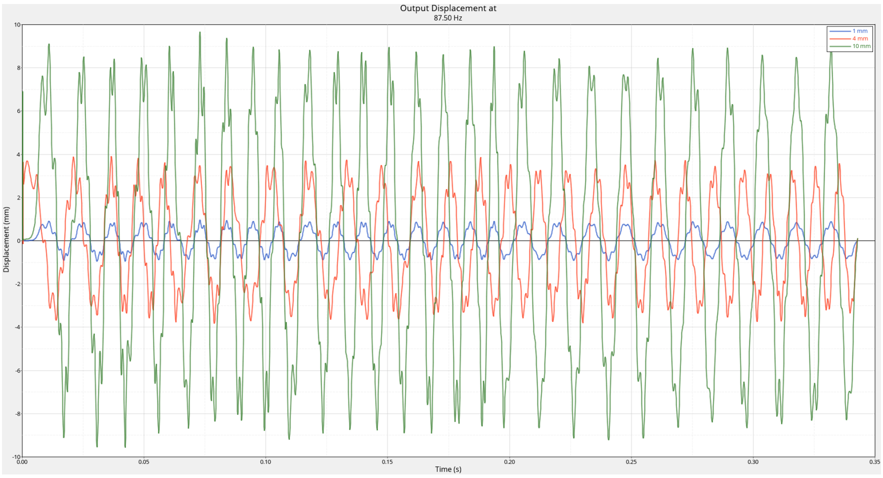

Figure 4.18. Displacement of the opposite corner versus time at 87.50 Hz.

For each case, RMS values of these graphs are calculated as, 0.514 for 1 mm, 2.055 mm for 4 mm and 5.525 mm for 10 mm at 11.25 Hz. At 87.50 Hz 0.533 mm at 1 mm, 2.253 mm at 4 mm and 5.525 mm at 10 mm.

As shown in Table 4.2, parameters 3, 4, and 5 are brought to the lower limit at 0.4 mm. Additionally, parameters 2.1 and 2.2 get quite close to the lower limits. To verify the systems durability against it's own weight (110 kg) a static analysis is run by applying gravitational acceleration load and restricting the motion at the horizontal corners to calculate the displacements (see Figure 4.19) and the maximum stresses in the structure (see Figure 4.20).

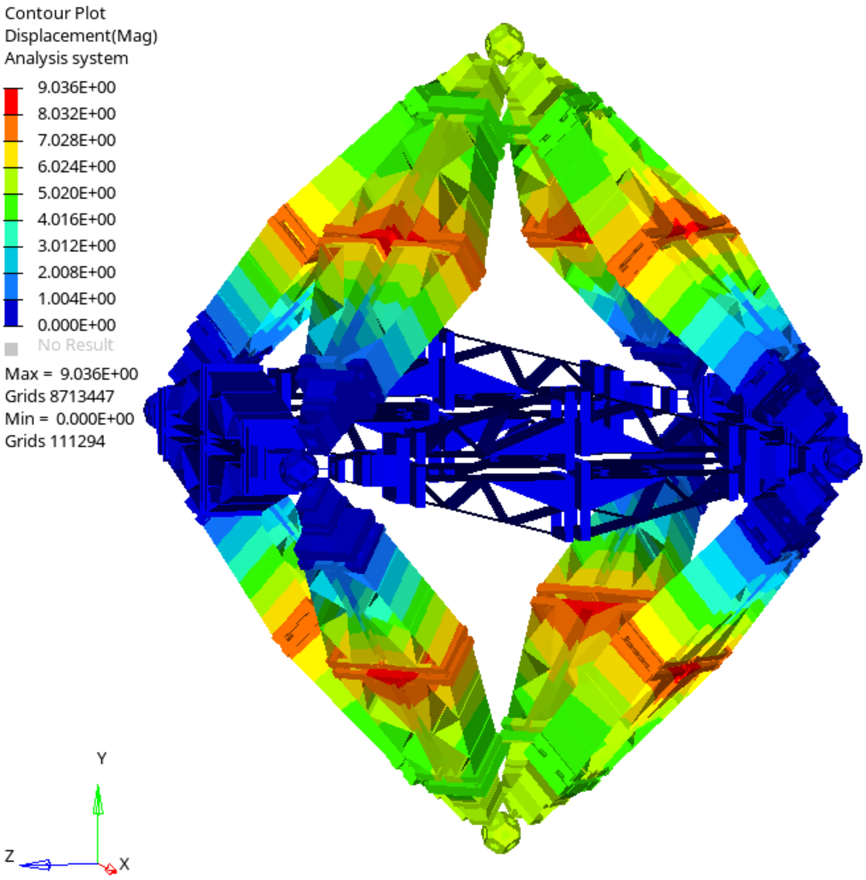

Figure 4.19. Displacement contour of prototype octahedron model under gravitational acceleration.

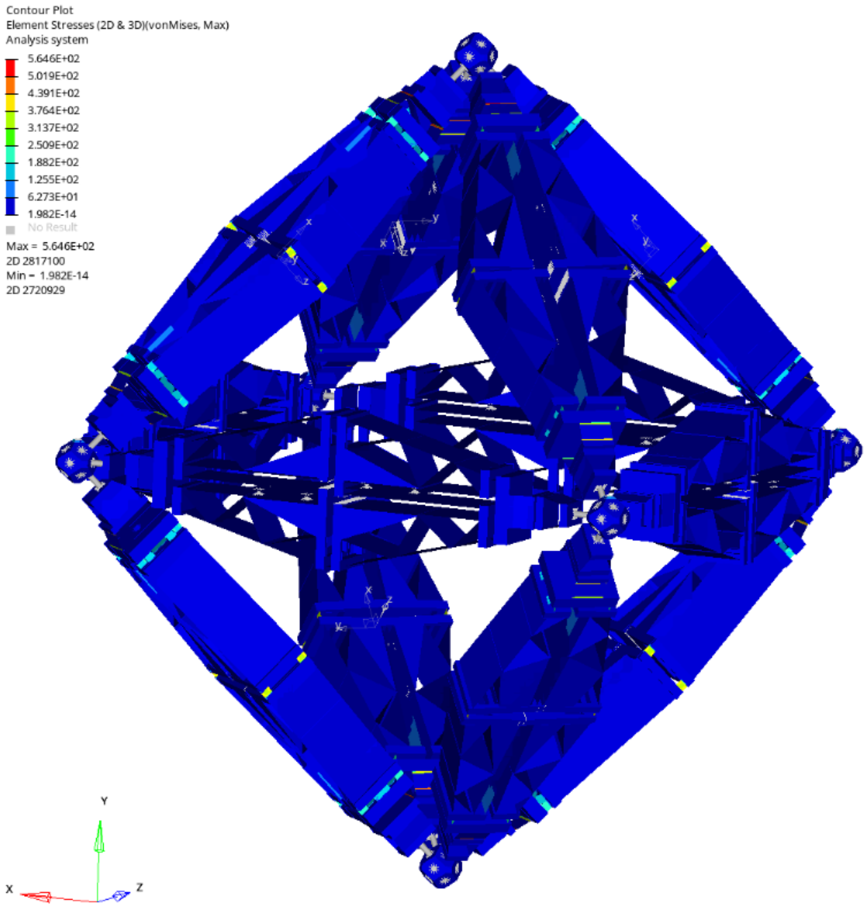

Figure 4.20. Von Mises stress contour plot of prototype octahedron model under gravitational acceleration.

As shown in Figure 4.19, octahedron structure deforms under gravitational acceleration load which causes stresses up to 560 MPa as shown in Figure 4.20. Namely, the mechanisms in the upper pyramid contracts and the lower pyramid extracts when the system is hung from its corners on the horizontal plane. To redeem the deformation of the mechanism under it's own weight, short flexures are prestressed by applying moment (see Figure 4.21) to obtain a straight mechanism when assembled into an octahedron. For correct prestress application, flexures at the top pyramid are assembled such that their neutral position is closed and the opposite is applied to the mechanisms at the lower pyramid.

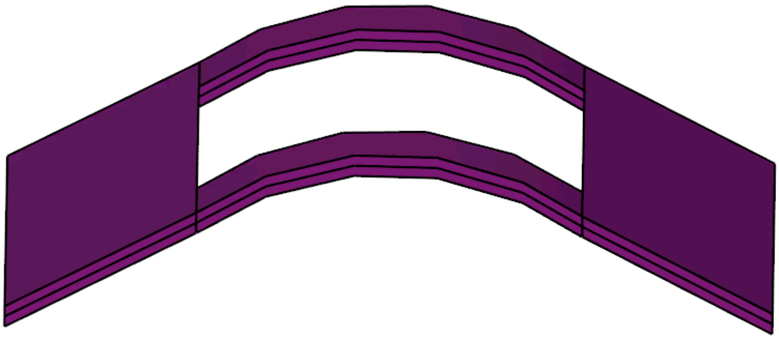

Figure 4.21. Prestressed short flexure component to obtain an appropriate position of mechanism when assembled.

The necessary moment application is calculated by applying 500 N.mm moment in total at each short flexures through 25 steps as shown in Figure 4.22 and calculating displacement after applying gravitational load to the structure.

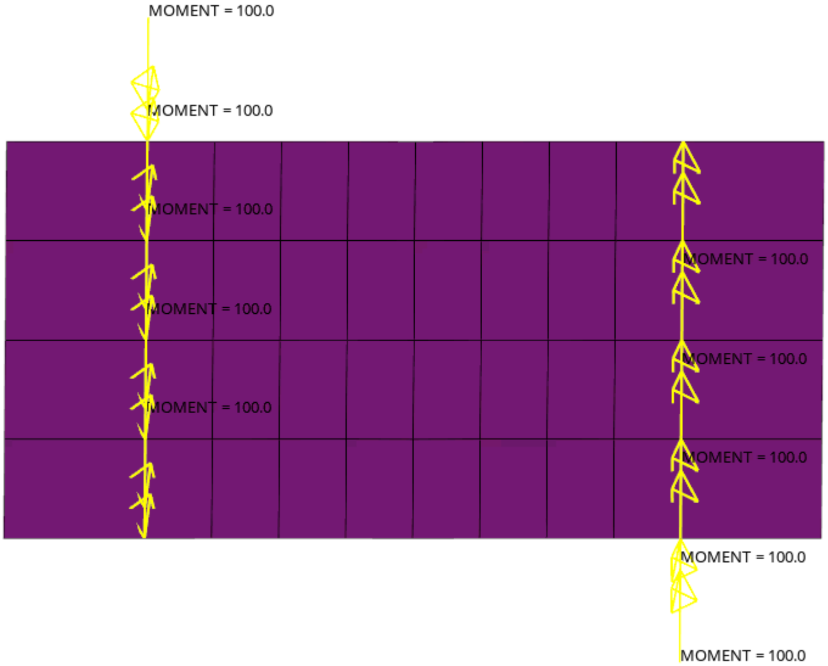

Figure 4.22. Moment load for compensating the deformation caused by gravity.

After applying the moment load to the octahedron structure it is calculated that when 320 N.mm moment is applied, maximum displacement drops down to 0.112 mm from 9.036 mm (see Figure 4.23). As a result, the maximum stress in the structure is reduced to 13.4 MPa from 564.6 MPa (see Figure 4.24).

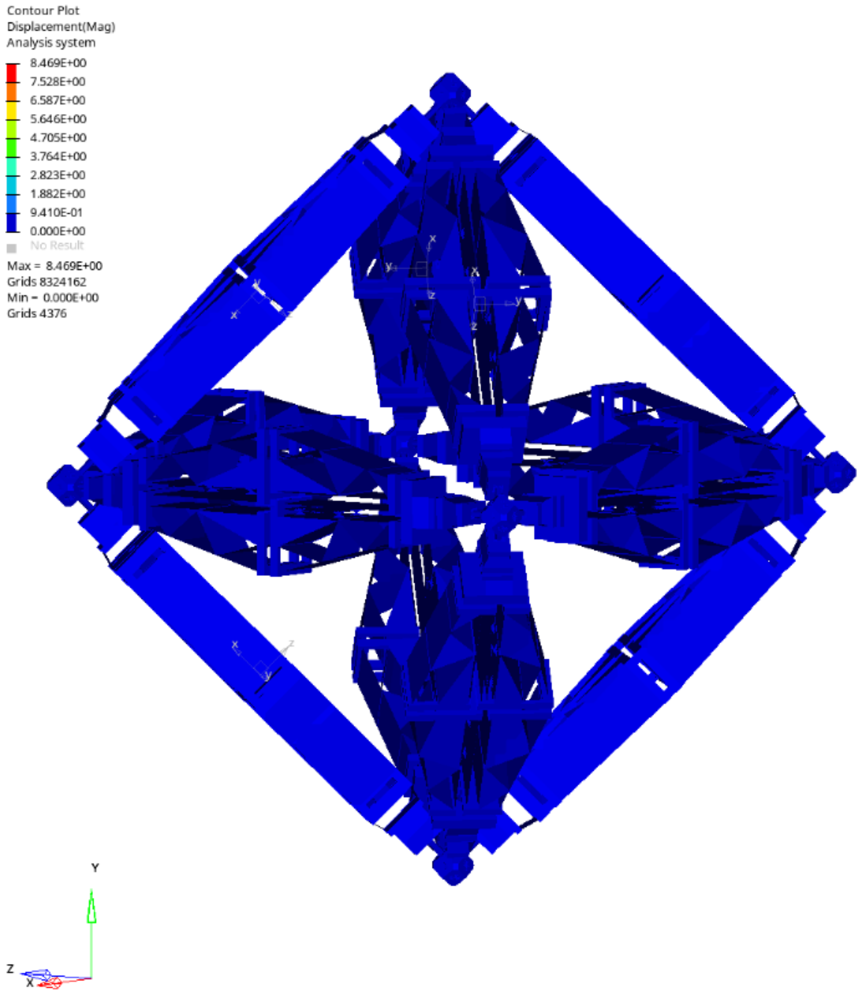

Figure 4.23. Displacement contour plot of static analysis step at which minimum displacement is obtained.

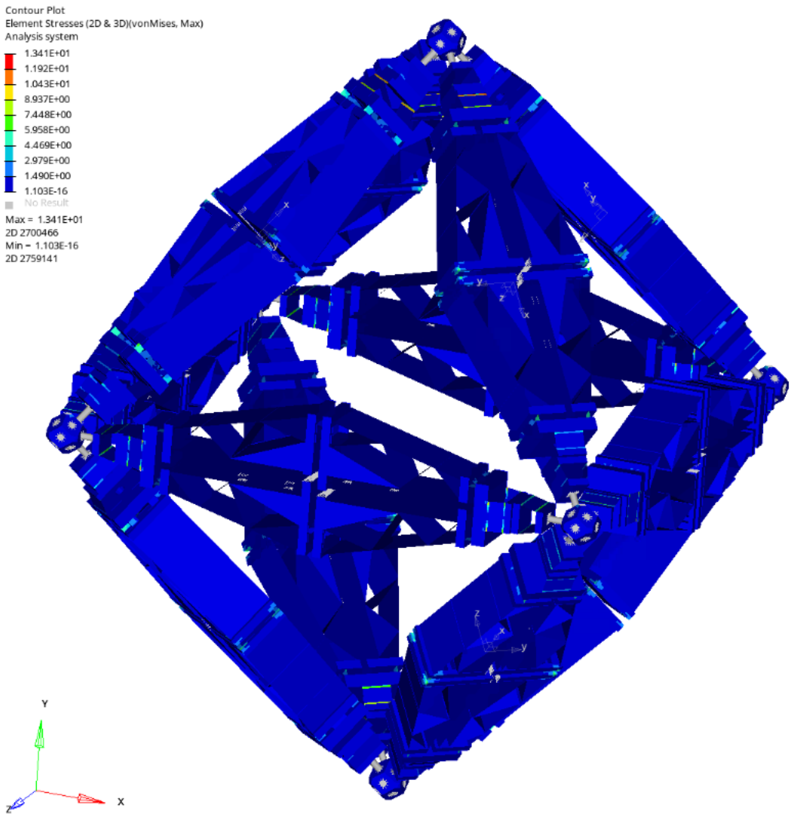

Figure 4.24. Von Mises stress contour plot of static analysis step at which minimum displacement is obtained.

To find out the amount of deformation needed to obtain required moment is calculated by applying required moment to a single short flexure as shown in Figure 4.25. It is found out that a single short flexure is needed to be deformed 0.765 mm at the tip to obtain 320 N.mm moment at the end as shown in Figure 4.26.

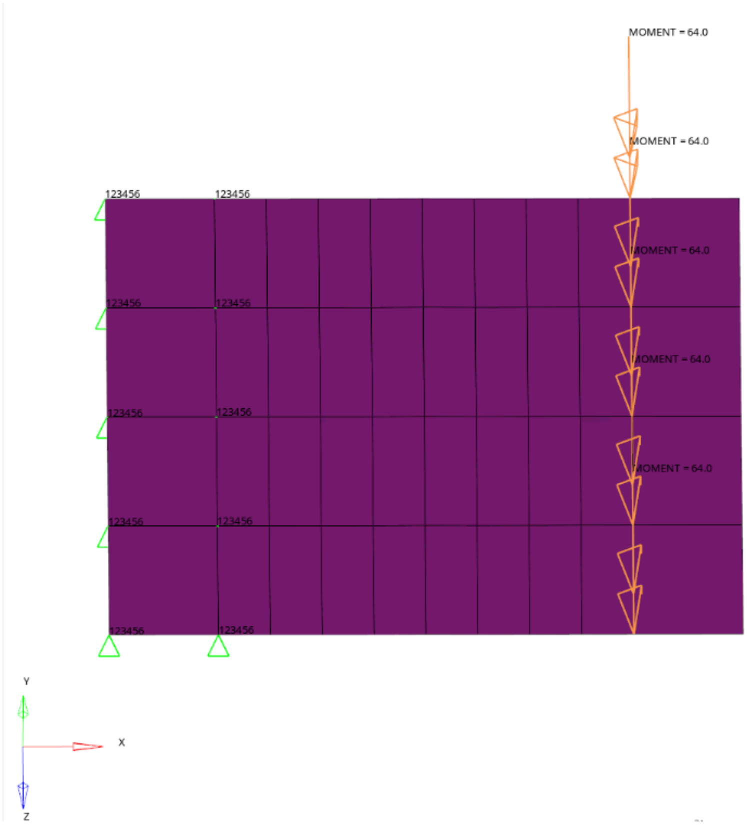

Figure 4.25. Application of moment which will compensate the deformation caused by octahedron weight on a single short flexure.

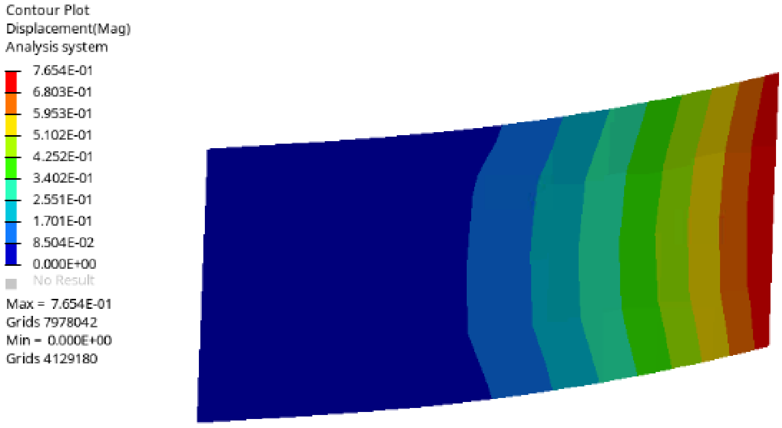

Figure 4.26. Displacement contour plot of single short flexure under loading of moment which will compensate the deformation caused by octahedron weight.

After completion of this analysis, all analytical information for manufacturing the system has been gathered and prototype manufacturing has begun.

5. MANUFACTURING

After completing the necessary calculations on the FEM model, production phase of the octahedron structure commenced. All possible components are produced from sheet metal by laser cutting. However, some components like cross flexures and remote center of rotation mechanisms require much higher precision for having thicknesses down to 0.4 mm. To manufacture these parts, wire EDM method is used because of it's higher precision. Also, the triangular weights are laser cut from 10 mm plate and bolted together.

After manufacturing of all components is finished, components are assembled to obtain 12 inertial amplification mechanisms. Corners of the octahedron are assembled with remote centre of rotation (RCR) mechanisms separately and lastly mechanisms and corners are assembled into an octahedron.

Lastly, the octahedron structure is tested using hammer and shaker as excitation sources. Test results are compared with simulation results and a generic truss structure.

5.1. Prototype Manufacturing

For the triangular weights, steel plate with 10 mm thickness is cut by laser and the first triangle is countersunk while the last one is tapped (see Figure 5.1). Six of them are brought together via two bolts (see Figure 5.2) to obtain a 60 mm wide triangular block which will be used as an inertia at the center of the mechanism (see Figure 5.3). 288 pieces of 10 mm thick triangles are used to obtain 48 blocks as shown in Figure 5.4.

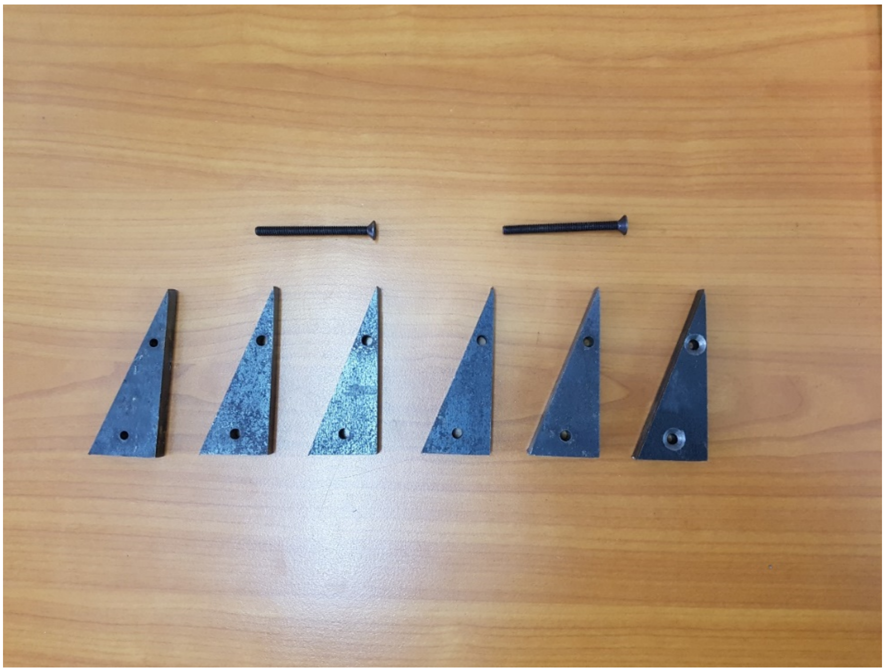

Figure 5.1. Six pieces of 10 mm steel plate cut in triangular shape and the first one is countersunk while the last one is tapped for bolting.

Figure 5.2. Six pieces of 10 mm triangles are brought together.

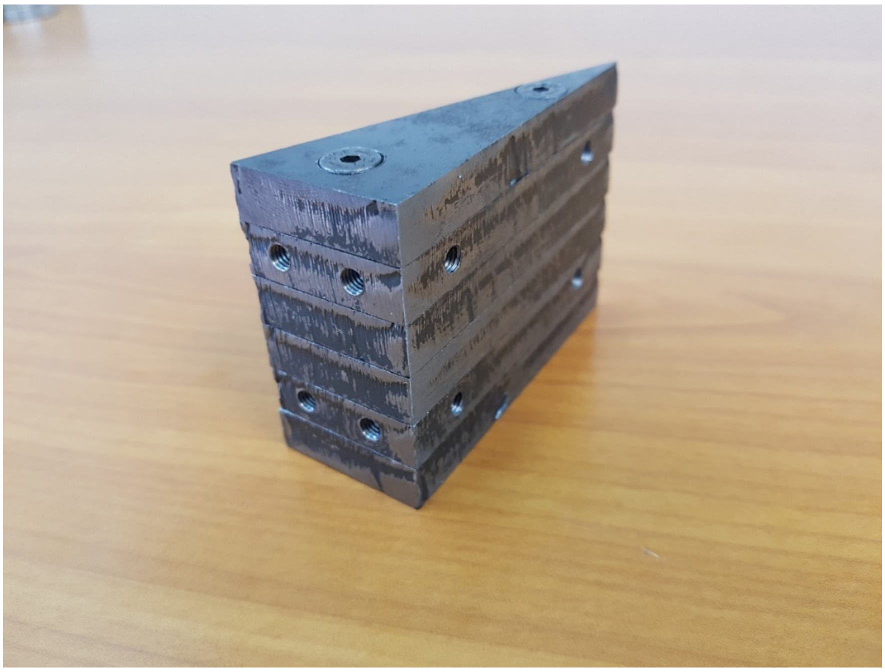

Figure 5.3. Six pieces of 10mm triangles are bolted together. The triangular block is tapped at 8 different points to enable attachment to the wall plate and bottom plate.

Figure 5.4. 48 triangular blocks are manufactured.

The wall plates which triangular blocks are connected as shown in Figure 4.9 number 6 are also cut by laser from 10 mm metal sheet and machined. They are connected to the blocks via four bolts so four holes are countersunk. They are also connected to other sheet metals from top and bottom. These holes are threaded.

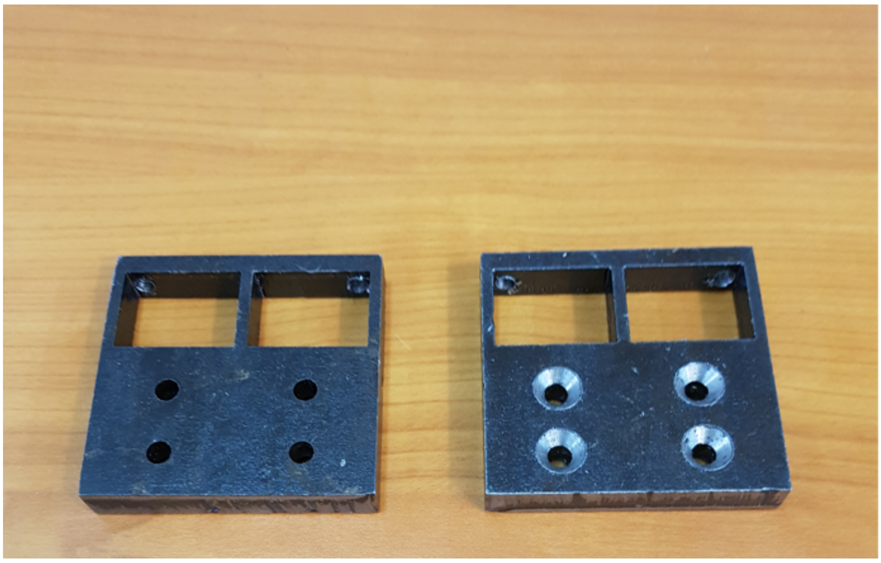

Figure 5.5. Short wall plates before and after countersinking.

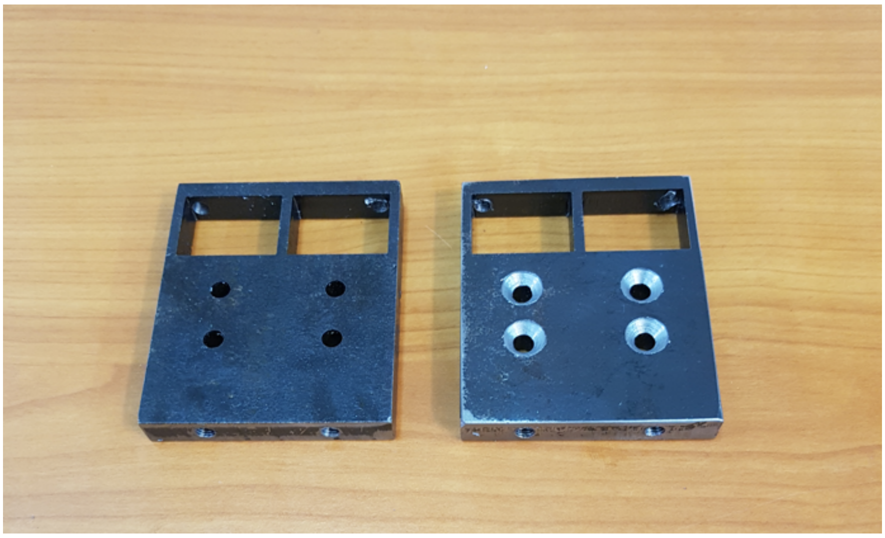

Figure 5.6. Long wall plates before and after countersinking.

24 pieces for both short and long wall plates are produced as shown in Figure 5.7.

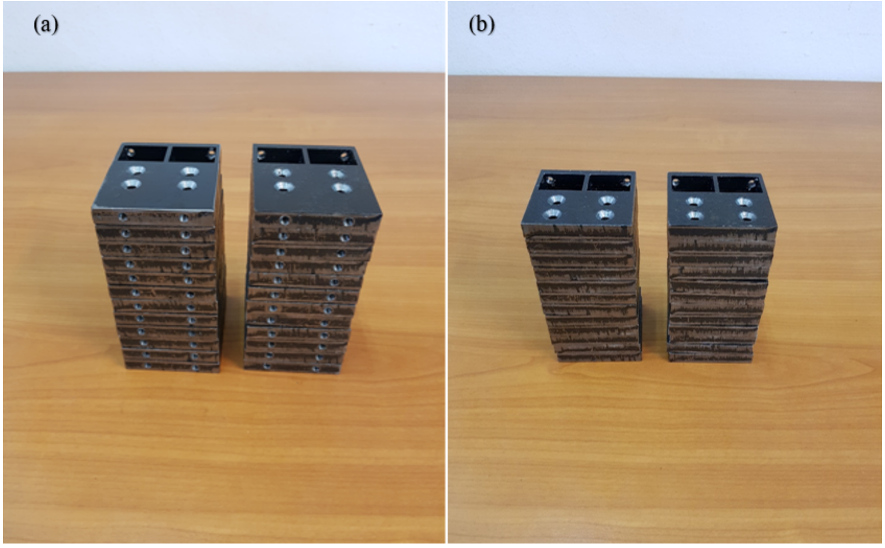

Figure 5.7. 24 pieces of a) short wall, b) long wall.

8.5 mm thick weight blocks are cut from 10 mm sheet metal, too. After laser cutting, they are machined to reduce the thickness. Lastly, they are countersunk to be connected to the mechanism as shown in Figure 5.8.

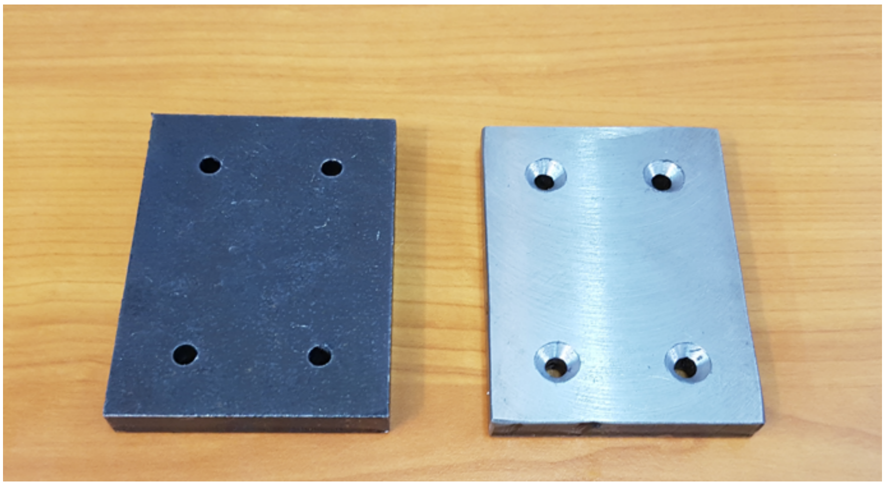

Figure 5.8. 8.5 mm thick blocks for extra mass near the centre.

Each mechanism contains two of these components, so 24 pieces are produced.

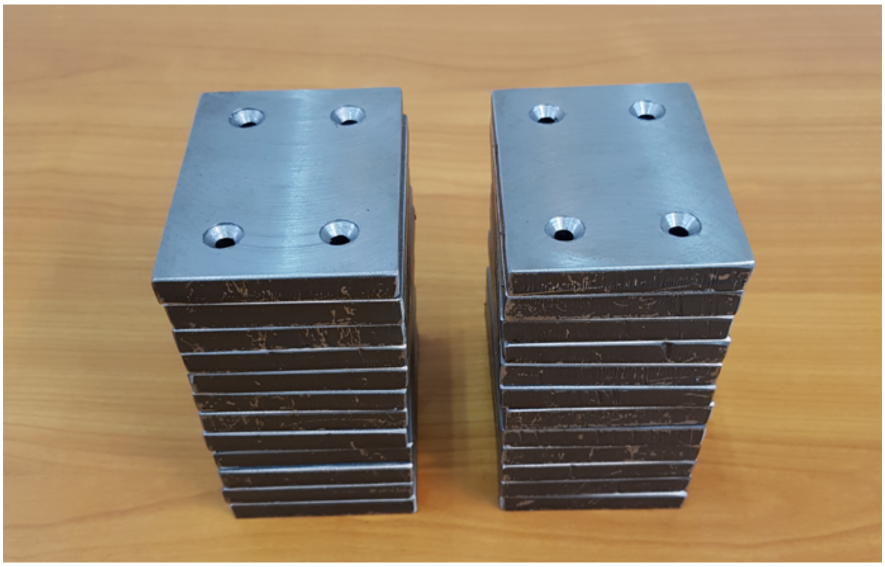

Figure 5.9. 24 pieces of 8.5 mm thick blocks.

3 mm plates shown as number 1.3 in Figure 4.8 are also laser cut from sheet metal. 24 of them are countersunk to be connected to the triangular blocks (see Figure 5.10), and another 24 are prepared to be connected to cross flexures (see Figure 5.11).

Figure 5.10. 3 mm plates countersunk to be connected to triangular blocks.

Figure 5.11. 3 mm plates countersunk to be connected to cross flexures.

In total 24 pieces for both type are produced as shown in Figure 5.12.

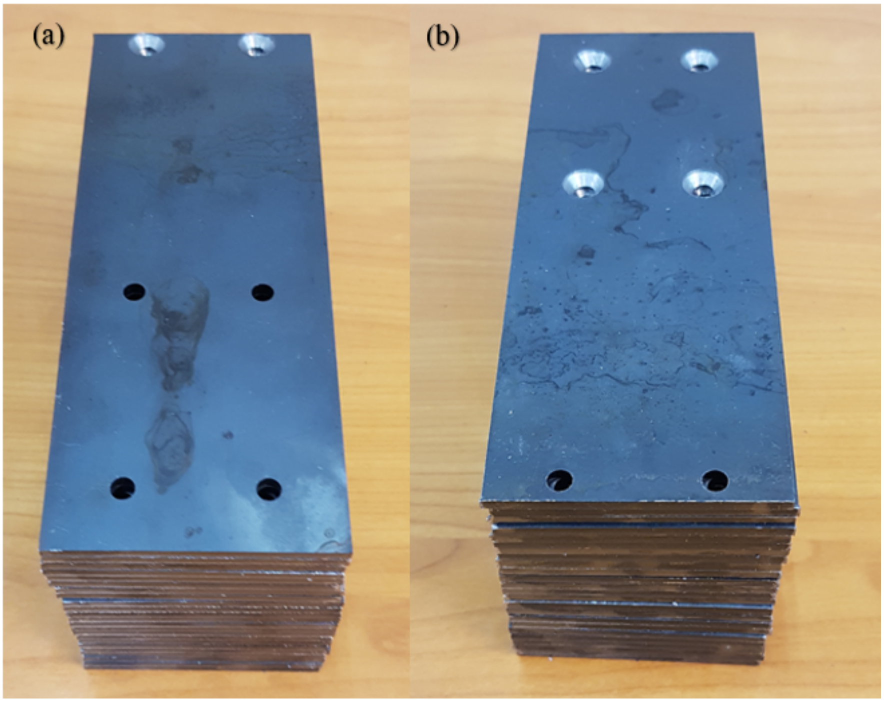

Figure 5.12. 24 pieces of 3 mm plates countersunk to be connected to a) cross flexures, b) triangular blocks.

2 mm steel plates indicated by number 1.1 in Figure 4.8 are cut by laser to be bolted to the cross flexures and walls. Their edges are bent before assembly (see Figure 5.13) so that the surfaces are in parallel contact with the wall plate and cross flexures.

Figure 5.13. 2 mm plates before and after bending the edges.

1 mm steel plates indicated as 1.2 in Figure 4.8 are also cut by laser. Their edges are slotted to make sliding possible between the two parts it is bolted between. After laser cutting, each piece is bent according to a template is prepared using 3D model (see Figure 5.14).

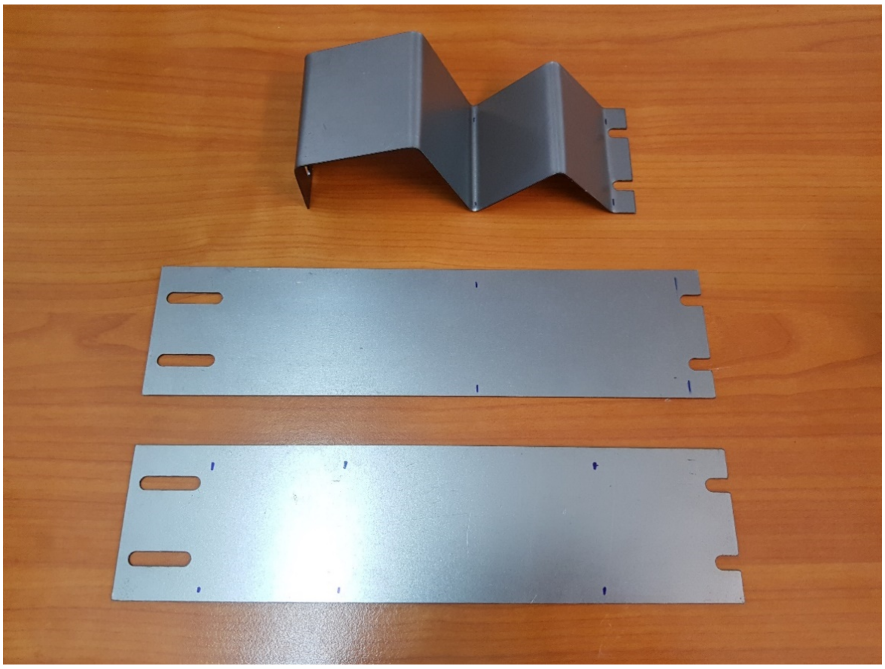

Figure 5.14. 1 mm plates before and after bending operations.

Cross and straight flexures are produced by wire EDM method from 10 mm steel plates (see Figure 5.15).

To be able to use bolts for connections, half of the straight components are threaded and the other half are countersunk as shown in Figure 5.16.

Figure 5.15. Cross flexures cut from 10 mm plate by wire EDM.

Figure 5.16. Cross and straight flexures cut from 10 mm plate by wire EDM.

Each quarter mechanism contains a cross and straight flexure assembly at their tips. To avoid friction between flexures, spacer elements cut by laser are put between each part as shown in Figure 5.17. Notice that there is no spacer between the middle two parts as they are identical and flex the same way. There are two types of these assemblies named as top and bottom flexure assemblies. One of them has countersink on one side and the other has threads on both sides as shown in Figure 5.18.

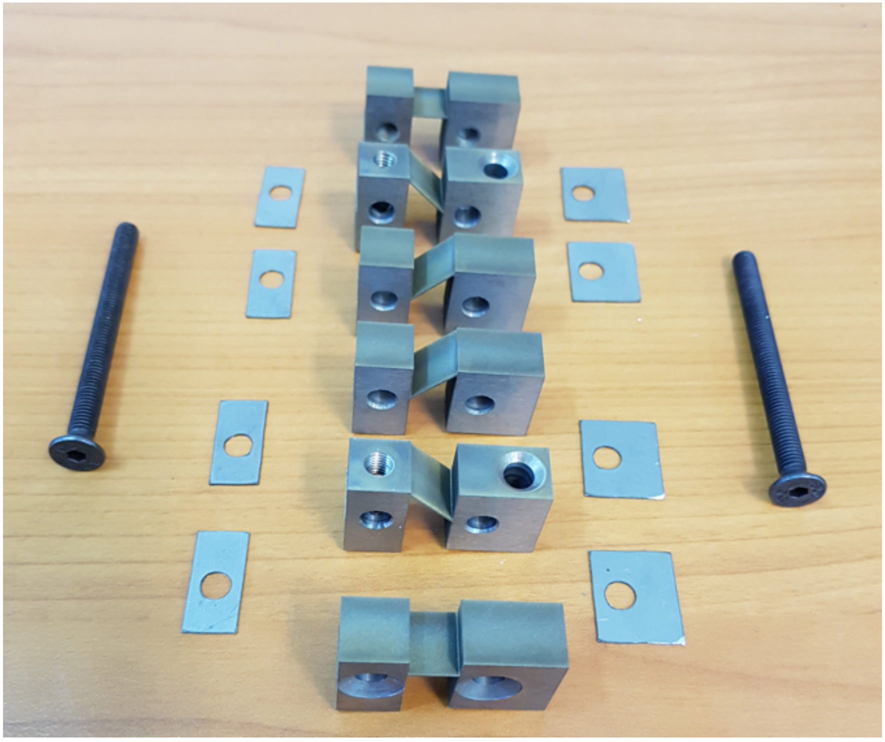

Figure 5.17. Cross and straight flexure assembly parts before assembly.

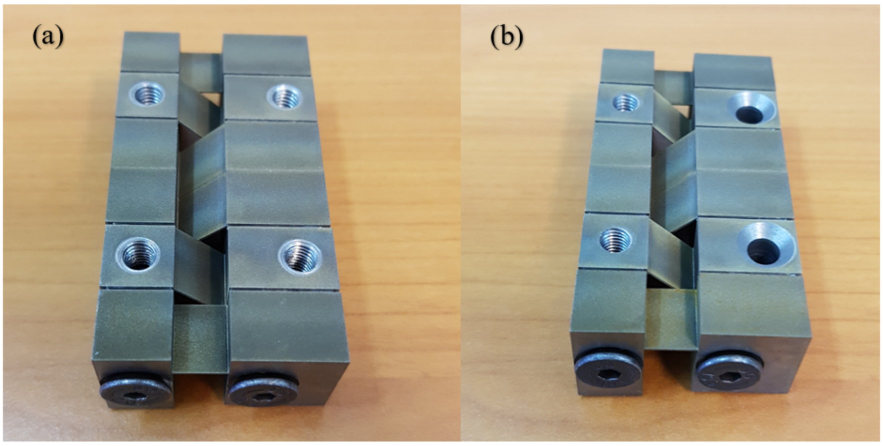

Figure 5.18. Cross and straight flexure assembly used in a) top quarter, b) bottom quarter.

24 of each of these two assembly types are produced (see Figures 5.19 and 5.20).

Figure 5.19. 24 top flexure assembly.

Figure 5.20. 24 bottom flexure assembly.

To fix the elastic components cut by laser, steel parts with 3 mm thickness are used as fixing plates. These parts are countersunk after laser cutting. Half of the fixing plate components are cut with bolt holes with 32 mm separation, while the other half are cut with 52 mm separation.

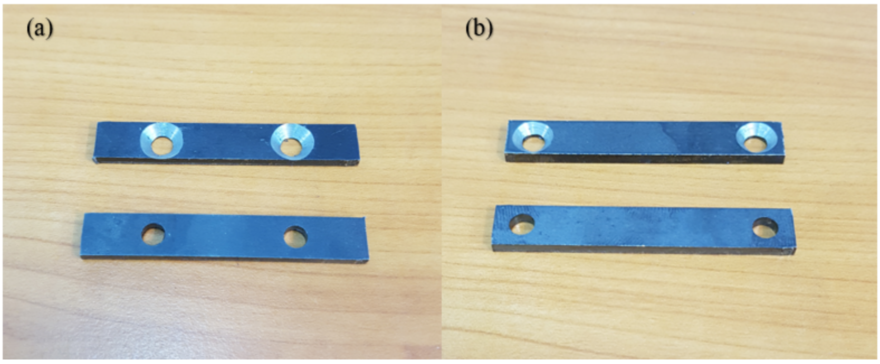

Figure 5.21. Steel fixing plates with bolt hole separation of a) 32 mm b) 52 mm.

48 pieces of each type are produced.

Figure 5.22. 48 pieces of fixing plate with 32 mm hole separation.

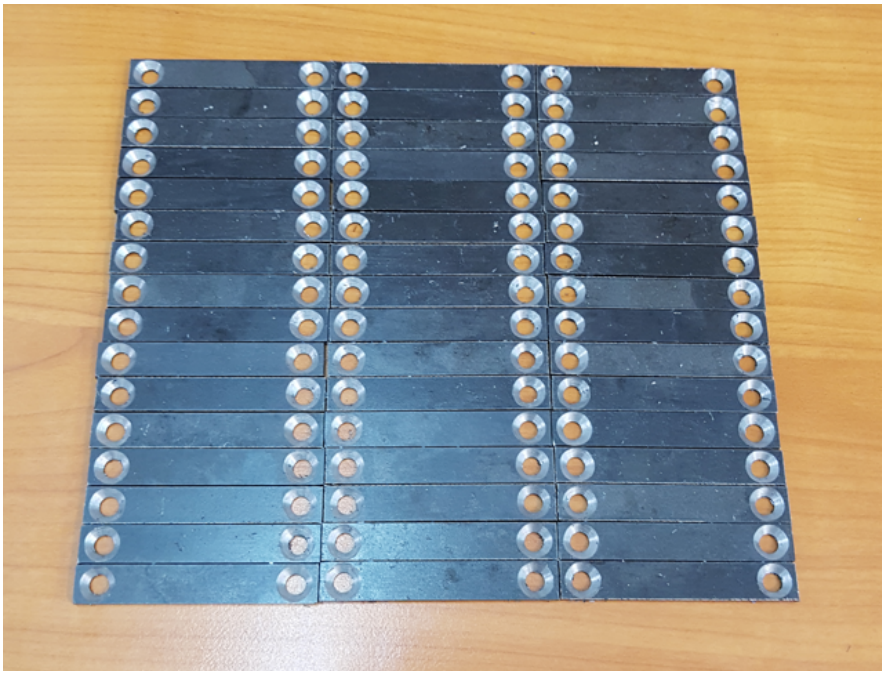

Figure 5.23. 48 pieces of fixing plate with 52 mm hole separation.

After the plates are produced, mechanism mounted between the RCR mechanisms are ready to be assembled. After long and short wall assemblies are completed, they brought together using long and short flexures. Stages for the assembly of long wall and short wall assemblies are depicted in Figures 5.24, 5.25, 5.26, 5.27, 5.28, 5.29 for long wall assembly and Figures 5.30, 5.31, 5.32, 5.33 and 5.34 for short wall assembly.

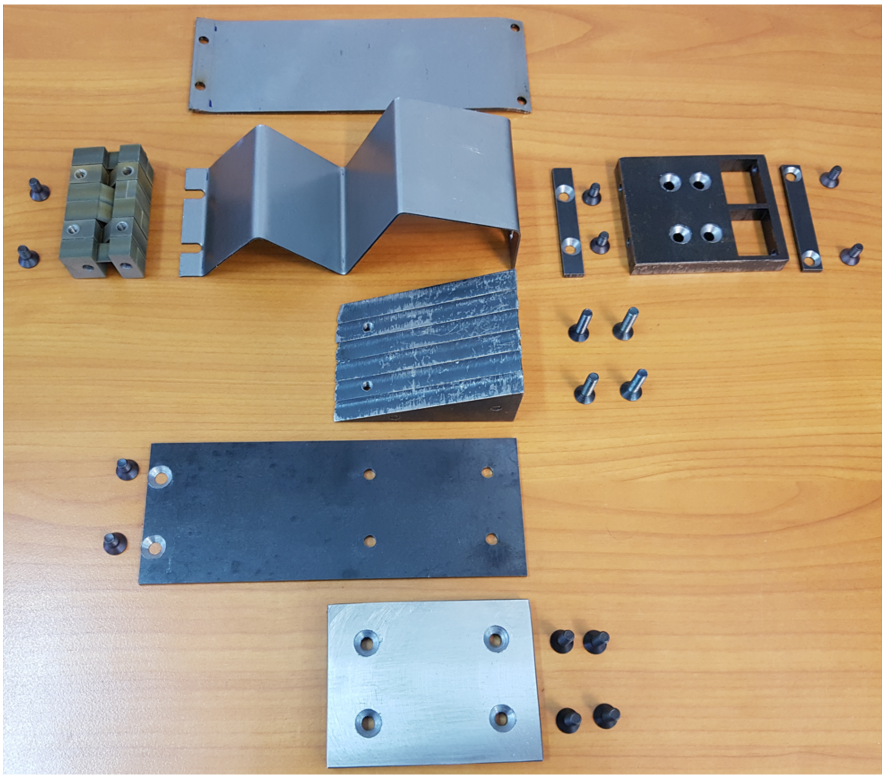

Figure 5.24. Long wall assembly components before assembly.

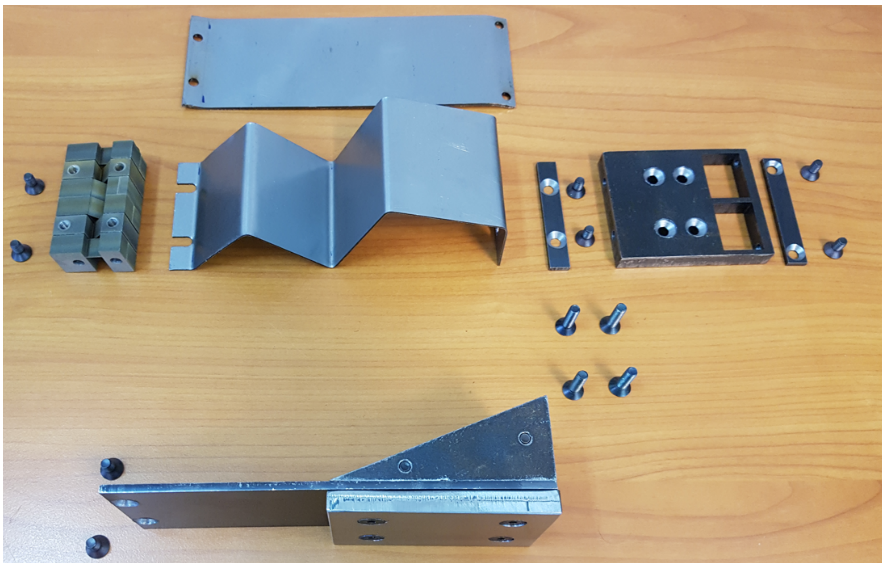

Figure 5.25. Fastening the triangular block and 8.5 mm thick plate to the 3 mm plate.

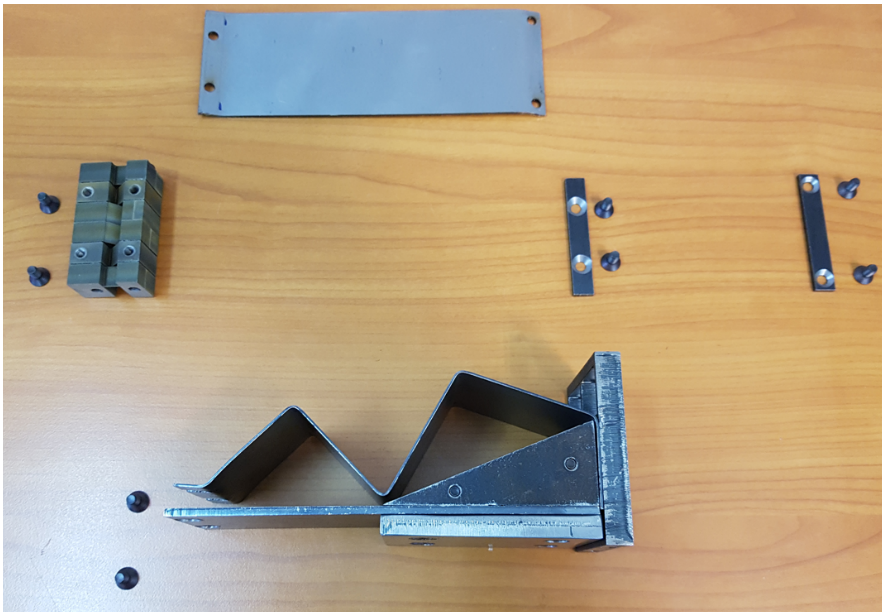

Figure 5.26. Fastening the long wall and 1 mm plate to the triangle prisms.

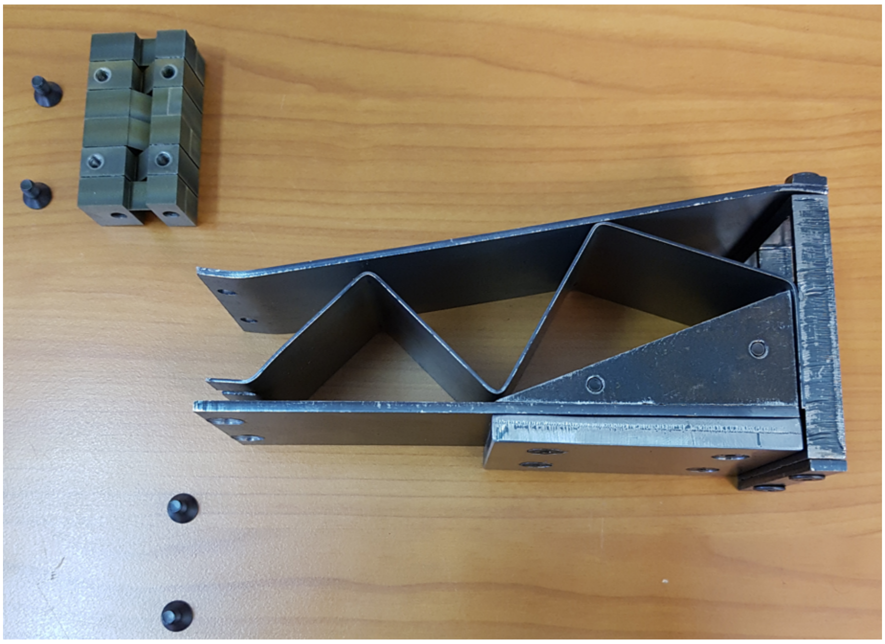

Figure 5.27. Fastening the 2 mm top cover plate to the long wall component.

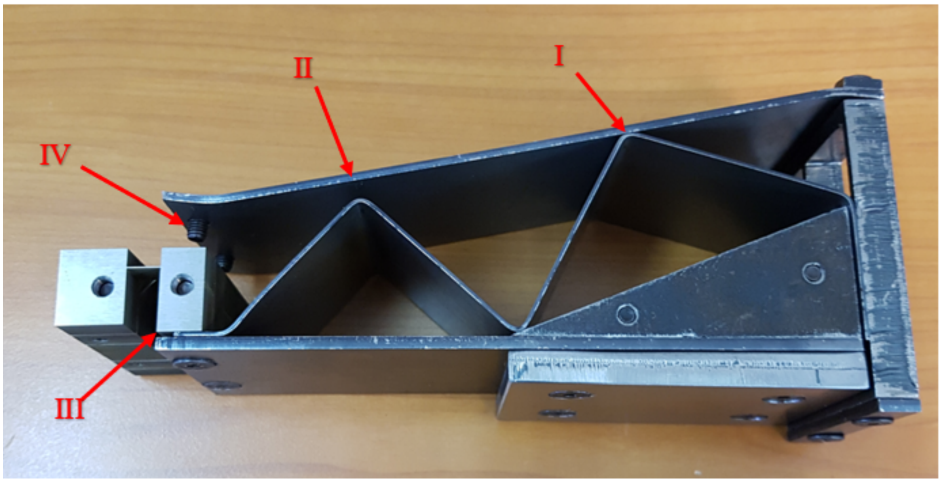

Figure 5.28. Lining up the cross-straight flexure assembly between the plates.

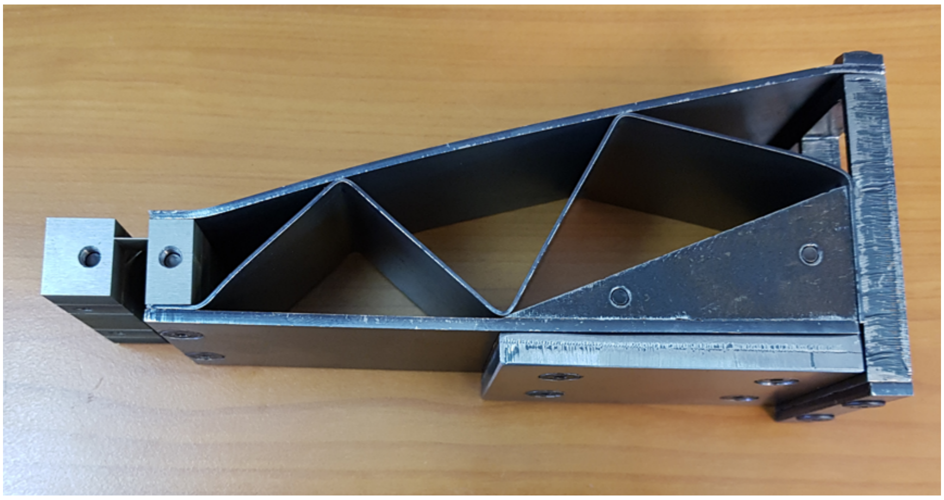

Figure 5.29. Fastening the bolts at the top and bottom of the cross-straight flexure assembly such that the 1 mm plate is trapped inside the mechanism.

As shown in Figure 5.28, 1 mm plate is in contact with the top cover plate from point I while there is no contact at point II. Also, there is space for the 1 mm plate to slip into at point III. When the point IV is pressed down onto the cross flexures and fastened, 2 mm top and 3 mm bottom cover plates flex and apply pressure onto the 1 mm plate. As a result, contact at point II is obtained. Moreover, because of the force exerted to the 1 mm plate, tip of the plate slides towards point III. After fastening all the bolts, 1 mm plate is completely constrained between the 2 mm and 3 mm plates and act as a rigid connection. Thanks to this method, mechanism can be reassembled after a possible installation failure. During vibration testing, it is observed that these points never lost contact. Therefore, permanent connection methods like welding is not required.

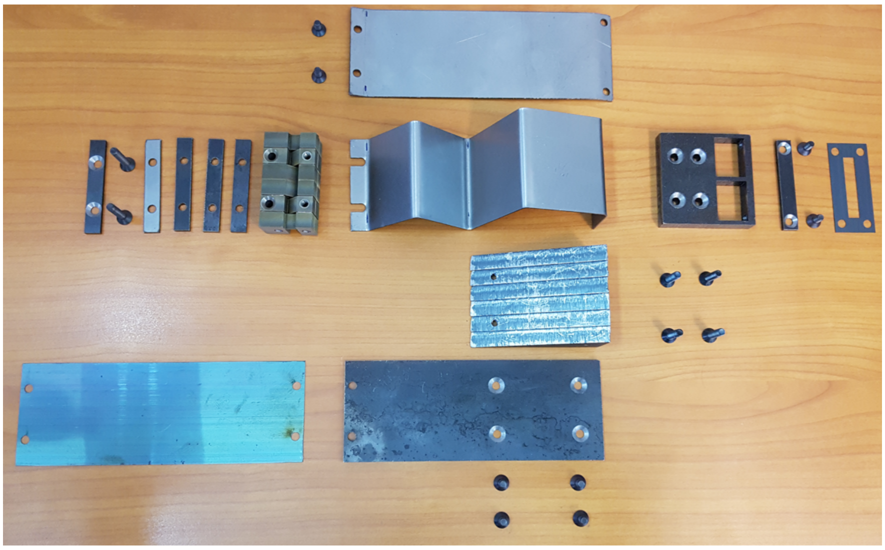

Figure 5.30. Short wall assembly components before assembly.

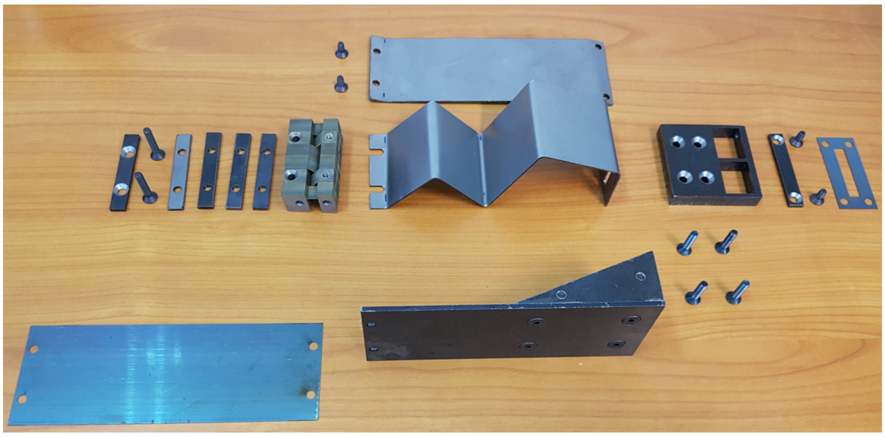

Figure 5.31. Fastening the triangular block to the 3 mm plate.

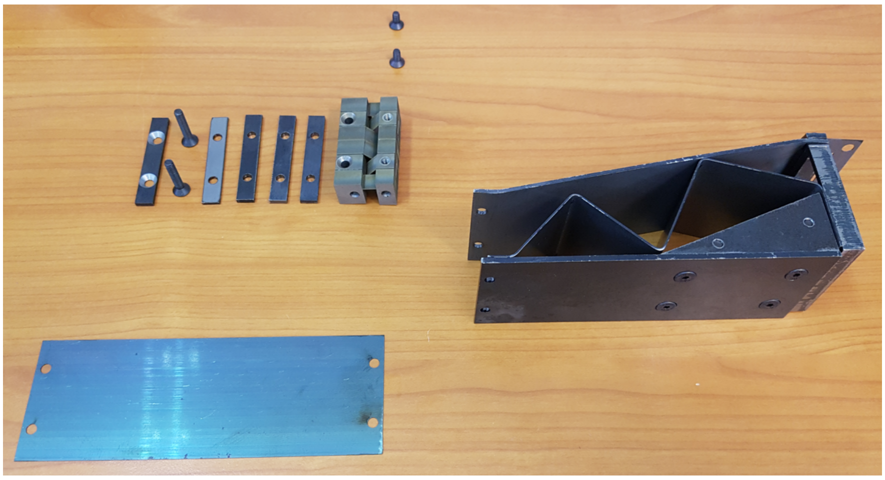

Figure 5.32. Fastening the short wall and 1 mm plate to the triangular block. On top of the short wall component, 2mm top cover plate, short flexure and a cover plate is installed.

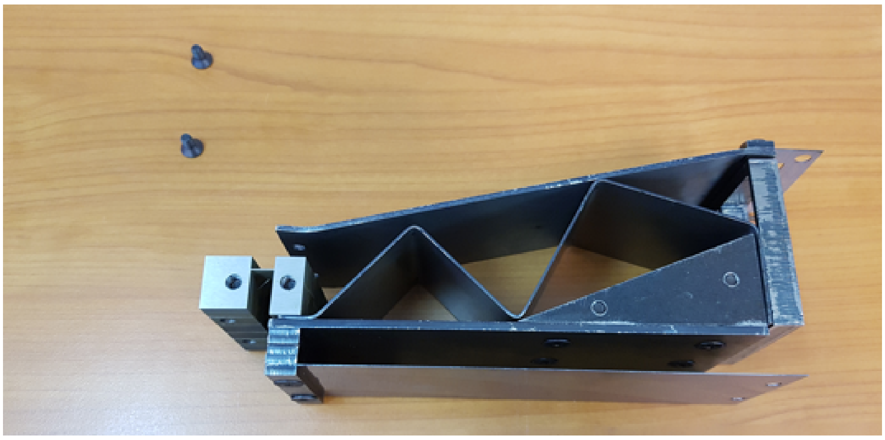

Figure 5.33. Lining up the cross-straight flexure assembly between the plates. Installing the long flexures at the bottom of the 3 mm plate.

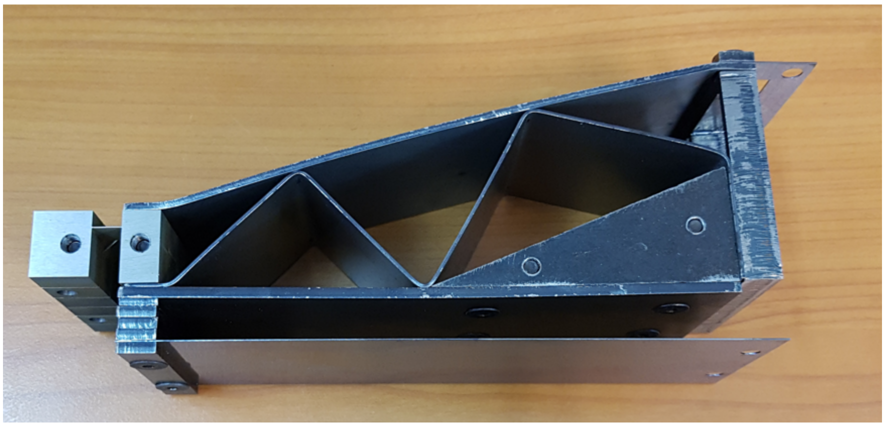

Figure 5.34. Fastening all the bolts and trapping the 1 mm plate inside the mechanism.

Long and short wall assemblies are connected to each other from long flexures to obtain a half mechanism as shown in Figure 5.35.

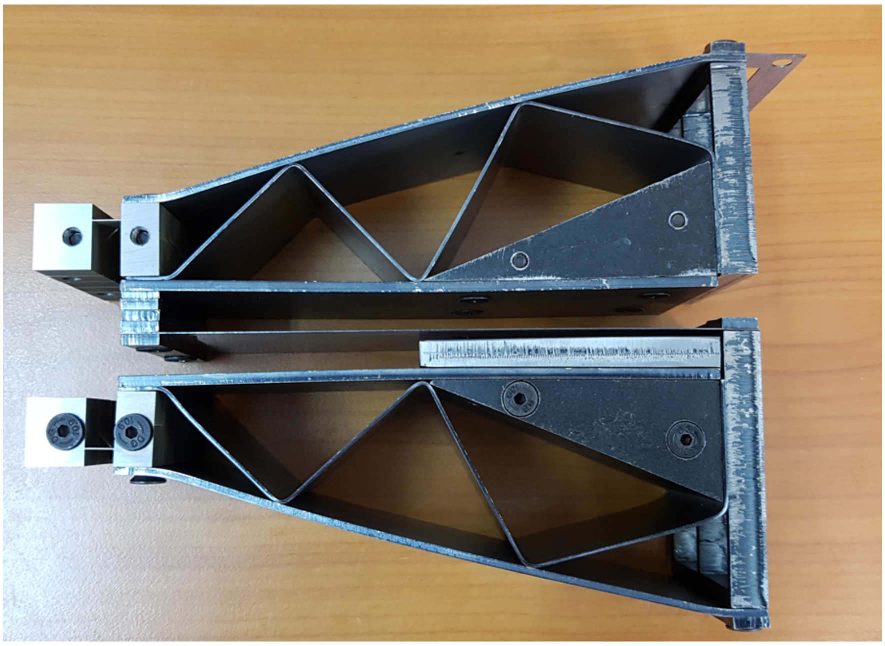

Figure 5.35. Connecting the long wall and short wall assemblies from the long flexure components.

After that two half assemblies are brought together by the short flexures. For this step, bolts at the top of the walls are loosened and the short flexures are installed between the 2 mm plates and cover plate components as shown in Figure 5.36.

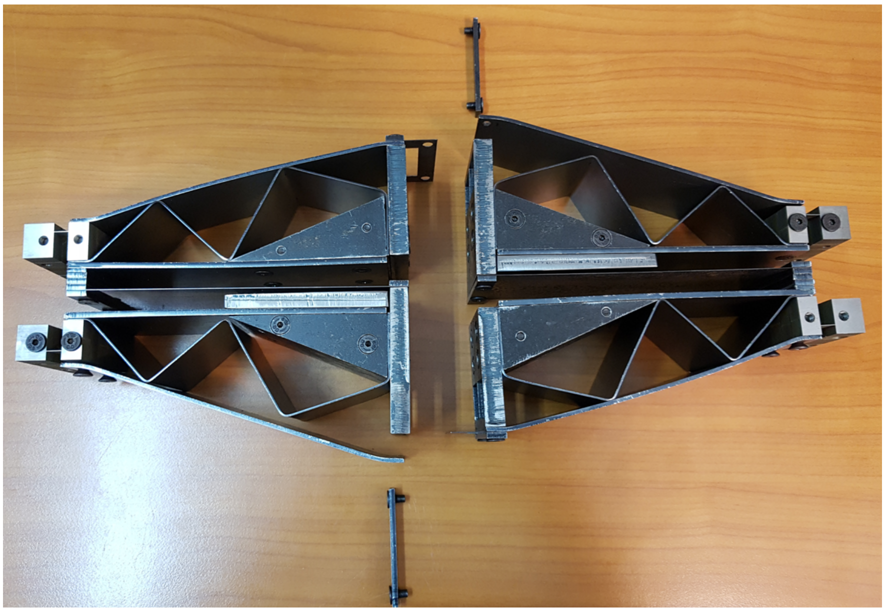

Figure 5.36. Connecting the two half mechanisms to each other from the short flexure components.

By assembling 12 mechanism as described above, necessary amount of mechanisms to build an octahedron is completed. These mechanisms are brought together via steel spherical nodes (see Figure 5.37) along with four pairs of RCR mechanisms (see Figure 5.38) connected to the nodes by M12 bolts (see Figure 5.39). Firstly, the 1st stages are bolted to the spherical nodes in a correct position (see Figure 5.40), then the 2nd stages are bolted the 1st stage via M22 bolts (see Figure 5.41). For each inertial amplification mechanism, 2 RCR mechanisms are used. So, using 24 RCR mechanisms and 6 spherical nodes are assembled to obtain 6 RCR assembly (see Figure 5.42).

Figure 5.37. Steel balls that are used at the corners of the octahedron structure.

Figure 5.38. First (left) and second (right) stages of RCR mechanism.

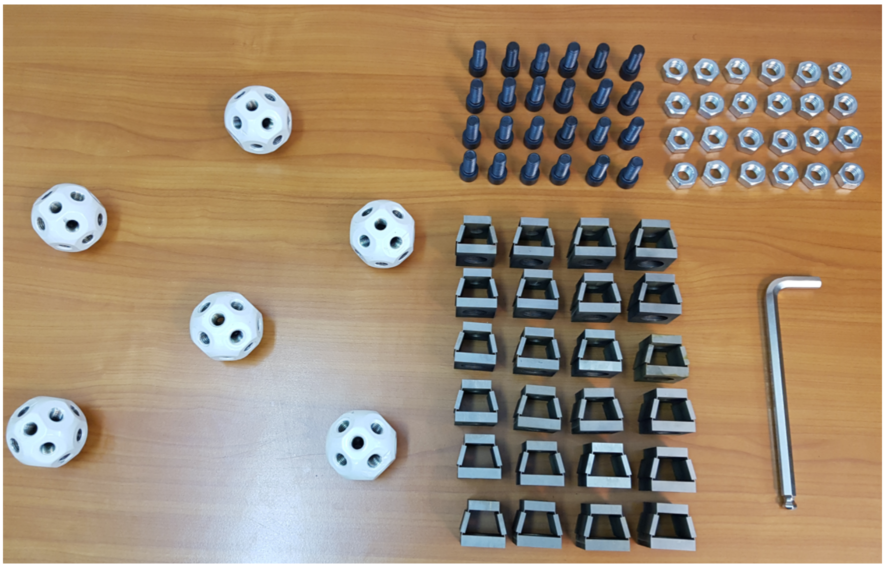

Figure 5.39. RCR mechanisms and corner balls before assembly.

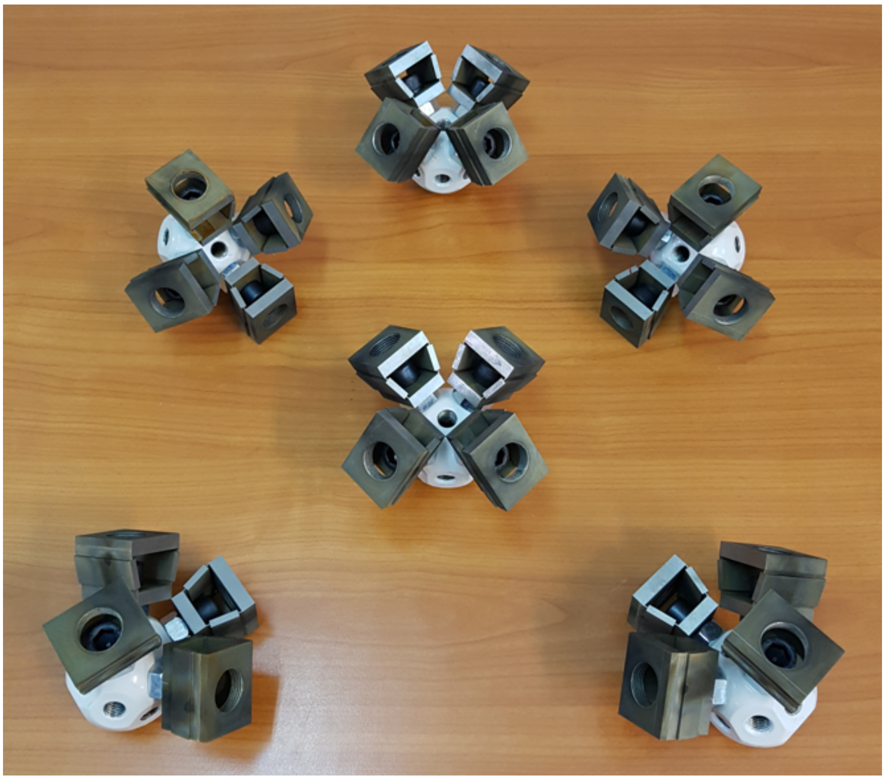

Figure 5.40. 1st stages of RCR mechanisms are attached to the corner nodes.

Figure 5.41. 2nd stages of RCR mechanisms before assembly.

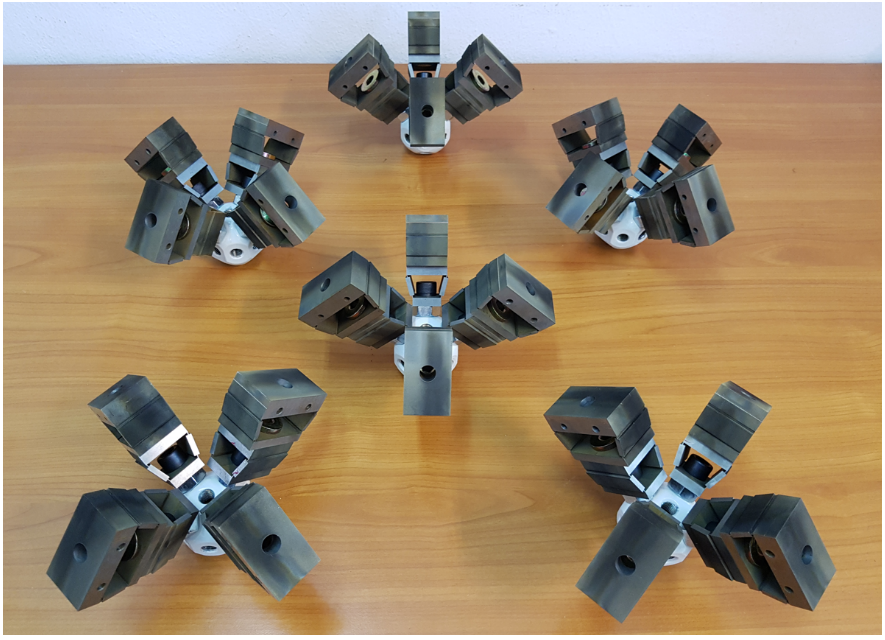

Figure 5.42. 2nd stages of RCR mechanisms after assembly.

Then, RCR mechanisms are connected to the inertial amplification mechanisms using two M5 bolts on each side (see Figure 5.43).

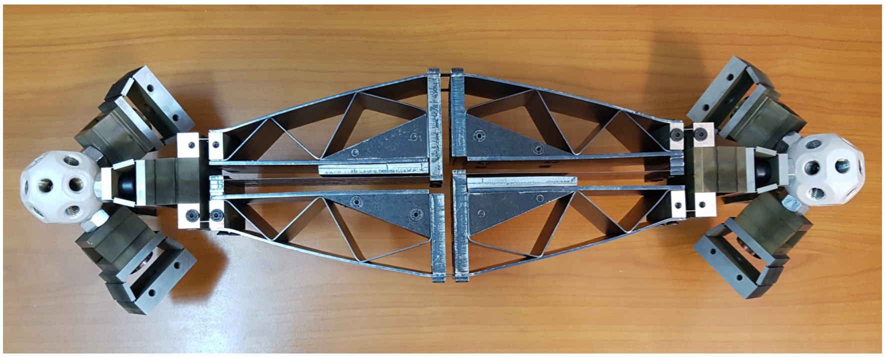

Figure 5.43. A fully assembled inertial amplification mechanism.

An inertial amplification mechanism assembly is completed after RCR mechanisms are attached to the structure. For the upper and lower pyramids that will deform under their own weight, short flexures are prestressed according to the calculated deformation (see Figure 5.44) so that the octahedron structure will be in neutral position when hung from the horizontal corners.

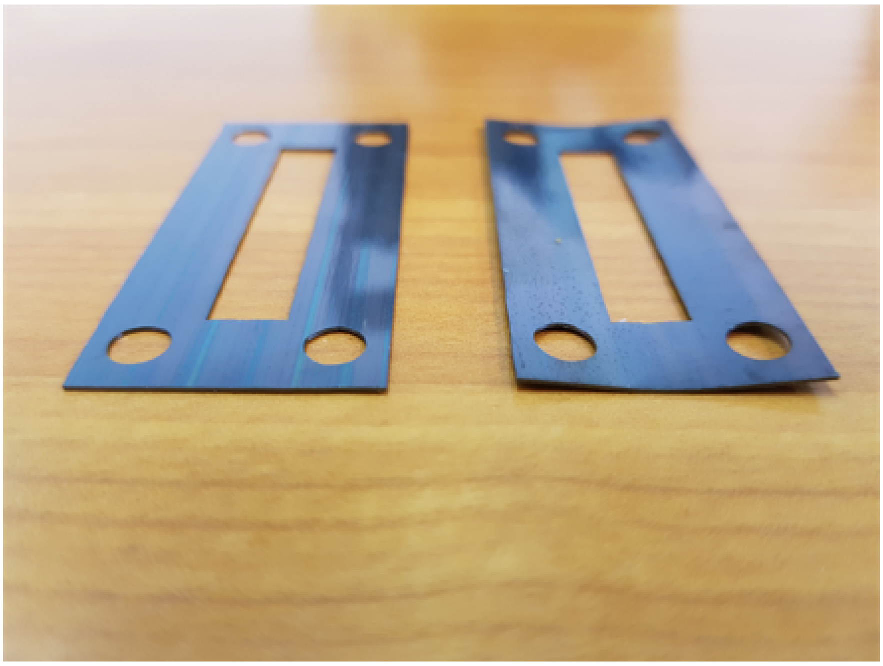

Figure 5.44. Short flexures before and after prestressing.

When these short flexures are used, the neutral position of an inertial amplification mechanism is flexed inwards (closed) for bottom pyramid units (see Figure 5.45), and outwards (opened) for the upper pyramid units (see Figure 5.46).

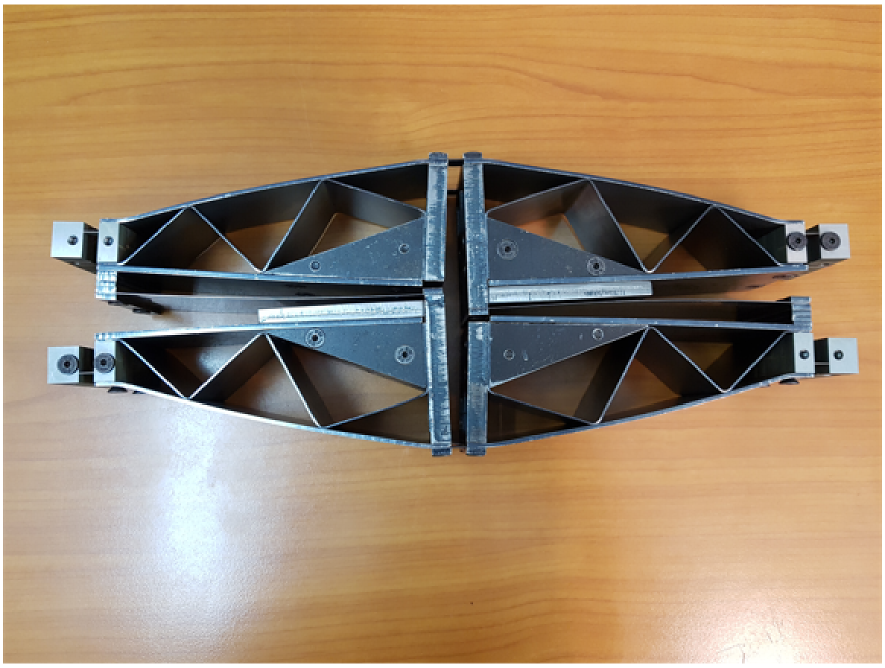

Figure 5.45. Inertial amplification mechanism with prestressed short flexure, mounted to apply force on closing direction.

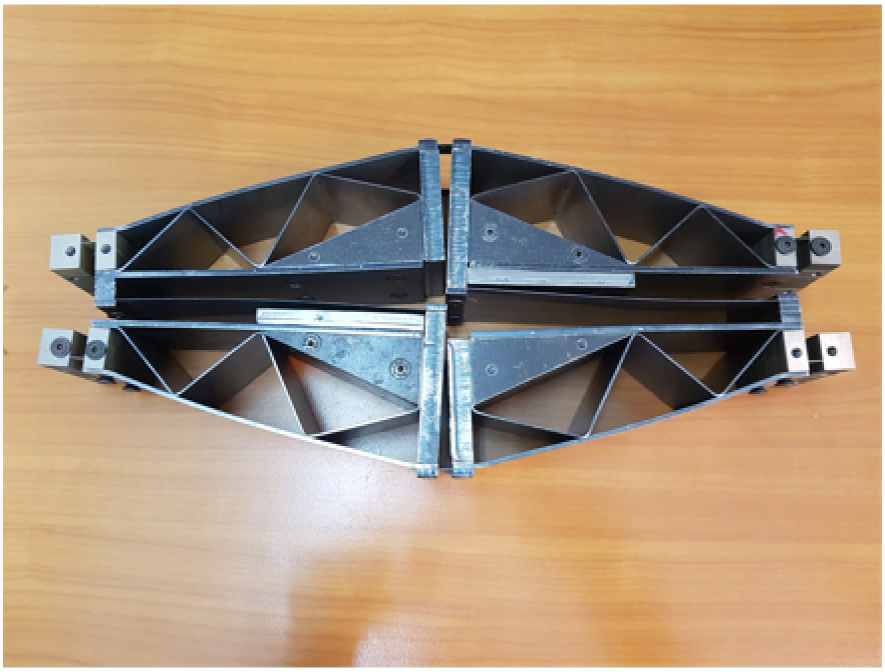

Figure 5.46. Inertial amplification mechanism with prestressed short flexure, mounted to apply force on opening direction.

To build up the octahedron, initially 4 mechanisms on the same plane are assembled as shown in Figures 5.47 and 5.48. For the top and bottom pyramids, two mechanism are assembled in L shape (see Figure 5.49) around a corner component, then placed on the octahedron assembly and the remaining two mechanisms are attached to the assembly as shown in Figures 5.50 and 5.51.

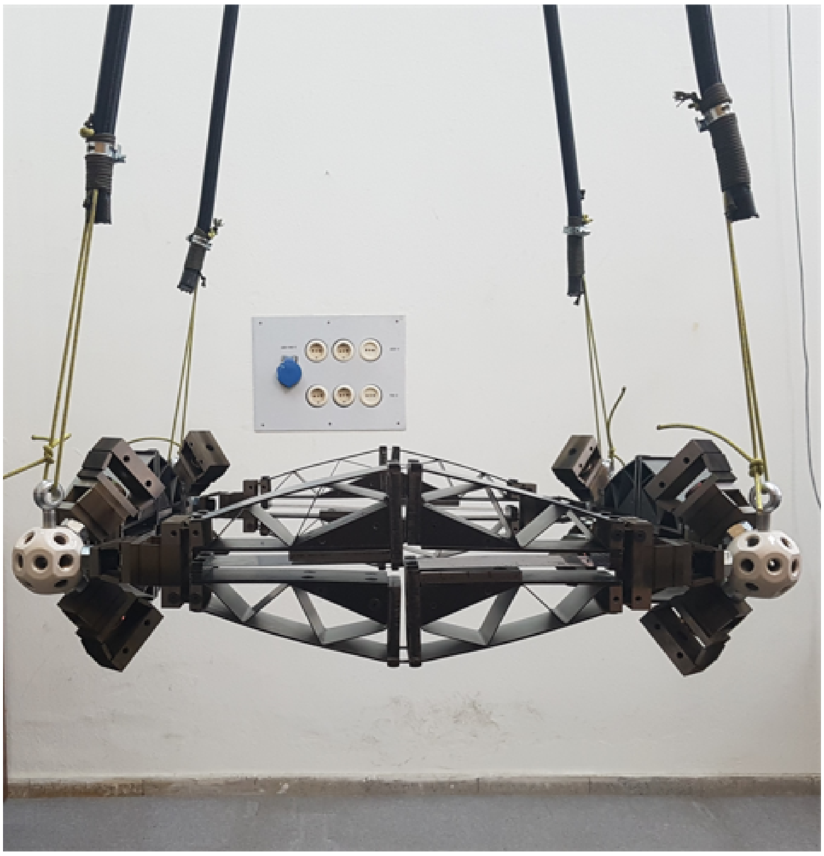

Figure 5.47. Side view of the assembly of 4 mechanisms on the same plane.

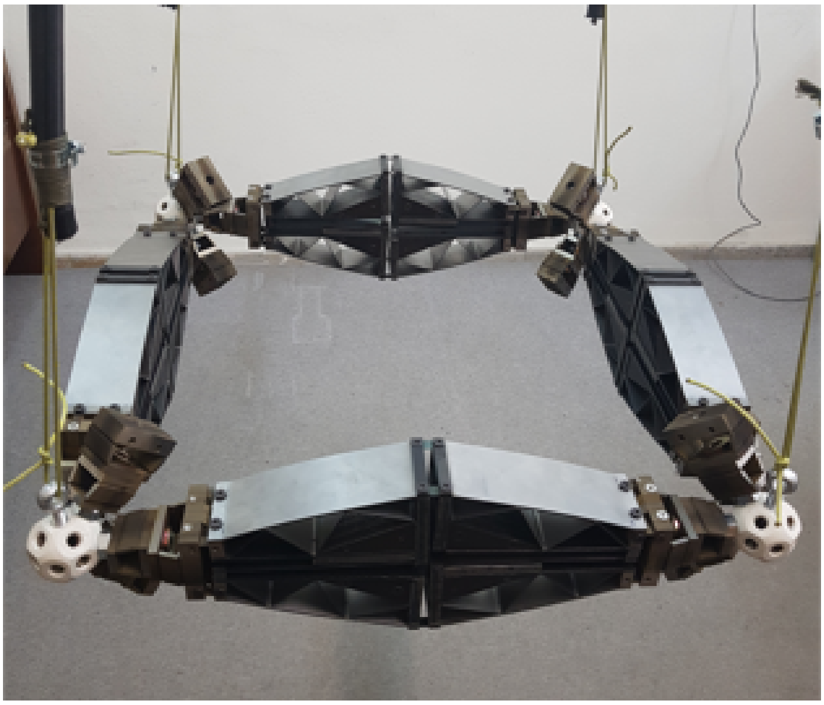

Figure 5.48. Isometric view of assembly of the 4 mechanisms on the same plane.

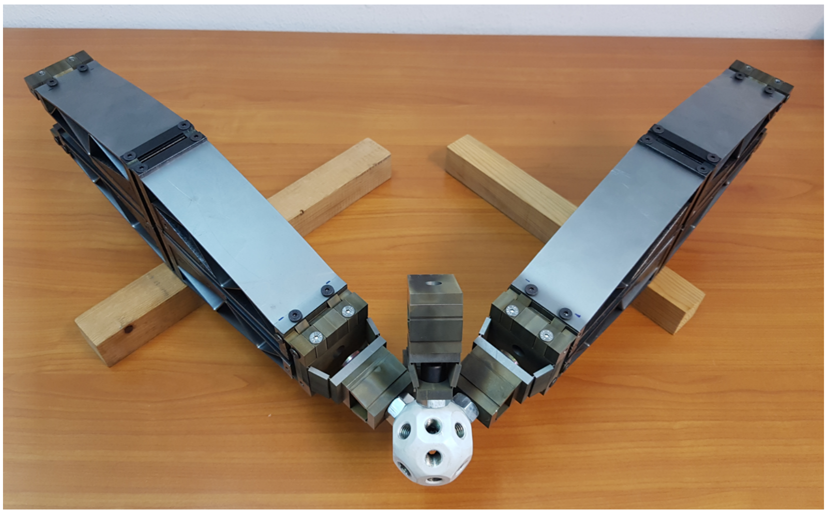

Figure 5.49. Two mechanism attached to the opposite sides of a corner mechanism.

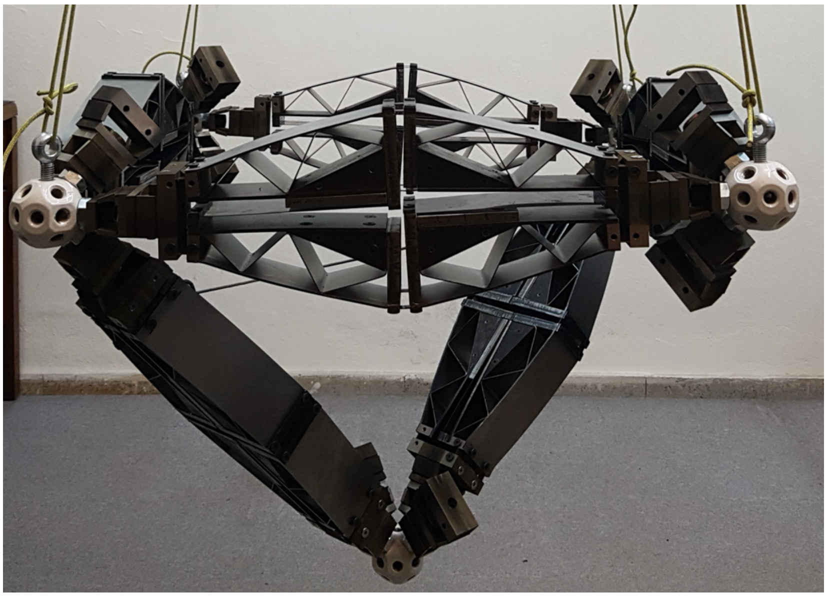

Figure 5.50. Bottom corner along with two mechanisms is attached to the 4 mechanisms on the horizontal plane.

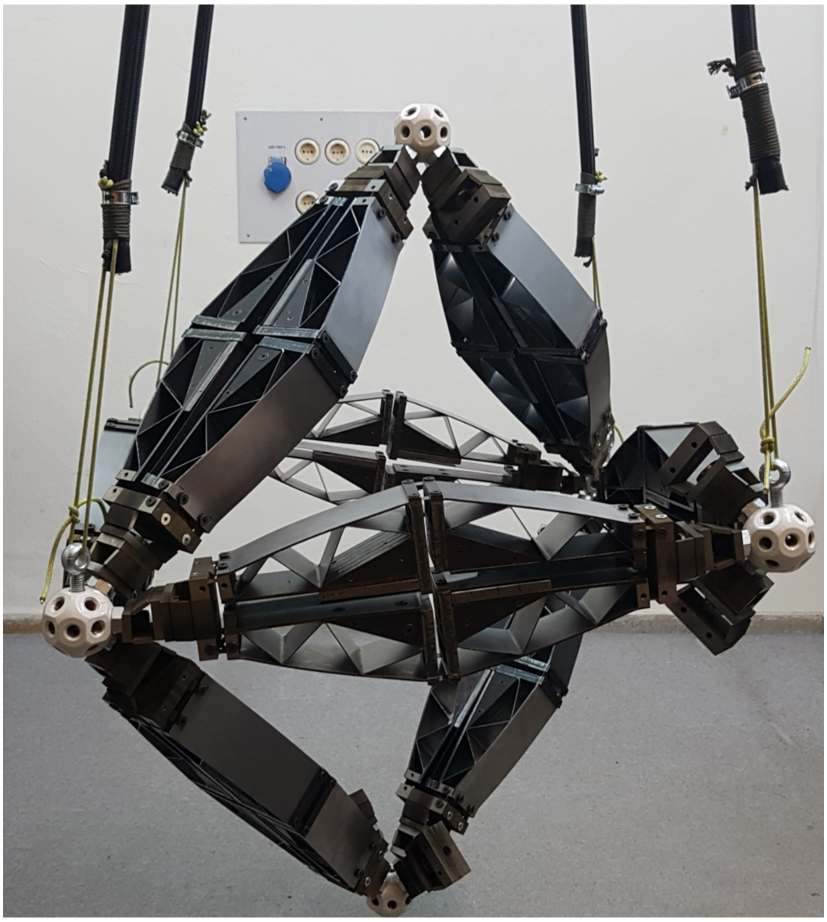

Figure 5.51. Top corner along with two mechanisms is attached to the 4 mechanisms on the horizontal plane.

After the remaining mechanisms are attached, a complete octahedron structure is obtained as shown in Figures 5.52, 5.53, 5.54.

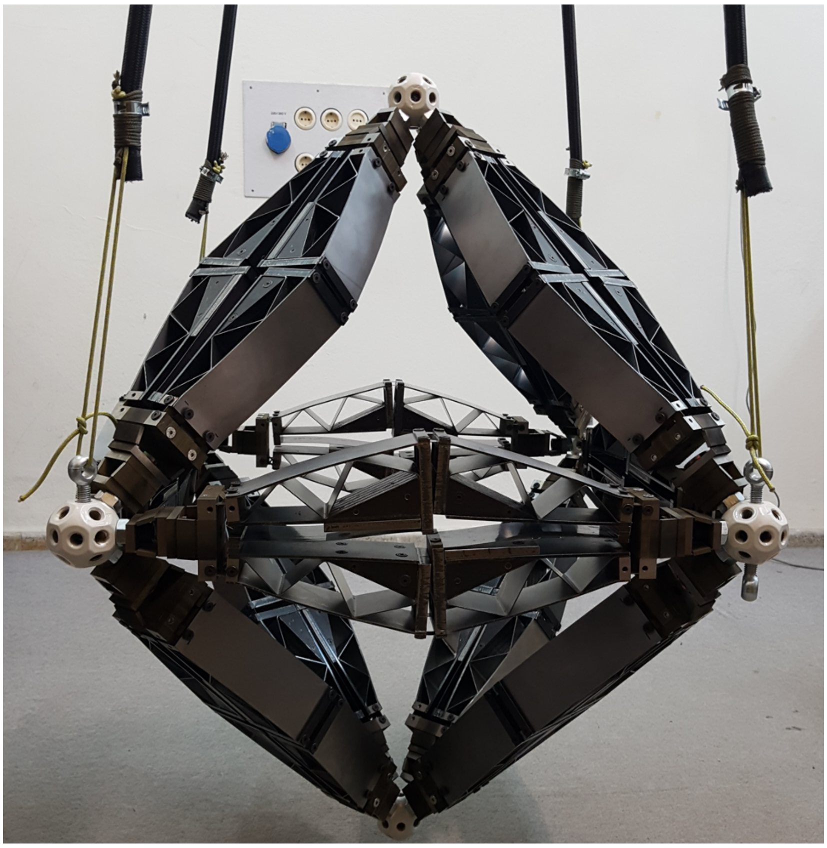

Figure 5.52. Side view of the octahedron structure made up of 12 inertial amplification mechanisms.

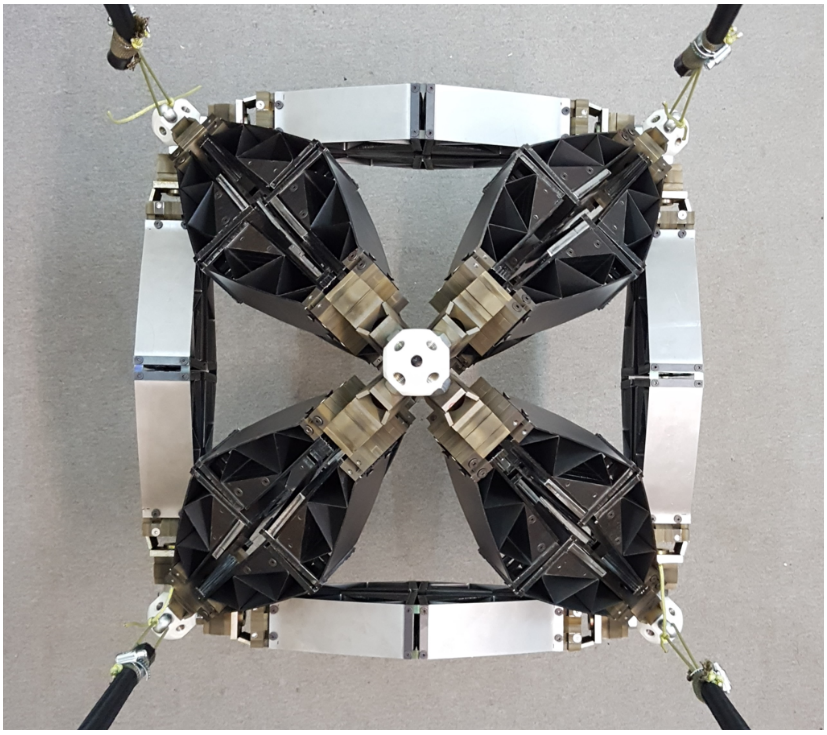

Figure 5.53. Top view of the octahedron structure made up of inertial amplification mechanisms.

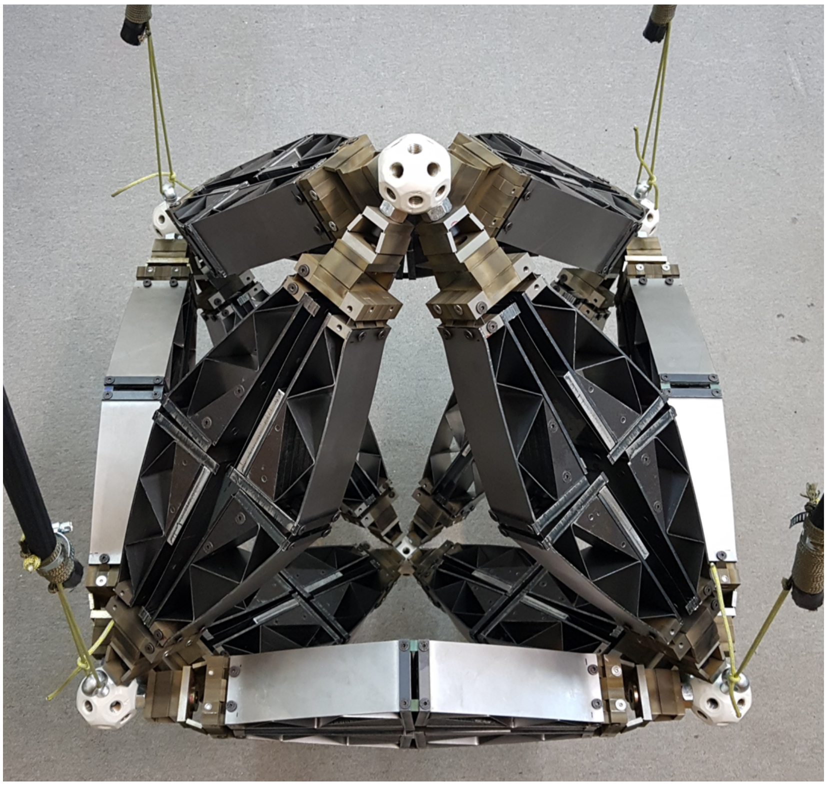

Figure 5.54. Isometric view of the octahedron structure made up of inertial amplification mechanisms.

6. EXPERIMENTS AND RESULTS

To verify the vibration isolation capability of an octahedron made up of inertial amplification mechanisms, series of tests are conducted. The octahedron structure is excited both by hammer and shaker, and acceleration data is collected from different locations.

Additionally, the same sized truss structure is also tested to compare the vibration isolation characteristics of these structures as shown in Figure 6.1. Hammer testing tools can be seen in Figure 6.2. Data collected from accelerometer and the hammer can be used to calculate transmissibility of the structure.

Figure 6.1. Test benches of octahedron structures made up of inertial amplification mechanisms (left) and steel rods (right).

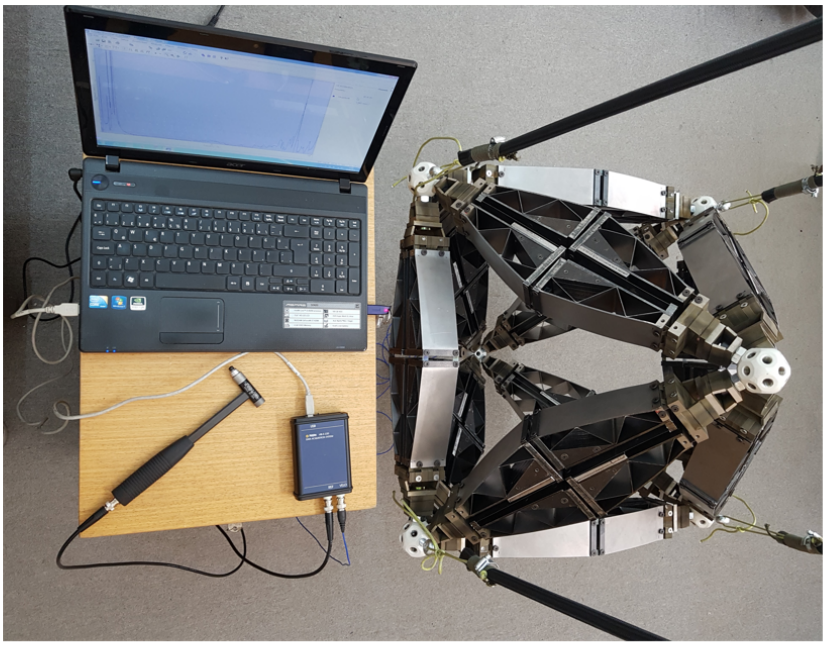

Figure 6.2. Hammer and accelerometer connected to the data acquisition device.

Firstly the original truss structure is tested in horizontal (see Figure 6.3) and vertical directions (see Figure 6.3).

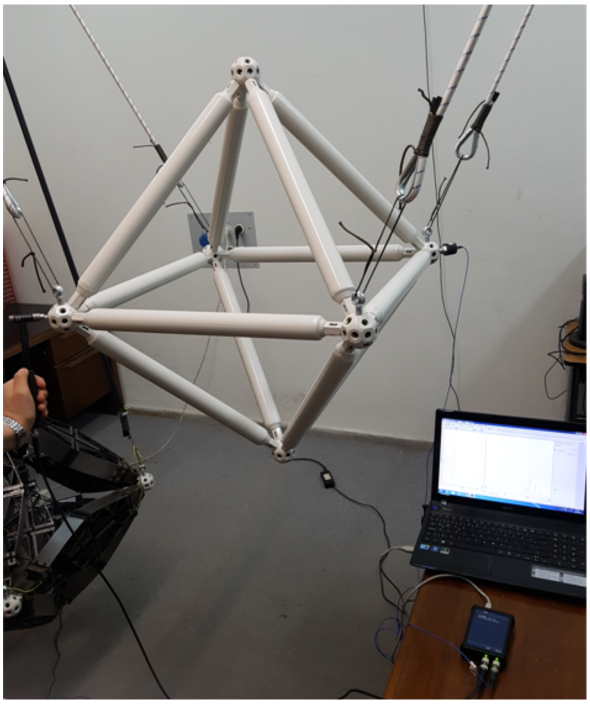

Figure 6.3. Hammer excitation and measurement in horizontal direction.

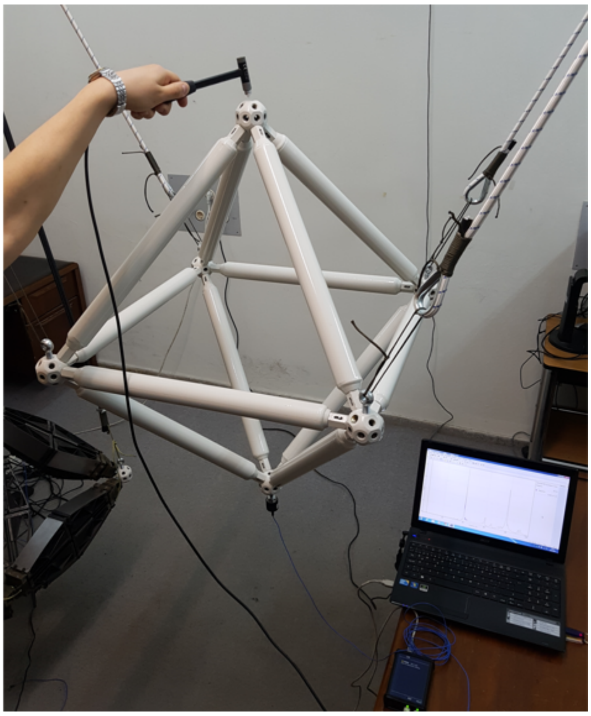

Figure 6.4. Hammer excitation and measurement in vertical direction.

As a result, the graph in the Figures 6.5 and 6.6 are obtained. As seen in Figure 6.6, there is no vibration isolation at low frequencies.

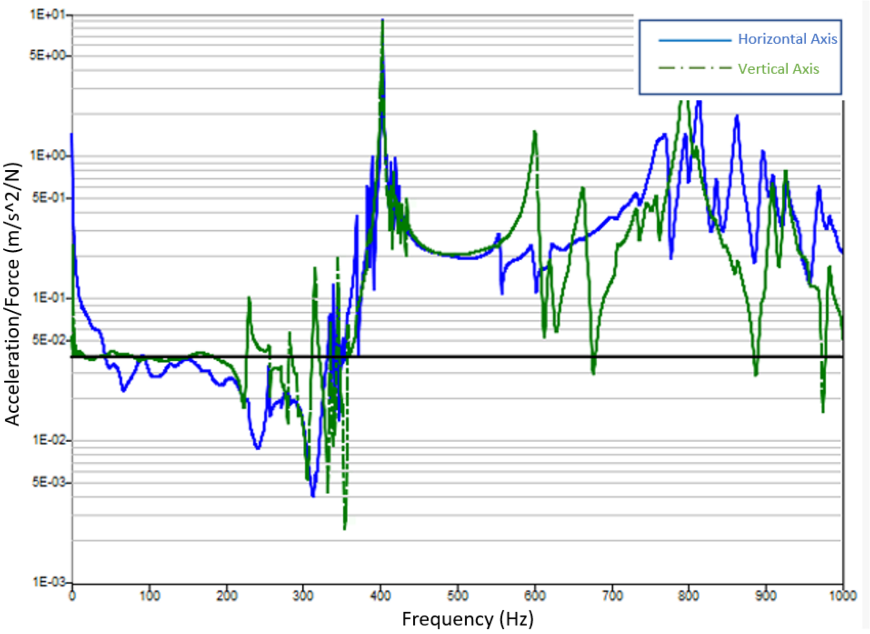

Figure 6.5. Hammer test results of the a truss structure in the range of 0-1000 Hz.

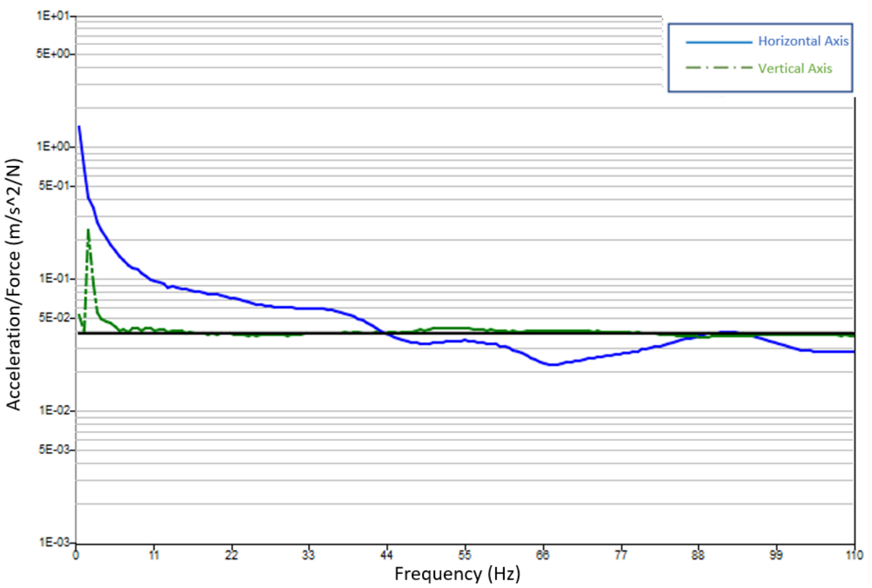

Figure 6.6. Hammer test results of the a truss structure in the range of 0-110 Hz.

Secondly, the same tests are applied to the inertial amplification mechanisms as shown in Figure 6.7. The octahedron structure is also excited in vertical and horizontal directions. As shown in Figure 6.9, there is a vibration isolation region between around 8-75 Hz for vertical and horizontal directions. Because of the symmetry of the structure, horizontal and vertical tests are expected to have similar results. However, tension caused by the elastic ropes that supports the structure and assembly errors results in deviations in the locations of the peak values. Also because of assembly errors, the long flexures are exposed to compressive forces which causes a steep decrease in their natural frequency. This is the reason why some peaks are observed inside the band gap.

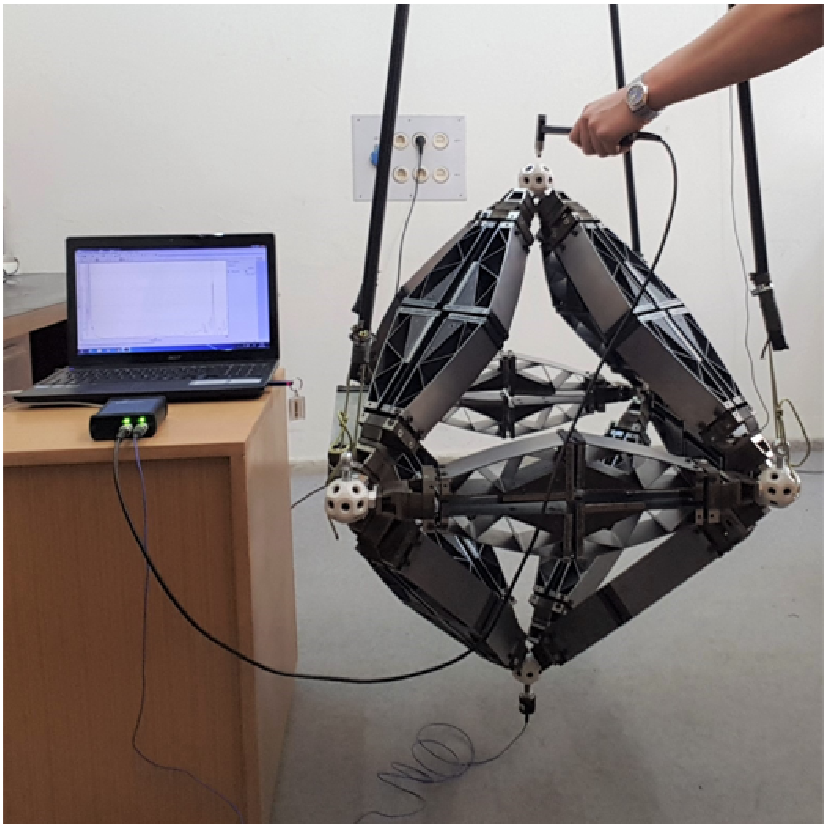

Figure 6.7. Application of hammer excitation to the octahedron structure made of inertial amplification mechanisms.

Test setup is also modeled in FEM environment to verify the numerical model. Unit load is applied in the horizontal direction as shown in Figure 6.8 and obtained results are given as red line in Figure 6.9. The numerical model shows a much smoother frequency response. However, the general trend is the same and vibration isolation occurs between 6.00 and 102.50 Hz.

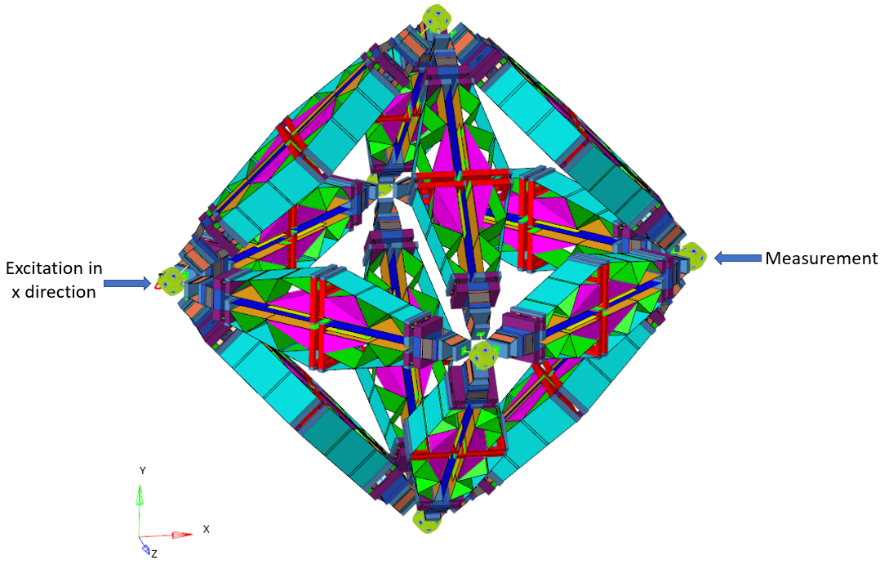

Figure 6.8. Numerical model of the test set up.

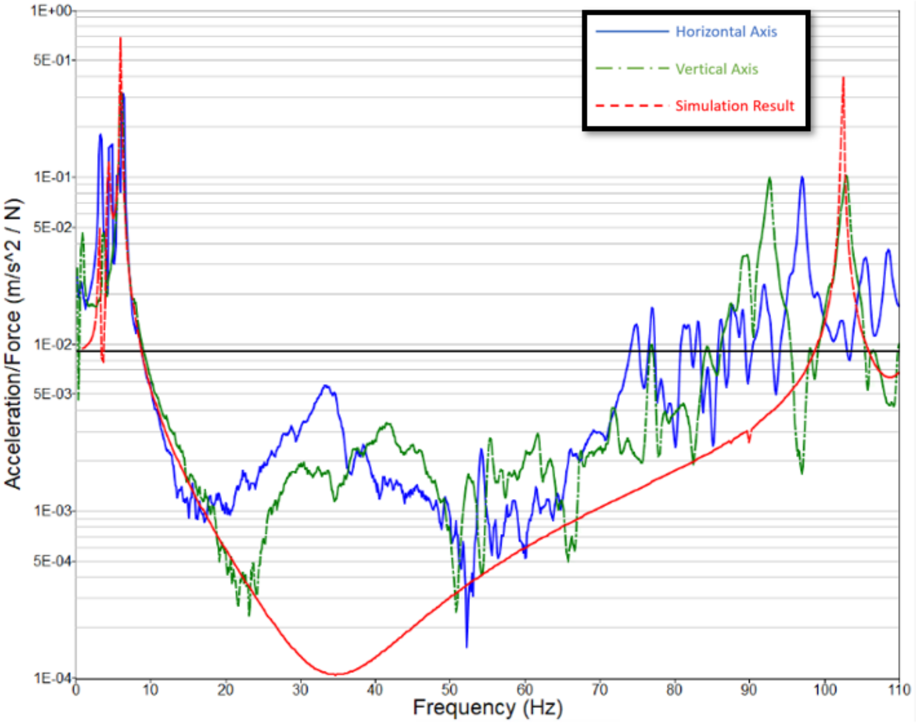

Figure 6.9. Hammer test and corresponding FRF analysis results of the a truss structure in the range of 0-110 Hz.

In addition to the hammer test, shaker test is conducted (see Figure 6.10). To observe the behavior in all directions, the system is excited in the horizontal direction while the measurement is conducted in oblique direction as shown in Figure 6.11.

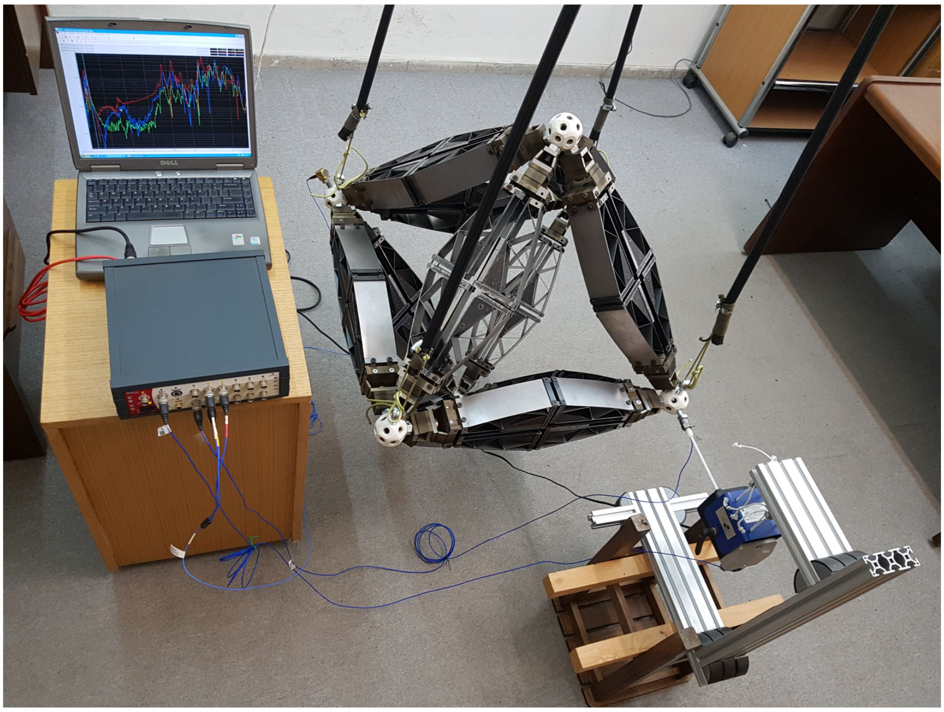

Figure 6.10. Shaker test set up.

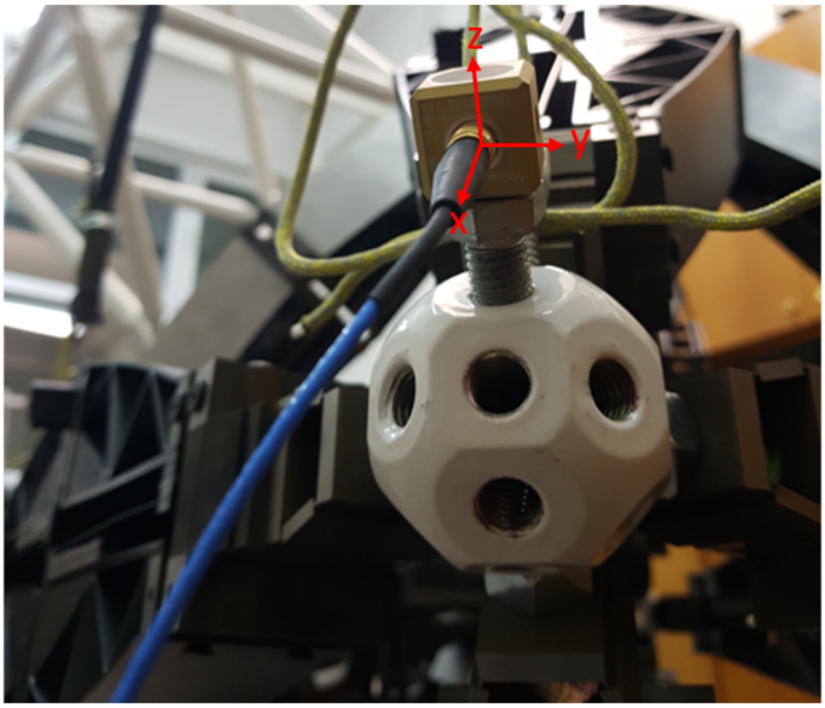

Figure 6.11. Direction of the accelerometer placed on the corner across the shaker.

As shown in Figure 6.12, measurements verify the existence of a band gap and vibration isolation is greatest in z-direction for most of the frequency range. The general behavior of the structure is in correlation with the analysis results in terms of lower limit of the band gap (see Figure 6.13). However, upper limit of the band gap shifted down due to the errors in the boundary conditions and residual stresses in the structure. Nevertheless, a very wide band gap is realized in three dimensions.

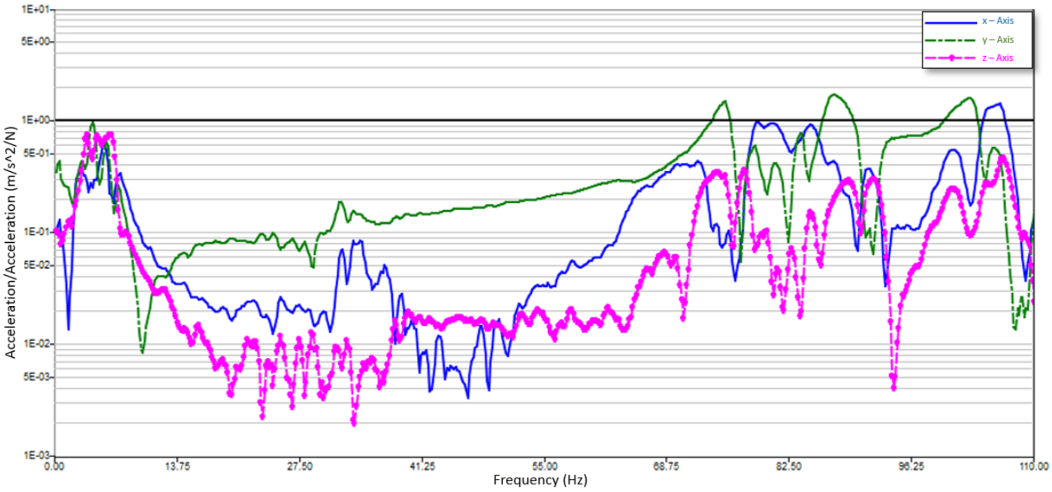

Figure 6.12. Results of the shaker test of the octahedron structure.

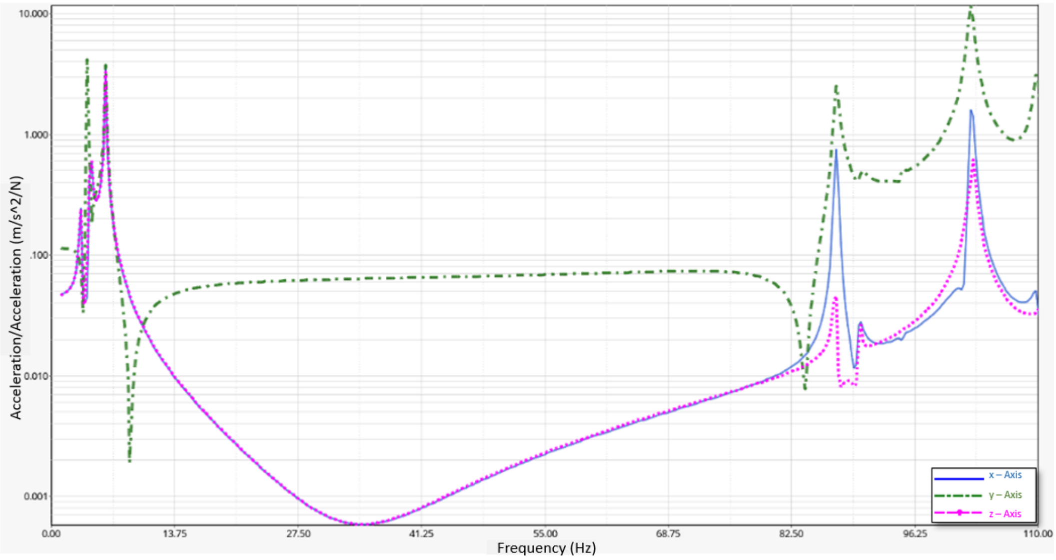

Figure 6.13. FRF analysis result on the FEM model of the octahedron structure excited and measured identically with the test.

7. CONCLUSION

In this thesis, a 3D ultrawide elastic metamaterial is designed and manufactured. The system utilized various mechanisms like cross flexures and remote center of rotation mechanisms to be able to isolate vibrations or waves in 3D. Moreover, using the FEM method, the model is parameterized and different parametric studies and optimizations are applied. As a result, the widest band gap is obtained with upper limit to lower limit ratio of 14.43.

System consists of various geometric features, some of which are flexible metal sheets, and some of them are bulk material. By analyzing the system for various geometries and thicknesses, relation between the component parameters are extracted. As a result, number of parameters is brought down to be able to apply optimization within reasonable time.

Finally, a prototype of the system is manufactured using various production methods like laser cutting and wire EDM. System is designed as a modular assembly, so that any new feature can be directly implemented on the existing prototype and be tested. This flexibility can also be considered as the first step of inertial amplification systems to be produced for the industrial use. The design is available for testing different components as long as it is compatible with the rest of the assembly. For example, shape of the central masses can be further optimized to obtain a wider spectral gap. In fact, new central mass geometries can directly be implemented to the mechanism using the existing bolt locations.

Considering the number components, connections, and delicacy of the assembly, it is quite a challenging task to obtain a test result in correlation with the simulation results. When the test results and the simulations are compared, 10-15 % difference is observed. Reasons for this difference are low modeling accuracy of the connection elements due to lack of computation power, residual stresses in the mechanism accumulated during assembly, deformation of the mechanism due to its weight and vibration of the elastic ropes used to hang the octahedron mechanism.

In the future, the system can be tuned for the desired frequency values according to application just by scaling up or down. As confirmed during scaling for manufacturing, even thought the system's natural frequencies change with the size, the ratio of the upper and lower limits of the band gap remains constant. Thus, if the designed structure is enlarged, the band gap limiting frequencies can be decreased and the system can work in the seismic frequency range.

REFERENCES

1. Yuksel, O. and C. Yilmaz, “Realization of an Ultrawide Stop Band in a 2-D Elastic Metamaterial With Topologically Optimized Inertial Amplification Mechanisms”, *International Journal of Solids and Structures*, Vol. 203, pp. 138–150, 2020.

2. Acar, G. and C. Yilmaz, “Experimental and Numerical Evidence For The Existence of Wide and Deep Phononic Gaps Induced by Inertial Amplification in Two-Dimensional Solid Structures”, *Journal of Sound Vibration*, Vol. 332, pp. 6389–6404, 11 2013.

3. Yuksel, O. and C. Yilmaz, “Shape Optimization of Phononic Band Gap Structures Incorporating Inertial Amplification Mechanisms”, *Journal of Sound and Vibration*, Vol. 355, pp. 232–245, 2015.

4. Otlu, S. N., *Ultrawide Stop Band in a 3D Elastic Metamaterial With Inertial Amplification Mechanisms Having Cross Flexure Hinges*, M.S. Thesis, Department of Mechanical Engineering, Boğaziçi Universty, Istanbul, 2022.

5. Rao, S. S., *Mechanical Vibrations*, Pearson Prentice Hall International Edition, New Jersey, NJ, USA, 2004.

6. E. N. Economou, M., Sigalas, “Stop Bands For Elastic Waves in Periodic Composite Materials”, *The Journal of the Acoustical Society of America*, Vol. 95 (4), p. 1734–1740, 1994.

7. Bacigalupo, L., A. ve Gambarotta, “Simplified Modelling of Chiral Lattice Materials With Local Resonators”, *International Journal of Solids and Structures*, Vol. 83, p. 126–141, 2016.

8. Kushwaha, M. S., “Classical Band Structure of Periodic Elastic Composites”, *International Journal of Modern Physics B*, Vol. 10 (09), p. 977–1094, 1996.

9. Shen, W. J. Y. D. W. X., H., “The Vibrational Properties of a Periodic Composite Pipe in 3D Space”, *Journal of Sound and Vibration*, Vol. 328 (1), pp. 57–70, 2009.

10. Yu, D., J. Wen, H. Shen, Y. Xiao and X. Wen, “Propagation of Flexural Wave in Periodic Beam on Elastic Foundations”, *Physics Letters A*, Vol. 376, No. 4, pp. 626–630, 2012.

11. Assouar, B. and M. Oudich, “Enlargement of a Locally Resonant Sonic Band Gap by Using Double-Sides Stubbed Phononic Plates”, *Applied Physics Letters*, Vol. 100, 03 2012.

12. Taniker, S. and C. Yilmaz, “Phononic Gaps Induced by Inertial Amplification in BCC and FCC Lattices”, *Physics Letters A*, Vol. 377, No. 31, pp. 1930–1936, 2013.

13. Xiuchang, H., J. Aihua, Z. Zhiyi and H. Hongxing, “Design and Optimization of Periodic Structure Mechanical Filter in Suppression of Foundation Resonances”, *Journal of Sound and Vibration*, Vol. 330, No. 20, pp. 4689–4712, 2011.

14. Chang, C., K. Firouzi, K. K. Park, A. Sarioglu, A. Nikoozadeh, H.-S. Yoon, S. Vaithilingam, T. Carver and P. Khuri-Yakub, “Acoustic Lens For Capacitive Micromachined Ultrasonic Transducers”, *Journal of Micromechanics and Microengineering*, Vol. 24, p. 085007, 07 2014.

15. Snyder, A. W. and J. D. Love, *Optical Waveguide Theory*, Springer Science & Business Media, 2012.

16. Wang, Y.-Z., F.-M. Li, K. Kishimoto, Y.-S. Wang and W.-H. Huang, “Wave Band Gaps in Three-Dimensional Periodic Piezoelectric Structures”, *Mechanics Research Communications*, Vol. 36, pp. 461–468, 06 2009.

17. Jensen, J., “Phononic Band Gaps and Vibrations in One- and Two-Dimensional Mass–Spring Structures”, *Journal of Sound and Vibration*, Vol. 266, No. 5, pp. 1053–1078, 2003.

18. Kafesaki, M., M. M. Sigalas and E. N. Economou, “Elastic Wave Band Gaps in 3-D Periodic Polymer Matrix Composites”, *Solid State Communications*, Vol. 96, pp. 285–289, 1995.

19. Song, Y., L. Feng, J. Wen, D. Yu and X. Wen, “Analysis and Enhancement of Flexural Wave Stop Bands in 2D Periodic Plates”, *Physics Letters A*, Vol. 379, No. 22, pp. 1449–1456, 2015.

20. Rietman, E. and J. Glynn, “Band-gap engineering of phononic crystals: a computational survey of two-dimensional systems”, *arXiv preprint arXiv:0708.3669*, 2007.

21. Wen, J., G. Wang, D. Yu, H. Zhao, Y. Liu and X. Wen, “Study on the Vibration Band Gap and Vibration Attenuation Property of Phononic Crystals”, *Science in China Series E Technological Sciences*, Vol. 51, pp. 85–99, 04 2008.

22. Chang, L., “On The Limit of Spectral Gap Formation Via Bragg’s Reflection.”, *arXiv: Plasma Physics*, 2018.

23. Wu, Z., W. Liu, F. Li and C. Zhang, “Band-Gap Property of a Novel Elastic Metamaterial Beam With X-Shaped Local Resonators”, *Mechanical Systems and Signal Processing*, Vol. 134, p. 106357, 2019.

24. Bellido, J. C., A. Donoso and E. T. S. I. Industriales, “An Optimal Design Problem in Wave Propagation”, *Journal of Optimization Theory and Applications*, Vol. 134, pp. 339–352, 2007.

25. Goffaux, C., “Erratum: Two-Dimensional Phononic Crystals Studied Using a Variational Method: Application to Lattices of Locally Resonant Materials”, *Physical Review B*, Vol. 67, 04 2003.

26. Liu, Z., X. Zhang, Y. Mao, Y. Y. Zhu, Z. Yang, C. T. Chan and P. Sheng, “Locally Resonant Sonic Materials”, *Science*, Vol. 289, No. 5485, pp. 1734–1736, 2000.

27. Jensen, J., “Phononic Band Gaps and Vibrations in One- and Two-Dimensional Mass–Spring Structures”, *Journal of Sound and Vibration*, Vol. 266, pp. 1053–1078, 10 2003.

28. Assouar, B. and M. Oudich, “Enlargement of a Locally Resonant Sonic Band Gap by Using Double-Sides Stubbed Phononic Plates”, *Applied Physics Letters*, Vol. 100, 03 2012.

29. Sigalas, M. and E. Economou, “Band Structure of Elastic Waves in Two Dimensional Systems”, *Solid State Communications*, Vol. 86, No. 3, pp. 141–143, 1993.

30. Yilmaz, C. and G. Hulbert, “Theory of Phononic Gaps Induced by Inertial Amplification in Finite Structures”, *Physics Letters A*, Vol. 374, pp. 3576–3584, 07 2010.

31. Yilmaz, C., G. Hulbert and N. Kikuchi, “Phononic Band Gaps Induced by Inertial Amplification in Periodic Media”, *Physical Review B*, Vol. 76, pp. 54309–, 08 2007.

32. Higashino, M. and S. Okamoto, *Response Control and Seismic Isolation of Buildings (1st ed.)*, Routledge, 2006.

33. Zayas, V. A., S. S. Low and S. A. Mahin, “A Simple Pendulum Technique for Achieving Seismic Isolation”, *Earthquake Spectra*, Vol. 6, No. 2, pp. 317–333, 1990.

34. Naeim, F. and J. M. Kelly, *Design of Seismic Isolated Structures: From Theory to Practice (1. Edition)*, John Wiley Sons, 1999.

35. Sainidou, R., N. Stefanou and A. Modinos, “Formation of Absolute Frequency Gaps in Three-Dimensional Solid Phononic Crystals”, *Physical Review B*, Vol. 66, p. 212301, 12 2002.

36. Zhang, K., J. Luo, H. Fang and Z. Deng, “Seismic Metamaterials With Cross-Like and Square Steel Sections for Low-Frequency Wide Band Gaps”, *Engineering*

Structures, Vol. 232, p. 111870, 04 2021.

37. Muhammad and C. Lim, “Natural Seismic Metamaterials: The Role of Tree Branches in The Birth of Rayleigh Wave Bandgap for Ground Born Vibration Attenuation”, *Trees*, Vol. 35, 08 2021.

38. Zeng, Y., Y. Xu, K. Deng, Z. Zeng, H. Yang, M. Muhammad and Q. Du, “Low-Frequency Broadband Seismic Metamaterial Using I-Shaped Pillars in a Half-Space”, *Journal of Applied Physics*, Vol. 123, p. 214901, 06 2018.

39. Yan, Y., W. Witarto, S. Wang, Y. Mo, K. Chang, Y. Tang and M. Ruis, “Periodic material based seismic isolation for small modular reactors”, *Pressure Vessels and Piping Conference*, Vol. 57034, p. V008T08A041, American Society of Mechanical Engineers, 2015.

40. Jia, G. and Z. Shi, “A New Seismic Isolation System and Its Feasibility Study”, *Earthquake Engineering and Engineering Vibration*, Vol. 9, pp. 75–82, 03 2010.

41. Yan, Y., A. Laskar, Z. Cheng, F. Menq, Y. Tang, Y. Mo and Z. Shi, “Seismic Isolation of Two Dimensional Periodic Foundations”, *Journal of Applied Physics*, Vol. 116, p. 044908, 07 2014.

42. Yan, Y., A. Laskar, Z. Cheng, F. Menq, Y. Tang, Y. Mo and Z. Shi, “Periodic Materials-Based 3D Seismic Base Isolators for Nuclear Power Plants”, *Pressure Vessels and Piping Conference*, Vol. 46070, p. V008T08A008, American Society of Mechanical Engineers, 2014.

43. Witarto, W., S. Wang, C. Yang, X. Nie, Y. Mo, K.-C. Chang, Y. Tang and R. Kassawara, “Seismic Isolation of Small Modular Reactors Using Metamaterials”, *AIP Advances*, Vol. 8, p. 045307, 04 2018.

44. Yan, Y., Z. Cheng, F. M. Menq, Y. L. Mo, Y. Tang and Z. fei Shi, “Three dimensional periodic foundations for base seismic isolation”, *Smart Materials and*

Structures, Vol. 24, p. 075006, 2015.

45. Shi, Z., Z. Cheng and H. Xiang, “Seismic Isolation Foundations With Effective Attenuation Zones”, *Soil Dynamics and Earthquake Engineering*, Vol. 57, p. 143–151, 02 2014.

46. Miniaci, M., K. Nesrine, C. Cröenne, M. Mazzotti, M. Morvaridi, A. Gliozzi, M. Onorato, F. Bosia and N. Pugno, “Hierarchical Large-Scale Elastic Metamaterials for Passive Seismic Wave Mitigation”, *EPJ Applied Metamaterials*, Vol. 8, p. 14, 01 2021.

47. Bursi, O. S., F. Basone and M. Wenzel, “Stochastic Analysis of Locally Resonant Linear and Hysteretic Metamaterials for Seismic Isolation of Process Equipment”, *Journal of Sound and Vibration*, Vol. 510, p. 116263, 2021.

48. Muhammad and C. Lim, *Design and Manufacturing of Monolithic Mechanical Metastructure with Ultrawide Bandgap for Low Frequency Vibration and Noise Control*, META 2021, the 11th International Conference on Metamaterials, Photonic Crystals and Plasmonics Conference, Warsaw, Poland, City University of Hong Kong, Hong Kong, 2021.

49. Lucklum, F. and M. Vellekoop, “Bandgap Engineering of Three-Dimensional Phononic Crystals in a Simple Cubic Lattice”, *Applied Physics Letters*, Vol. 113, p. 201902, 11 2018.

50. Muhammad and C. Lim, “Ultrawide Bandgap by 3D Monolithic Mechanical Metastructure for Vibration and Noise Control”, *Archives of Civil and Mechanical Engineering*, Vol. 21, p. 52, 05 2021.

51. D’Alessandro, L., R. Ardito, F. Braghin and A. Corigliano, “Low Frequency 3D Ultra-Wide Vibration Attenuation via Elastic Metamaterial”, *Scientific Reports*, Vol. 9, 05 2019.

52. Taniker, S. and C. Yilmaz, “Generating Ultra Wide Vibration Stop Bands by a Novel Inertial Amplification Mechanism Topology With Flexure Hinges”, *International Journal of Solids and Structures*, Vol. 106-107, pp. 129–138, 2017.

APPENDIX A: ELSEVIER LICENSE NUMBER 5370721129532

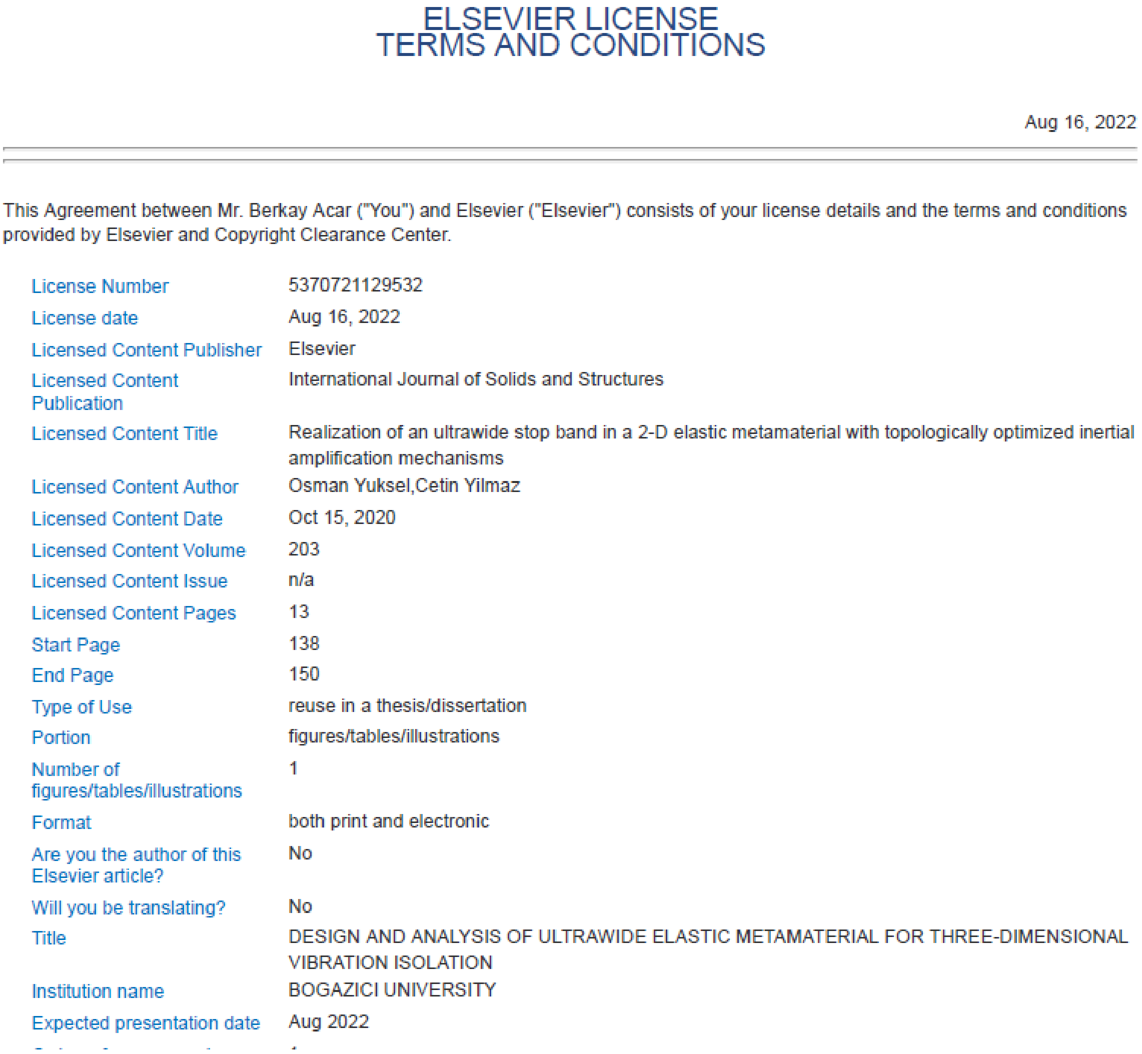

ELSEVIER LICENSE
TERMS AND CONDITIONS

Aug 16, 2022

This Agreement between Mr. Berkay Acar ("You") and Elsevier ("Elsevier") consists of your license details and the terms and conditions provided by Elsevier and Copyright Clearance Center.

License Number	5370721129532
License date	Aug 16, 2022
Licensed Content Publisher	Elsevier
Licensed Content Publication	International Journal of Solids and Structures
Licensed Content Title	Realization of an ultrawide stop band in a 2-D elastic metamaterial with topologically optimized inertial amplification mechanisms
Licensed Content Author	Osman Yuksel,Cetin Yilmaz
Licensed Content Date	Oct 15, 2020
Licensed Content Volume	203
Licensed Content Issue	n/a
Licensed Content Pages	13
Start Page	138
End Page	150
Type of Use	reuse in a thesis/dissertation
Portion	figures/tables/illustrations
Number of figures/tables/illustrations	1
Format	both print and electronic
Are you the author of this Elsevier article?	No
Will you be translating?	No
Title	DESIGN AND ANALYSIS OF ULTRAWIDE ELASTIC METAMATERIAL FOR THREE-DIMENSIONAL VIBRATION ISOLATION
Institution name	BOGAZICI UNIVERSITY
Expected presentation date	Aug 2022

Figure A.1. Elsevier license of [1] for Figure 1.2.

APPENDIX B: ELSEVIER LICENSE NUMBER 5370721085469

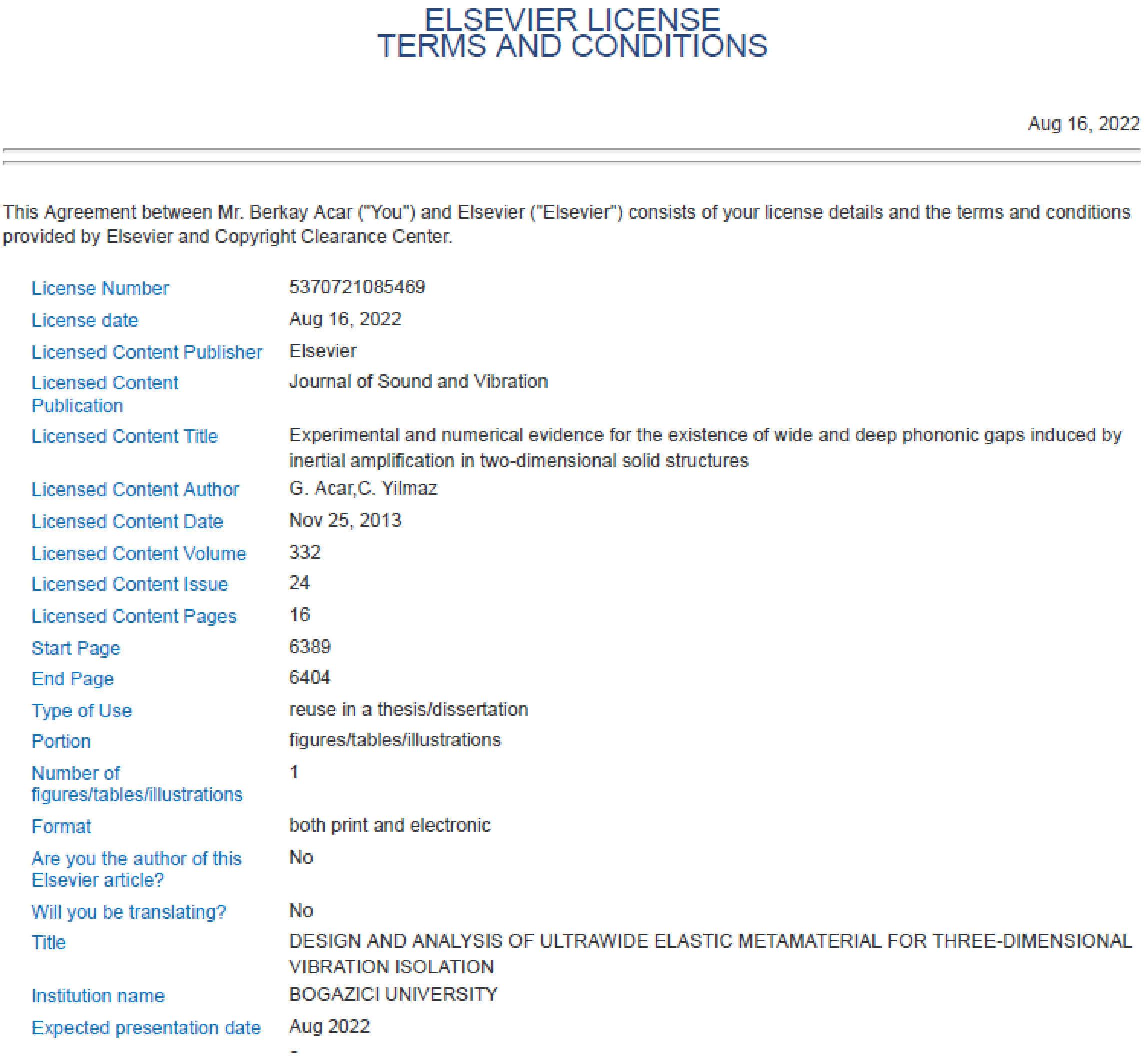

ELSEVIER LICENSE
TERMS AND CONDITIONS

Aug 16, 2022

This Agreement between Mr. Berkay Acar ("You") and Elsevier ("Elsevier") consists of your license details and the terms and conditions provided by Elsevier and Copyright Clearance Center.

License Number	5370721085469
License date	Aug 16, 2022
Licensed Content Publisher	Elsevier
Licensed Content Publication	Journal of Sound and Vibration
Licensed Content Title	Experimental and numerical evidence for the existence of wide and deep phononic gaps induced by inertial amplification in two-dimensional solid structures
Licensed Content Author	G. Acar,C. Yilmaz
Licensed Content Date	Nov 25, 2013
Licensed Content Volume	332
Licensed Content Issue	24
Licensed Content Pages	16
Start Page	6389
End Page	6404
Type of Use	reuse in a thesis/dissertation
Portion	figures/tables/illustrations
Number of figures/tables/illustrations	1
Format	both print and electronic
Are you the author of this Elsevier article?	No
Will you be translating?	No
Title	DESIGN AND ANALYSIS OF ULTRAWIDE ELASTIC METAMATERIAL FOR THREE-DIMENSIONAL VIBRATION ISOLATION
Institution name	BOGAZICI UNIVERSITY
Expected presentation date	Aug 2022

Figure B.1. Elsevier license of [2] for Figure 1.3.

APPENDIX C: ELSEVIER LICENSE NUMBER 5370721053578

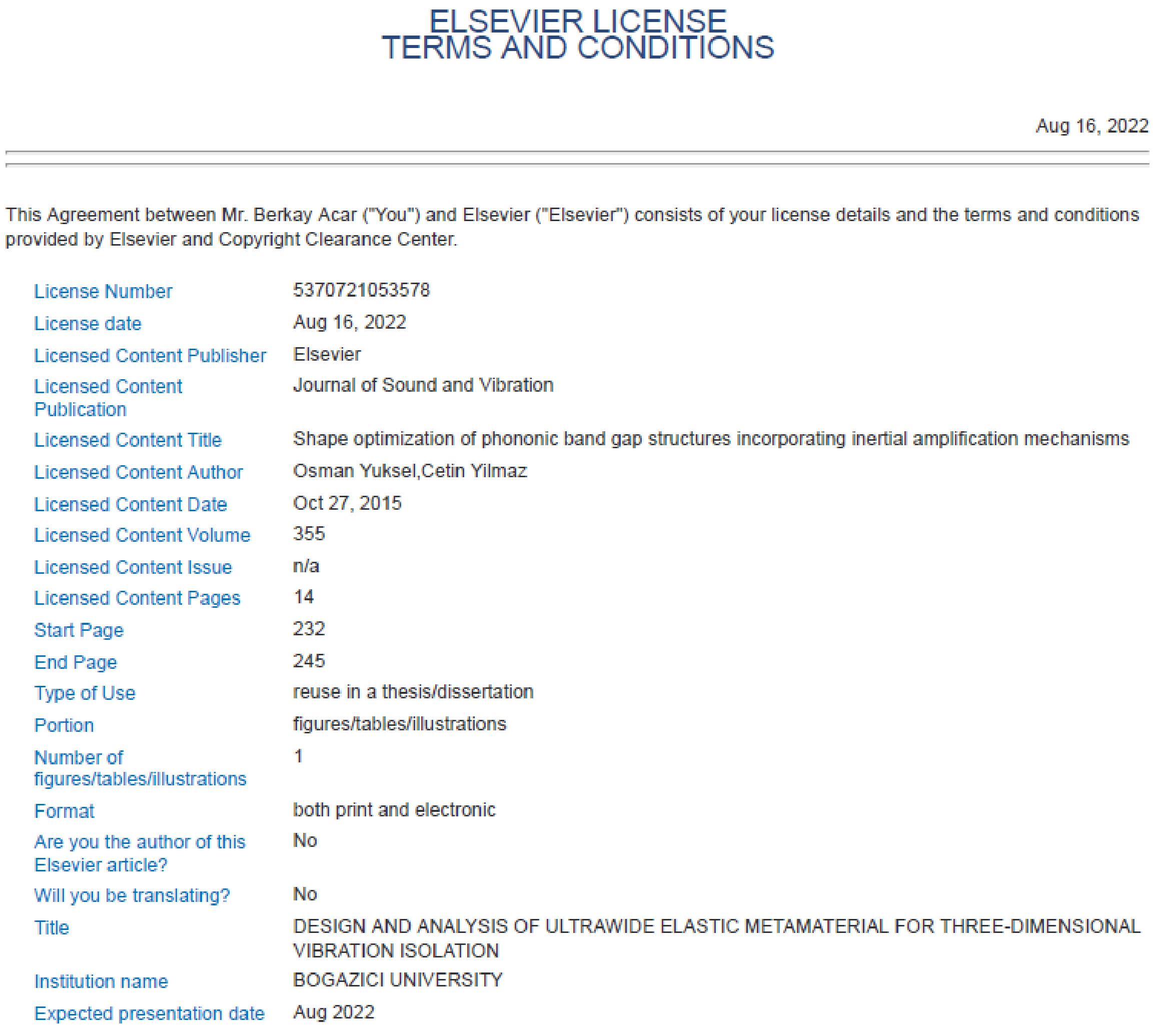

ELSEVIER LICENSE
TERMS AND CONDITIONS

Aug 16, 2022

This Agreement between Mr. Berkay Acar ("You") and Elsevier ("Elsevier") consists of your license details and the terms and conditions provided by Elsevier and Copyright Clearance Center.

License Number	5370721053578
License date	Aug 16, 2022
Licensed Content Publisher	Elsevier
Licensed Content Publication	Journal of Sound and Vibration
Licensed Content Title	Shape optimization of phononic band gap structures incorporating inertial amplification mechanisms
Licensed Content Author	Osman Yuksel,Cetin Yilmaz
Licensed Content Date	Oct 27, 2015
Licensed Content Volume	355
Licensed Content Issue	n/a
Licensed Content Pages	14
Start Page	232
End Page	245
Type of Use	reuse in a thesis/dissertation
Portion	figures/tables/illustrations
Number of figures/tables/illustrations	1
Format	both print and electronic
Are you the author of this Elsevier article?	No
Will you be translating?	No
Title	DESIGN AND ANALYSIS OF ULTRAWIDE ELASTIC METAMATERIAL FOR THREE-DIMENSIONAL VIBRATION ISOLATION
Institution name	BOGAZICI UNIVERSITY
Expected presentation date	Aug 2022

Figure C.1. Elsevier license of [3] for Figure 1.4.